
**TRIBHUVAN UNIVERSITY**

**INSTITUTE OF ENGINEERING**

**PULCHOWK CAMPUS**

**THESIS NO: M-90-MSMDE-2023-2025**

# Numerical and Experimental Analysis of the Fluidic Thrust Vectoring by Shock Vector Control in a Two Dimensional Convergent - Divergent Nozzle

by

Keshav Kumar Acharya (079MSMDE011)

A THESIS

SUBMITTED TO THE DEPARTMENT OF MECHANICAL AND AEROSPACE ENGINEERING IN PARTIAL FULFILLMENT OF THE REQUIREMENTS FOR THE DEGREE OF MASTER OF SCIENCE IN MECHANICAL SYSTEM DESIGN ENGINEERING

DEPARTMENT OF MECHANICAL AND AEROSPACE ENGINEERING,
LALITPUR, NEPAL

April, 2025

## COPYRIGHT

**TRIBHUVAN UNIVERSITY**

**INSTITUTE OF ENGINEERING**

**PULCHOWK CAMPUS**

**DEPARTMENT OF MECHANICAL AND AEROSPACE ENGINEERING**

The undersigned certify that they have read, and recommended to the Institute of Engineering for acceptance, a thesis entitled **"Numerical and Experimental Analysis of the Fluidic Thrust Vectoring by Shock Vector Control in a Two Dimensional Convergent - Divergent Nozzle"** submitted by **Keshav Kumar Acharya (079MSMDE011)** in partial fulfillment of the requirement for the degree of Master of Science in Mechanical Systems Design and Engineering.

Asst. Prof. Kamal Darlami
Supervisor,
Department of Mechanical and Aersospace Engineering

Er. Salim Maharjan
External Examiner,
Visiting Faculty,
Himalaya College of Engineering, Lalitpur

Tribhuvan University
Institute of Engineering
Department of Mechanical and Aerospace Engineering
Pulchowk Campus

Committee Chairperson,
Asst. Prof. Dr. Sudip Bhattarai,
Head of Department,
Department of Mechanical and Aersospace Engineering

Date : April 7, 2025

## ABSTRACT

This study presents a comprehensive numerical and experimental analysis of fluidic thrust vectoring using shock vector control (SVC) in a two-dimensional convergent-divergent (CD) nozzle. The research integrates computational fluid dynamics (CFD) simulations and Schlieren imaging experiments to evaluate the effects of secondary flow injection on thrust vectoring.

The study begins with the development and testing of a single-mirror Schlieren imaging setup, which is utilized to visualize thermal plumes from candle and hand and later to visualize supersonic flow structures inside and at the exit of the nozzle. The CD nozzle is designed using the Method of Characteristics (MOC) and simulated in ANSYS Fluent to investigate the effect of nozzle pressure ratio (NPR), secondary pressure ratio (SPR), and secondary injection location on jet deflection. Experimental validation is conducted using a 3D-printed nozzle tested in the test rig constructed locally.

The results indicate that increasing NPR reduces jet deflection, while an optimal SPR exists for maximizing thrust vectoring before performance degradation occurs. Furthermore, secondary injection location significantly influences jet behavior, with downstream placements yielding greater deflection angles. The comparison of experimental Schlieren images with CFD results demonstrates strong agreement, validating the numerical models.

This research confirms that shock vector control is a viable and effective fluidic thrust vectoring technique, offering potential advantages for aerospace propulsion applications. Future studies are recommended to refine experimental setups, investigate on the effect of other parameters on thrust vectoring, using other turbulence models, and investigate three-dimensional flow behaviors for enhanced system performance.



Keywords: Fluidic Thrust Vectoring, Shock Vector Control, Convergent-Divergent Nozzle, Schlieren Imaging, Computational Fluid Dynamics

## ACKNOWLEDGEMENT

I would like to express my deepest gratitude to my supervisor Asst. Prof. Kamal Darlami for his unwavering guidance, support and inspiration through out this project. I would also like to express my sincere thanks to the Department of Mechanical and Aerospace Engineering, Institute of Engineering for providing the opportunity to carry out the thesis work as partial fulfillment of the Masters of Science in Mechanical Systems Design and Engineering. I am also thankful towards Asst. Prof. Dr. Sudip Bhattrai, Head of Department, Department of Mechanical and Aerospace Engineering for his constant encouragement and words of wisdom.

I am very grateful to the Department of Mechanical Engineering, Purwanchal Campus, Dharan for providing working space for schlieren imaging setup. I would also like to express my sincere thanks to Asst. Prof. Kaji Ram Karki, campus chief, Purwanchal Campus for providing all the assistance in setting up the experimental setup. I would also like to acknowledge Asst. Prof. Yam Kumar Rai, Head of Agriculture Engineering Department for providing much needed two stage compressor for setting up experimental test rig. I am also very thankful to the staffs from carpentary department in assisting with the fabrication of different components.

Special thanks goes to Salim Maharjan, Abhishek Bhandari, Rajan Jung Basnet, and Sujan Dahal for their guidance and assistance during the project. Similarly, special thanks also goes to Bharat Shah and Dipesh Chaudhary for assisting in carrying out experimental studies. I would like to express my sincere appreciation to all my dear friends and family for their constant support and care amid which this thesis work is brought into fruition.

## TABLE OF CONTENTS

## LIST OF FIGURES

## LIST OF TABLES

## LIST OF SYMBOLS

| | | |
|---|---|---|
| A | : | Cross - sectional area |
| a | : | Velocity of sound |
| $A^*$ | : | Throat cross sectional area |
| $a_e$ | : | Sonic velocity at exit of nozzle |
| c | : | Speed of light in the medium (m/s) |
| $c_0$ | : | Speed of light in vacuum = $3 \times 10^8$ |
| f | : | Focal length of the mirror |
| h | : | Enthalpy |
| k | : | Gladstone – Dale constant ($m^3/kg$) |
| M | : | Mach number |
| n | : | Refractive index of a medium |
| p | : | Pressure |
| $P^*$ | : | Pressure at sonic condition |
| $P_0$ | : | Stagnation pressure |
| $P_a$ | : | Atmospheric pressure (101325 Pa) |
| R | : | Gas constant |
| T | : | Temperature |
| t | : | Time |
| $T^*$ | : | Temperature at sonic condition |
| $T_0$ | : | Stagnation temperature |
| $T_e$ | : | Temperature at exit nozzle |
| u | : | Velocity component in x - direction |
| $u_e$ | : | Velocity at exit of nozzle |
| $\gamma$ | : | Specific heat ratio |
| $\varepsilon$ | : | Deflection angle of light ray (radian) |
| $\rho$ | : | Density of a medium ($kg/m^3$) |
| $\rho^*$ | : | Density at sonic condition |
| $\rho_0$ | : | Stagnation density |
| $\rho_e$ | : | Density at exit of nozzle |

## LIST OF ABBREVIATIONS

| | | |
|---|---|---|
| 2 - D | = | Two Dimensional |
| 3 - D | = | Three Dimensional |
| AC | = | Alternating Current |
| BDTN | = | Bypass Dual Throat Nozzle |
| BOS | = | Background - Oriented Schlieren |
| CD Nozzle | = | Converging – Diverging Nozzle |
| CDC | = | Convergent - Divergent - Convergent |
| CFD | = | Computational Fluid Dynamics |
| DC | = | Direct Current |
| DSLR | = | Digital Single - Lens Reflex |
| DTN | = | Dual Throat Nozzle |
| FC – nozzle | = | Fluidic Coanda nozzle |
| FDM | = | Fused Deposition Modeling |
| FTV | = | Fluidic Thrust Vectoring |
| IF | = | Forward current |
| IOE | = | Institute of Engineering |
| LED | = | Light Emitting Diode |
| MOC | = | Method of Characteristics |
| MTV | = | Mechanical Thrust Vectoring |
| NASA | = | National Aeronautics and Space Administration |
| NPR | = | Nozzle Pressure Ratio |
| PLA | = | Polylactic Acid |
| SPR | = | Secondary Pressure Ratio |
| SVC | = | Shock Vector Control |
| TSC | = | Throat Skewing Control |
| TV | = | Thrust Vectoring |
| VF | = | Forward voltage |

# CHAPTER ONE : INTRODUCTION

## 1.1 Background

The fluid flows are governed by complex partial differential equations, the closed form analytical solutions of which are not derivable except for very simple flows. If the closed form analytical solution existed, flow patterns could be plotted or visualized easily. Furthermore, due to the transparent nature of large number of fluids, it's difficult to predict the features of the flow along with the hidden pattern underneath the flow. Due to these difficulties, it becomes necessary to carry out flow visualization in order to visualize and understand the nature of fluid flow along with the intricacies underlying the fluid flows. Light scattering from tracer particles, optical techniques based on fluid's changes in refractive index, and fluid flow interaction processes with a solid surface are the three main ways to visualize flow (Merzkirch, 2011). Among these techniques, the optical approaches are the most appropriate for studying the intricacies of the flow field since they are non – intrusive in nature.

Optical flow visualization techniques use light and the changes it undergoes while passing through the flow- region of interest to provide information about the fluid-flow behavior and inherent patterns as shown in the Figure 1.1. According to (Settles, 2001), there exists a simple relationship between the refractive index and density for air and other gases and is given by Equation 1.1.

$$n - 1 = k\rho \qquad \text{Equation 1.1}$$

where, $k$ is called the Gladstone – Dale constant which has units of $1/\rho$. Its value depends on the type of gas and the wavelength of the light.

Fermat's principle dictates the path a light wave or light ray follows as it moves through an inhomogeneous flow-field, like the area of mixed fluid density shown in Figure 1.1. The light beam is bent from its original straight-line path because of the changes in density and, hence, the refractive index. Undergoing displacement in two primary directions, $\Delta x$ and $\Delta y$, the deflected light finally reaches the recording plane. For given z, the direction in which the incident light beam travels, the deflection angles would be $\varepsilon_x$ and $\varepsilon_y$ in x and y – directions respectively. Light would be deflected along with an optical

phase shift. A visual signal is then created in the recording plane which could be a background with white color or an electronic camera due to changes in optical path and phase as discussed earlier. This study would allow one to establish a correlation between changes in the flow under investigation's density/refractive index and the ensuing fluctuations in the signal seen in the recording plane.

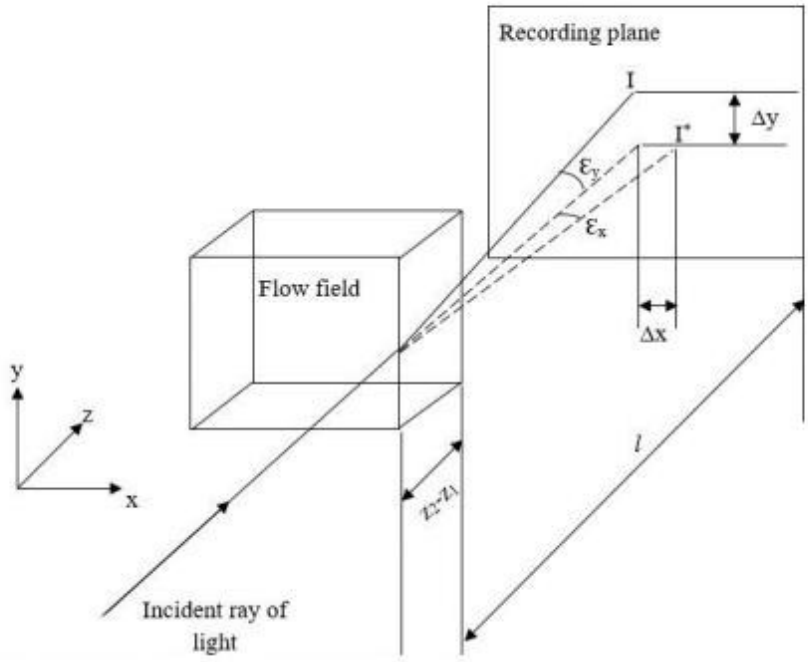


Figure 1.1: A light beam deflecting as it passes through a flow field of different densities

Schlieren photography, Shadowgraphy, Moiré Deflectometry, Speckle Photography, Interferometry, etc are some of the examples of optical flow visualization methods (Maharjan, 2023). Among these techniques, this research work mainly focuses on Schlieren imaging. This research focuses on setting up a Schlieren system and to use this system to visualize the flow from the CD – nozzle with fluidic thrust vectoring incorporated into it.

**1.2 Statement of Problem**

Schlieren imaging finds most of its uses in the fields of engineering, high-speed phenomenon, and aerospace, with applications pertaining to the flow of transparent fluids

and air receiving special attention. This study intends to construct and configure a Schlieren imaging system for the purpose of visualizing various density gradient-related fluid-flow events. The main focus is the study of fluidic thrust vectoring using shock vector control in a two–dimensional CD nozzle using computational analysis and experimental analysis using a Schlieren imaging setup.

## 1.3 Objectives

### 1.3.1 Main Objective

The primary objective of this study is as follows:

- To carry out numerical simulations and experimental analysis of the fluidic thrust vectoring using shock vector control in a two – dimensional convergent-divergent nozzle.

### 1.3.2 Specific Objectives

The following are the secondary objectives of this work:

- To fabricate a single mirror Schlieren imaging system for flow visualization with wide test section.
- To carry out computational analysis of thrust vectoring using shock vector control method in converging diverging nozzle using ANSYS fluent
- To carry out experimentation in the 3 – D printed nozzle and to validate the results obtained in computation through Schlieren imaging system.

## 1.4 Research Question

This research work attempts to answer following research questions:

- Does the fabricated Schlieren imaging system has enough sensitivity to record complex density-gradient features of thermal plumes and supersonic fluid-flow phenomenon?
- Does the computational fluid flow analysis carried out in the designed CD – nozzle correctly predict the actual flow pattern?

## 1.5 Limitations

The limitations of this work can be summarized as follows:

- Among various type of fluidic thrust vectoring only shock vector control is considered for this work
- Only a small scale working model of CD – nozzle will be manufactured using 3 – D printing technology. So, the material will be the one used in 3 – D printing instead of being one used for actually fabricating the CD – nozzle.
- The pressure in the inlet side of the nozzle may not be too high due to the constraint in air compressor available.

# CHAPTER TWO : LITERATURE REVIEW

## 2.1 Schlieren

Schlieren imaging is a non – intrusive optical technique that shows changes in transparent media's refractive index. When analyzing optical phenomena, heat transfer, and fluid fluxes which are otherwise undetectable to the human eyes, this method works especially well. The basis of the Schlieren technique is the idea that changes in a transparent medium's density, such as water or air, will result in changes to that medium's refractive index. These changes result in the light beams bending or diverging from their original pathways as they travel through such material. Schlieren imaging shows the changes in refractive index by identifying these discrepancies.

### 2.1.1 History and Development of Schlieren Imaging

Schlieren imaging's beginnings date back to the seventeenth century, a time when prominent scientists like Isaac Newton and Robert Hooke studied the behavior of light. Hooke explained how changes in air density could impact light refraction in his groundbreaking work *Micrographia* (1665). These initial findings established the foundation for comprehending how variations in refractive index might be represented through light visualization.

German physicist August Toepler made the first workable Schlieren apparatus in 1864, which is credited with the invention of the modern Schlieren technique. With Toepler's method, variations in the refractive index, which resulted in deviations in light path were detected using a knife-edge technique. This breakthrough made phenomena like shock waves and supersonic velocity in gases that would otherwise be invisible observable. With Toepler's work, Schlieren imaging became a scientific instrument and opened up new avenues for the study of optical fluctuations and fluid dynamics.

Schlieren imaging made great strides in the early 20th century, thanks in large part to the efforts of Ludwig Prandtl and others at the University of Göttingen. A pioneer in the field of aerodynamics, Prandtl examined flow processes surrounding objects and boundary layers using Schlieren techniques. His work influenced the advancement of contemporary aerodynamic theory and application. Schlieren imaging became well - known in military studies during World War II, helping to understand explosions and high-speed

aerodynamics. The method was essential for comprehending how shock waves and supersonic flows behaved, which was necessary for creating quicker and more effective aircraft. The post-war improvements in light sources, optical elements, and recording apparatus considerably augmented the Schlieren imaging's capabilities.

Schlieren image technology underwent a digital revolution in the late 20th and early 21st centuries. The method was revolutionized by the advent of digital cameras and image processing software, which made quantitative analysis and real-time visualization possible. With the remarkable sensitivity and flexibility offered by modern digital Schlieren equipment, researchers may precisely record and analyze complex fluid movements. Schlieren imaging has evolved into a number of variations each suited to a particular use case. For example, Color Schlieren adds color information to flow structures to improve their visibility. The technique's application has been further increased by background-oriented Schlieren (BOS) and synthetic Schlieren, which provide additional avenues for investigating a variety of phenomena.

Schlieren imaging is a vital technique in many industrial and scientific fields these days. It is often used in wind tunnels in aerodynamics and aerospace engineering to see shock waves, boundary layers, and other flow phenomena surrounding aircraft and spacecraft models. This skill is essential for performance improvement and design optimization. Moreover, Schlieren imaging aids in the understanding of flame behavior, combustion processes, and explosions in combustion research. Gaining this understanding is essential to improving the safety and efficiency of reactors and engines. Additionally, the method finds usage in biological and medical research, where it is applied to investigate biological fluid behavior, heat transfer in tissues, and respiratory fluxes. Additionally, Schlieren imaging has gained popularity as a teaching tool because it presents basic concepts in fluid dynamics and optics in an interesting and eye-catching way. Its capacity to reveal the invisible keeps motivating both scholars and pupils.

The development of Schlieren imaging is a monument to human creativity and the unwavering quest for comprehension of difficult phenomena. Schlieren imaging has developed into a potent and adaptable method, starting with Hooke and Newton's initial discoveries and continuing with Toepler's groundbreaking research and contemporary

digital systems. Its broad applications highlight its continuing significance and relevance, offering priceless insights into the behavior of transparent media and intricate fluid movements. Schlieren imaging will surely continue to be at the forefront of scientific innovation and discovery as long as technology persists in its advancement.

### 2.1.2 Mathematical Foundation of Schlieren Imaging

Schlieren imaging's physical foundation comes from Snell's Law, which states that the speed of light slows down when interacting with matter. In a homogeneous medium, light moves consistently and at a constant speed. Schliere is the result of light beams refracting and deflecting from their continuous path when they come into contact with inhomogeneous material, such as fluids on motion. Outlining the laws governing Schlieren pictures is important in order to use suitable quantitative analysis to Schlieren optics systems.

The simplest Schlieren system visualizes schliere by using a straight-line lens configuration, as shown in Figure 2.1. A beam of light originating from light source B and passing through slit O is rendered parallel by first lens $L_1$. The parallel beam of light then passes through the test subject E where it gets deflected and then onto the second lens $L_2$. The second lens $L_2$ focuses the light on to the knife – edge cut – off K. Finally the Schlieren image is projected onto the screen or photographic sensor, H with the help of projection lens $L_3$ (Mazumdar, 2013).

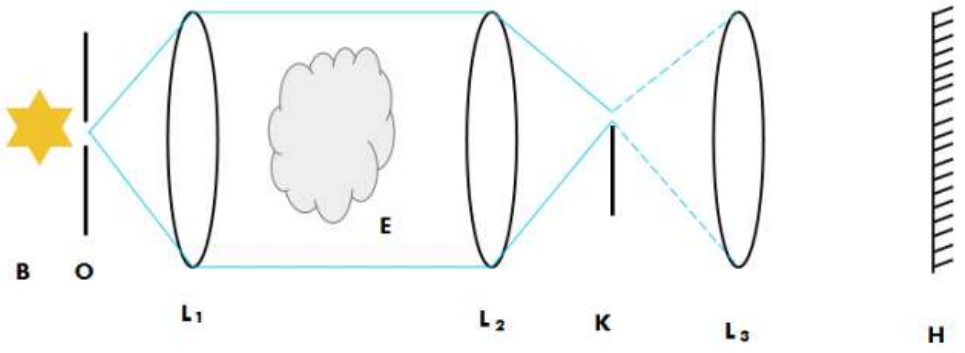


Figure 2.1: Schematic diagram of lens-based schlieren optics system (Mazumdar, 2013)

Fermat's principle—which states that "light travels between two points along the path that requires the least amount of time, as compared to other nearby paths"—forms the mathematical foundation of Schlieren imaging. Fermat's principle readily simplifies to Snell's law, also known as the law of refraction, when one considers a light beam traveling through a Schlieren object, or an area of density/refractive index differences. The light beam becomes bent as it interacts with the area of varied density. This change is indicated by refractive index ($n$) and given by the equation

$$n = \frac{c_0}{c} \qquad \text{Equation 2.1}$$

Where,

c = speed of light while travelling in the medium

$c_0$ = speed of light while travelling in the vacuum ($3 \times 10^8$ m/s)

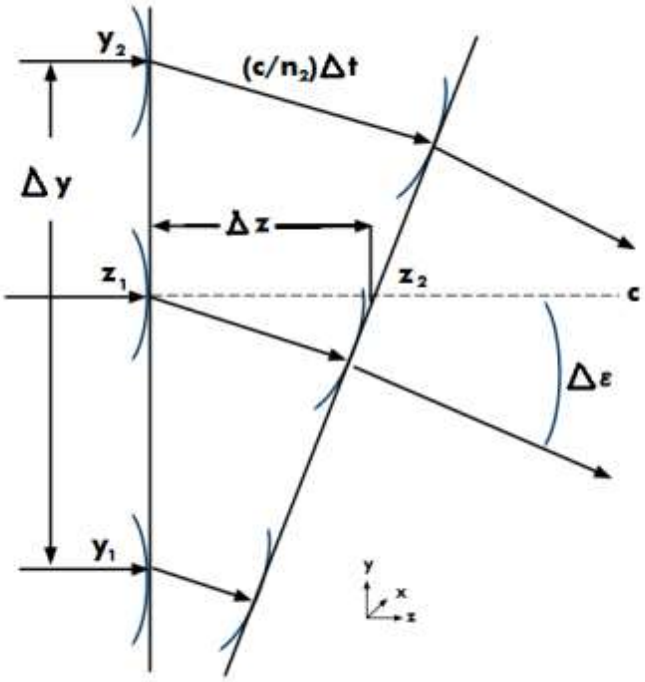


Figure 2.2: Diagram of light-ray deflection by a refractive-index gradient dn/dy *(Mazumdar, 2013)*

In order to demonstrate how the Schlieren light refraction occurs, let's consider that the refractive index has negative gradient in y direction i.e. $\partial n/\partial y < 0$, and no gradient in other 2 principle directions (i.e. x and z – directions). Once a vertical planar light wave passes through a Schlieren object, it is displaced from its initial vertical position. Let's assume that the light wave travels a differential distance $\Delta z$ in differential time $\Delta t$ being refracted through a differential angle of $\Delta\varepsilon$ as shown in the Figure 2.2. From the Figure 2.2, it can be written as:

$$\Delta\varepsilon = \frac{\frac{c}{n_2} - \frac{c}{n_1}}{\Delta y}\,\Delta t \qquad \text{Equation 2.2}$$

When the above expression is combined with an expression for differential time given by $\Delta t = \Delta z \frac{n}{c}$, and terms simplified, the above equation becomes:

$$\Delta\varepsilon = \frac{n}{n_1 n_2}\,\frac{(n_1 - n_2)}{\Delta y}\Delta z \qquad \text{Equation 2.3}$$

This equation can be further simplified by letting all finite differences approach zero and simplifying $\frac{n}{n_1 n_2}$ to $\frac{1}{n}$ to obtain:

$$\frac{d\varepsilon}{dz} = \frac{1}{n}\frac{dn}{dy} \qquad \text{Equation 2.4}$$

On using small angle approximation to postulate $= \frac{dy}{dz}$ , the above equation can be re - written as:

$$\frac{\partial^2 y}{\partial z^2} = \frac{1}{n}\frac{\partial n}{\partial y} \qquad \text{Equation 2.5}$$

The relation between refracted ray curvature and refractive – index gradient is established by Equation 2.5. The angular ray deflection's components in x – and y – directions can be obtained by integrating the above equation once. Following expressions are obtained:

$$\varepsilon_x = \frac{1}{n}\int \frac{\partial n}{\partial x}\partial z \qquad \text{Equation 2.6}$$

$$\varepsilon_y = \frac{1}{n}\int \frac{\partial n}{\partial y}\partial z \qquad \text{Equation 2.7}$$

### 2.1.3 Single Mirror Schlieren Imaging Setup

A single mirror Schlieren imaging setup consists of four elements; single concave mirror, a point light source, a sharp knife – edge and a digital camera arranged in an arrangement as depicted by Figure 2.3.

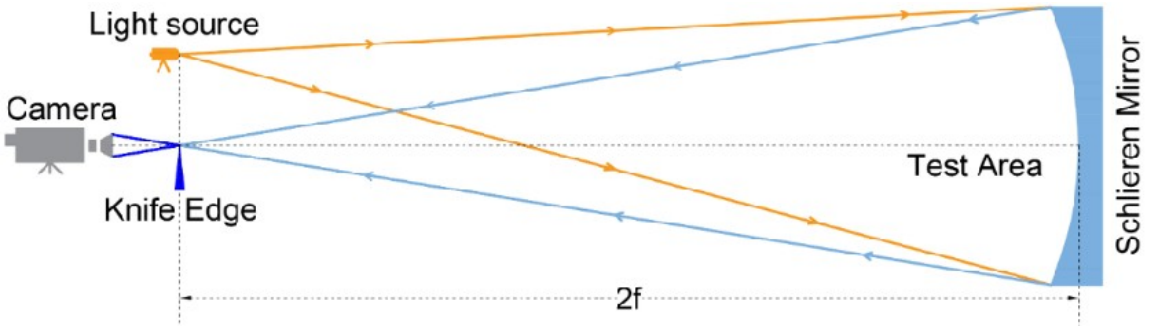


Figure 2.3: Schematic diagram of a single mirror schlieren imaging setup *(Gena & Voelker, 2018)*

In this setup, a point light source is placed at a length equal to the radius of curvature (R = 2f) from the mirror. The light emitted from the point source fills the mirror and returns converging into a single point at the distance equal to 2f from the mirror. In doing so the light traversed the test section twice. A knife edge is placed at the same point, where the light converges into a single point, to partially block some of the light returning from the mirror. A camera placed behind the knife edge captures the Schlieren image.

### 2.1.4 Z – Type Two Mirror Schlieren System

This system consists of two telescopic parabolic mirrors, a point light source, a knife edge and a camera. The layout of the setup is shown in the Figure 2.4. The point light source is placed at a distance f away from the first mirror tilted at a small angle from the optical centerline. The diverging light emitted by the light source is collimated by the first mirror to produce parallel rays of light in the test area. The parallel rays of light after falling upon the second mirror are focused onto the knife edge, which blocks a portion of the incoming light. The light then finally falls upon the camera. The parallel light beam experiences a schliere as it travels across the test section because of the different indices

of refraction, which bend it. By creating a range of light shades, either monochromatic or colored, this effect makes it possible to see how a fluid's density changes. The two mirrors are tilted by the same angle but in opposite direction and are placed at about 2f distance, where f is the focal length of the mirrors.

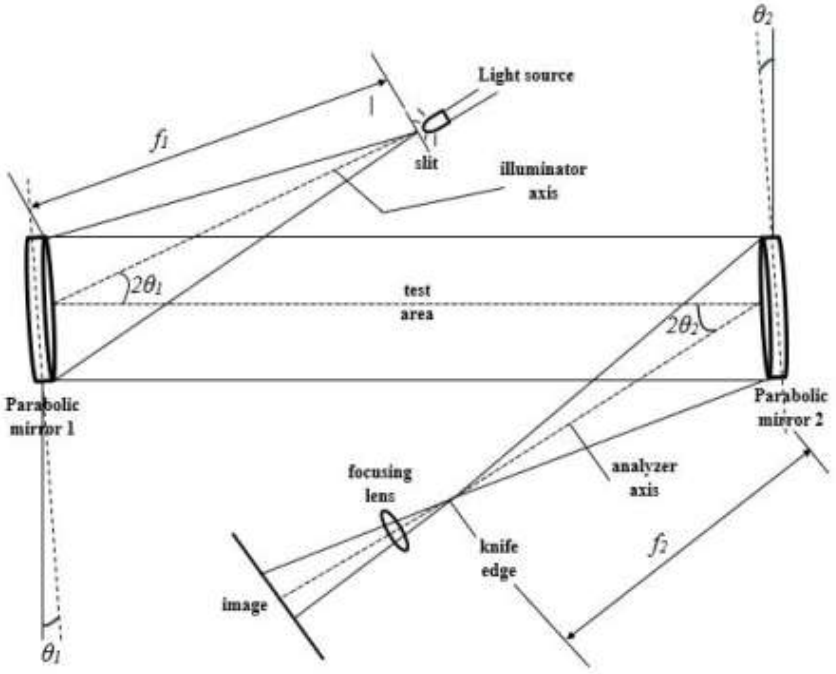


Figure 2.4: Schematic diagram of z - type schlieren imaging setup *(Maharjan, 2023)*

## 2.2 De – Laval Nozzle

De Laval nozzle uses change in the area of the flow region to accelerate the flow from subsonic speed to supersonic speed. There are three regions in the nozzle; convergent section, throat, and divergent section. In the convergent section, the flow cross sectional area reduces, becomes least at the throat and increases in the divergent section. When properly configured, a flow through a de Laval will start off as subsonic, change to sonic at the throat, and continue to be supersonic as it passes through the outlet. The flow itself is driven by a pressure gradient along the nozzle (Robinson, 2016).

### 2.2.1 Quasi – One – Dimensional Flow

One – dimensional flows are strictly constant – area flow but in case of the Convergent – Divergent (CD) nozzle, the cross - sectional area varies in the direction of flow. In case of

CD nozzle, the restriction is relaxed and the streamtube area A is allowed to change with distance *x* but at the same time, all the flow properties are assumed to be uniform at any given cross section of the flow. Thus, the properties are the functions of *x* only (and time *t* in case of unsteady flow). This kind of flow, where all the flow properties along with cross section area are the functions of *x* only, are called quasi – one – dimensional flow.

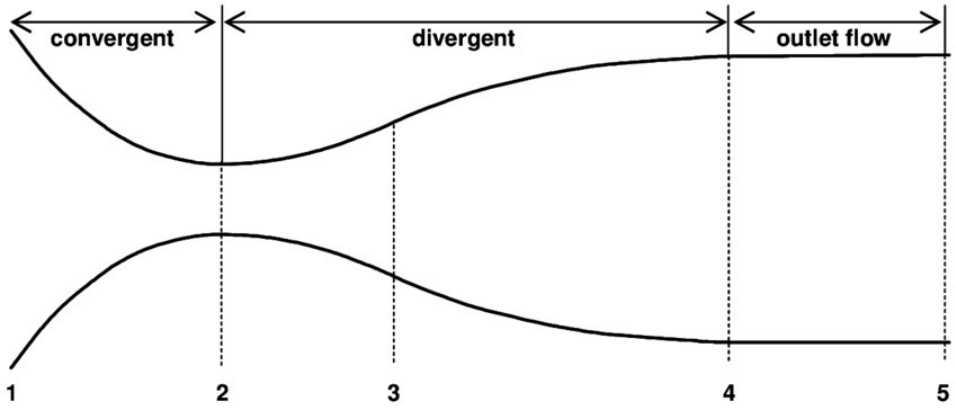


Figure 2.5: Convergent - divergent nozzle

### 2.2.2 Governing Equations

Algebraic relations for steady quasi – one – dimensional flow through nozzle can be derived by using the integral form of the conservation equation to a variable – area control volume as shown in Figure 2.6.

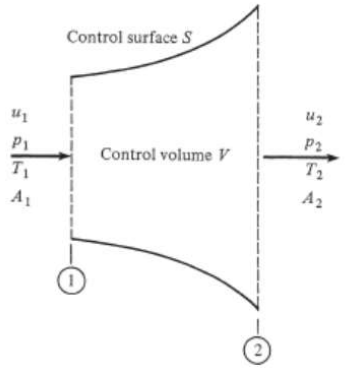


Figure 2.6 : Finite control volume for quasi - one - dimensional flow *(Anderson, 2021)*

Following algebraic equations are obtained:

Continuity equation: $$\rho_1 u_1 A_1 = \rho_2 u_2 A_2$$ Equation 2.8

Momentum equation:

$$p_1 A_1 + \rho_1 u_1^2 A_1 + \int_{A_1}^{A_2} p dA = p_2 A_2 + \rho_2 u_2^2 A_2 \qquad \text{Equation 2.9}$$

Energy equation:

$$h_1 + \frac{u_1^2}{2} = h_2 + \frac{u_2^2}{2} \qquad \text{Equation 2.10}$$

### 2.2.3 Area – Velocity Relation

After combining the conservation equations for nozzle flow in differential form, following relation is obtained:

$$\frac{dA}{A} = (M^2 - 1)\frac{du}{u} \qquad \text{Equation 2.11}$$

Equation 2.11 is called area – velocity relation, and it provides wealth of information regarding the flow through nozzle.

- For subsonic flow i.e. $0 \leq M < 1$, a decrease in area i.e. converging section (negative dA) is required to increase the velocity (positive du), and vice versa.
- For supersonic flow i.e. $M > 1$, an increase in area i.e. diverging section (positive dA) is required to increase the velocity (positive du), and vice versa.
- For sonic flow i.e. $M = 1$, Equation 2.11 yields $dA/A = 0$, this indicates to the area being either minimum or maximum, of which minimum area is only practically possible.

In summary, for a compressible fluid to accelerate to supersonic speed from subsonic speed, it needs to flow through a convergent – divergent duct. The gas accelerates from subsonic speed to sonic speed in the convergent section, attains sonic velocity at the region of minimum area (also called throat) and further accelerates from sonic speed to supersonic speed in the divergent section. Similarly, for gas to flow from supersonic speed to subsonic speed too, it needs to flow through convergent – divergent duct, wherein the velocity decreases to sonic speed in convergent section and further decreases to subsonic speed in the divergent section.

### 2.2.4 Isentropic Subsonic – Supersonic Flow Through Nozzles

For the duct shown in the Figure 2.7 , the flow is sonic at the throat. These conditions represented by an asterisk i.e. $M^* = 1$ and $u^* = a^*$ at throat. At other regions of the nozzle, the cross - sectional area, Mach number, speed, density, pressure and temperature are A, M, u, ρ, P and T respectively. Similarly, $\rho_0$, $P_0$ and $T_0$ represent the stagnation density, pressure and temperature respectively.

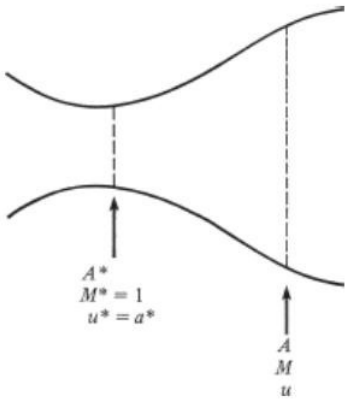


Figure 2.7: Geometry of diverging section of CD nozzle

The alternative forms of energy equation can be written for isentropic flow through the nozzle as follows:

$$\frac{T_0}{T} = 1 + \frac{\gamma - 1}{2} M^2 \qquad \text{Equation 2.12}$$

$$\frac{P_0}{P} = \left(1 + \frac{\gamma - 1}{2} M^2\right)^{\frac{\gamma}{\gamma - 1}} \qquad \text{Equation 2.13}$$

$$\frac{\rho_0}{\rho} = \left(1 + \frac{\gamma - 1}{2} M^2\right)^{\frac{1}{\gamma - 1}} \qquad \text{Equation 2.14}$$

On applying these equations for sonic condition, we get following equations:

$$\frac{T_0}{T^*} = 1 + \frac{\gamma - 1}{2} \qquad \text{Equation 2.15}$$

$$\frac{P_0}{P^*} = \left(1 + \frac{\gamma - 1}{2}\right)^{\frac{\gamma}{\gamma-1}}$$ Equation 2.16

$$\frac{\rho_0}{\rho^*} = \left(1 + \frac{\gamma - 1}{2}\right)^{\frac{1}{\gamma-1}}$$ Equation 2.17

On using continuity equation and energy equation we obtain following equation:

$$\left(\frac{A}{A^*}\right)^2 = \frac{1}{M^2}\left[\frac{2}{\gamma+1}\left(1 + \frac{\gamma - 1}{2}M^2\right)\right]^{\frac{(\gamma+1)}{(\gamma-1)}}$$ Equation 2.18

Equation 2.18 is called area – Mach relation and it implies that anywhere in the duct, the Mach number depends on the ratio of local duct area and the sonic throat area. (Anderson, 2021). From Equation 2.11, A needs to be larger than or at least equal to $A^*$, the condition where $A < A^*$ is physically impossible in an isentropic flow. Also from Equation 2.18, there exists two values of Mach number for a given $A/A^* > 1$, a subsonic and a supersonic value as shown in the Figure 2.8.

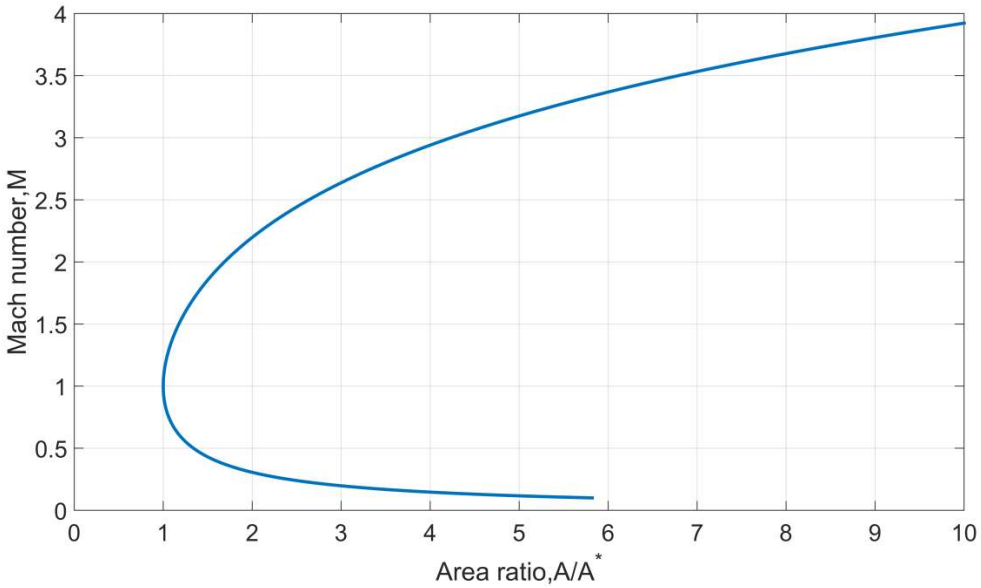


Figure 2.8: Area - Mach number relation

### 2.2.5 Role of Back Pressure on the Flow Through a CD – Nozzle

There is just no guarantee at all that a fluid will accelerate to supersonic velocity when forced through a converging-diverging nozzle. If the back pressure does not happen to be within the proper range, the fluid will in fact slow down within the diverging section rather than accelerate. The nature of the nozzle flow is dictated by the overall pressure ratio $P_b/P_0$. Therefore, the back pressure $P_b$ controls the flow through a converging-diverging nozzle under specific inlet conditions. (Çengel & Cimbala, 2006). This phenomenon is discussed below:

- For $P_0 > P_b > P_c$, the flow from the nozzle remains subsonic and the mass flow rate is also lower than that for the choked flow. In this case, the flow velocity raises in the first part of the nozzle and reaches maximum at the throat (but not sonic). This increase in velocity however is lost in the divergent part as it acts as a diffuser instead of nozzle.
- For $P_b = P_c$, the flow in the converging part accelerates to sonic speed at the throat. The divergent part, however, still behaves as a diffuser slowing the flow to subsonic speed. The flow rate reaches its maximum value and does not vary on further decreasing the back pressure and thus the nozzle is said to have reached condition of chocked flow. The normal shock moves downstream away from the throat as $P_b$ is decreased, and it approaches the nozzle exit plane as $P_b$ approaches $P_E$ (Çengel & Cimbala, 2006).
- When $P_b = P_E$, the normal shock is formed at the exit of the nozzle. In this instance, the entire diverging segment has supersonic flow, which is about isentropic. But as it passes over the typical shock, the fluid velocity decreases to subsonic levels immediately before exiting the nozzle.
- When $P_E > P_b > 0$, the flow in the diverging section becomes supersonic, and the fluid expands to $P_F$ at the nozzle exit without any normal shock formation within the nozzle and as such, the flow through the nozzle can be assumed to be isentropic. When $P_b = P_F$, no shocks occur inside and even outside of the nozzle and the condition is called perfectly expanded jet. When $P_b < P_F$, the jet is under - expanded and there occurs irreversible mixing and expansion waves behind the exit of the nozzle. When $P_b > P_F$, the jet becomes over – expanded and following

the nozzle exit, the fluid's pressure irreversibly rises from $P_F$ to $P_b$, producing what are known as oblique shocks (Çengel & Cimbala, 2006).

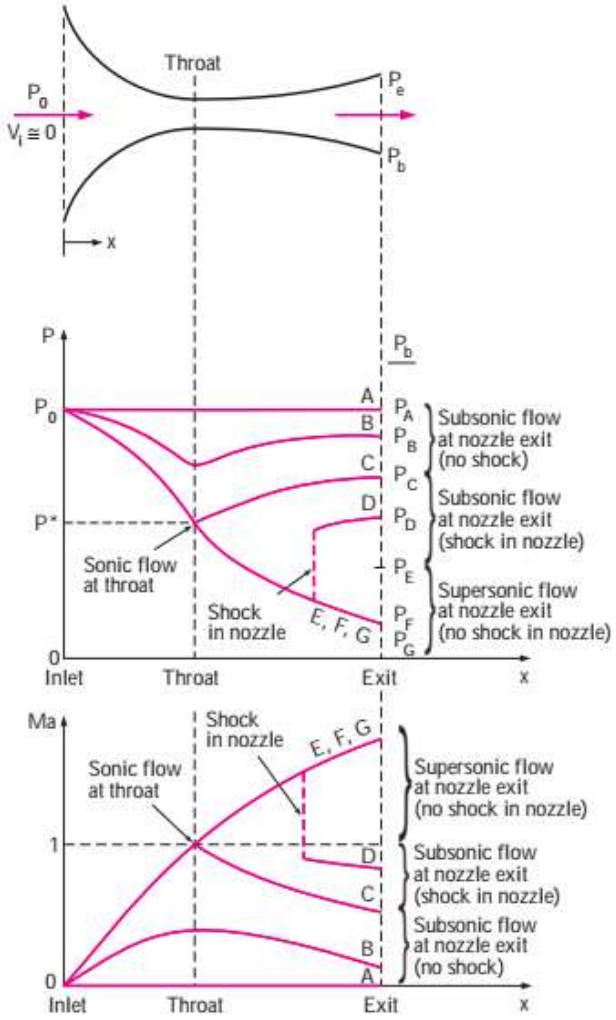


Figure 2.9: The effects of back pressure on the flow through a CD – nozzle *(Çengel & Cimbala, 2006)*

### 2.3 Thrust Vectoring

The basic idea behind thrust vectoring (TV) technology is to divert the aircraft's thrust direction. It is dependent upon a working fluid, or a source installed on the aircraft, and an exhaust nozzle on the engine that serves as a conduit for the fluids. In an aircraft, TV is accomplished by two techniques. The most modern approach uses fluidic-based thrust

vectoring techniques, whereas the conventional way uses mechanical means to deflect the exhaust gases' flow direction.

### 2.3.1 Mechanical thrust vectoring (MTV)

This is a technique of thrust vectoring wherein the vectoring is achieved mechanically by changing the orientation of the engine nozzle exit. The direction of thrust from the nozzle is varied using actuators and gimbaling mechanisms. Despite producing effective thrust vectoring, MTV suffers from disadvantages such as becoming heavy, complex and expensive (Afridi, Khan, Ali Shah, Shams, Mohiuddin, & Kukulka, 2023).

### 2.3.2 Fluidic Thrust Vectoring (FTV)

In order to solve the integration problem and inefficiency of MTV, fluidic thrust vectoring (FTV) technologies were designed and explored. FTV is a technology that uses a secondary flow source in order to manipulate the flow exhaust of an engine nozzle. They provide benefits of engine airframe integration, increased reliability, and decreased weight in comparison to MTV (Afridi, Khan, Ali Shah, Shams, Mohiuddin, & Kukulka, 2023).

Till date, seven different mechanisms for FTV control have been explored. These control systems are

- **Shock Vector Control**

  This technique utilizes a secondary fluid injection in the divergent portion of the CD – nozzle. An oblique shock wave is produced by the injected flow's disturbance because of the low-pressure area downstream of the injection port. The flow is supersonically deflected by the interaction between the oblique shock wave and the primary flow, producing thrust vectoring.

- **Bypass Shock Vector Control**

  A bypass channel flow SVC was designed to reduce the impact of secondary injection and increase the thrust vectoring angle with the least amount of thrust loss. The bypass flow rate was managed via a control valve. The thrust vectoring angle was found to increase in tandem with an increase in the bypass flow rate.

- **Counter Flow Control**

  It involves the penetration of a secondary fluidic flow in the direction opposite to that of the primary flow. The application of suction in the counter flow technique typically results in the creation of a secondary fluidic flow stream and an asymmetric flow in the primary fluid.

- **Co-Flow Control**

  The Coanda effect is used in this concept to facilitate TV through a secondary fluidic flow source. This technique controls the major flow vectoring by means of a tangential injection. A distinct air stream is added to the main flow to cause this phenomenon, which uses the Coanda effect to cause the main flow to curve.

- **Throat Skewing Control (TSC)**

  The theory of throat skewing control pertains to the infiltration of an additional fluidic flow, which causes throat shifting and thrust vectoring. The main flow turns as a result of asymmetric pumping at the neck. By regulating the secondary fluidic flow injection at the nozzle's flap and throat, the TSC nozzle can provide thrust vectoring under all operating conditions.

- **Dual Throat Nozzle (DTN)**

  It is designed to further enhance the throat skewing thrust vectoring technology. Its foundation is the separation control-based throat-shifting nozzle concept. It is comprised of a recessed cavity situated between the CDC nozzle and two minimum areas, one upstream and one downstream. By injecting a secondary fluidic flow into the upstream minimal region, a new area is formed downstream of the flow. The sonic plane, which divides the flow in the hollow near the injection, is skewered by the formation of a new area downstream.

- **Bypass Dual Throat Nozzle Control (BDTN)**

  The evolution of BDTN was based on the traditional DTN, which suffered little loss of thrust, immense thrust vectoring effectiveness, and little analytical modeling. Since the BDTN did not utilize a secondary fluid from the fan or engine compressor, it typically had little or no impact on thrust loss. The convergent-divergent-convergent nozzle's upstream throat is where the bypass is inserted. By creating flow separation in the cavity, the secondary flow passing

through the bypass diverts the nozzle's primary flow. Without sacrificing the discharge coefficient, thrust efficiency, or thrust coefficient, BDTN can achieve a high thrust deflection angle. Because of this, BDTN became more appealing for achieving high vectoring angles and little thrust loss (Afridi, Khan, Ali Shah, Shams, Mohiuddin, & Kukulka, 2023).

Out of all these vectoring controls, counter-flow control regulates the primary flow deflection by using the suction concept. To regulate the principal flow deflection, the remaining control strategies, however, rely on the blowing principle (Afridi, Khan, Ali Shah, Shams, Mohiuddin, & Kukulka, 2023). The different methods of FTV are shown in Figure 2.10.

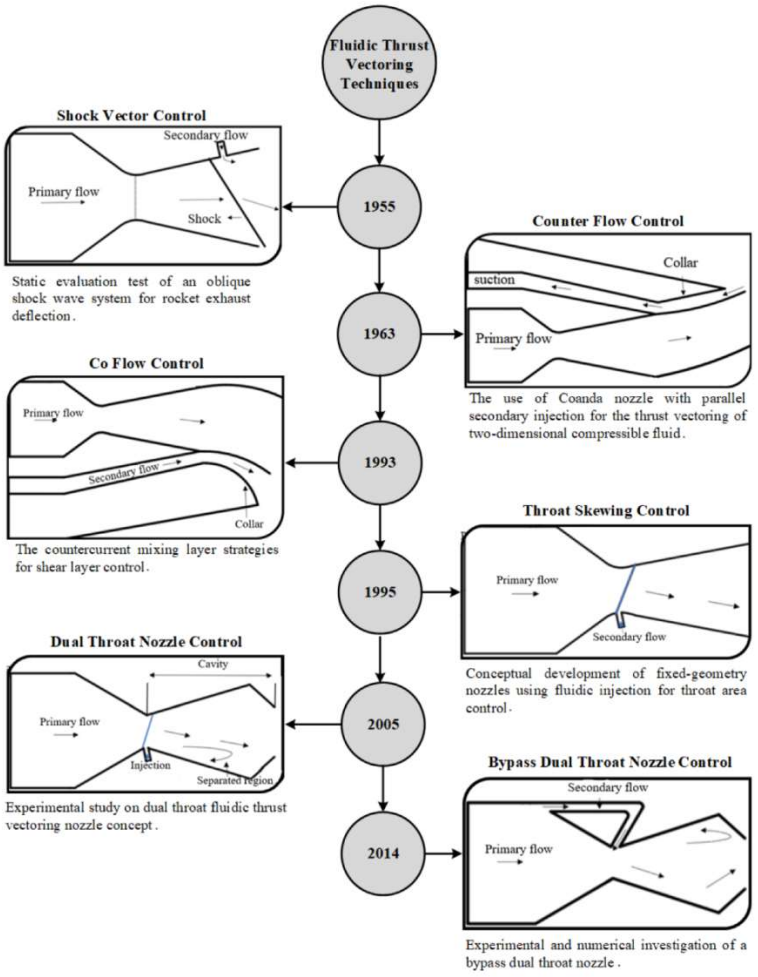


Figure 2.10: History of fluidic thrust vectoring controls techniques *(Afridi, Khan, Ali Shah, Shams, Mohiuddin, & Kukulka, 2023)*

## 2.4 Previous Works

### 2.4.1 Studies on Design and Development of Schlieren Imaging Setup

(Prisăcariu, Vilag, Nicoară, Suciu, Dobromirescu, & Dombrovschi, 2020) defined the parameters that need to be taken into consideration while setting up a Schlieren system. Its goals were to provide choices for optical route components, point to the best equipment, and follow and explain a mathematical approach that may be used to pre-set a system.

(Sopeña i Martínez, 2014) put together the Schlieren visualization device and characterizes it. Various configurations were put together to talk about the best setup. Many factors were considered, such as the kind of light source, the focal length, and the knife edge cutoff. In the end, the gadget was put to the test under harsh circumstances by using it to simulate an electric spark's sound wave. This enabled the researcher to ascertain its velocity and, thus, validate that the perturbation that was visualized does, in fact, correspond to a sound wave.

(Maharjan, 2023) fabricated a portable experimental setup of the z-type schlieren technique that fits on a 90 cm by 90 cm benchtop. It was made up of two reflecting telescope parabolic mirrors with a 400 mm focal length and 76 mm diameter. This configuration allowed for the qualitative and quantitative study of various fluid flow phenomena. The flow phenomena illustrated using this setup were under-expanded jet from a converging-diverging nozzle and negatively buoyant plumes in water. The phenomena that were visualized span from subsonic to supersonic characteristics.

### 2.4.2 Studies on Numerical and Experimental Analysis of Shock Vector Control

(Saito & Fujimoto, 2009) investigated a fluidic thrust vectoring system with a secondary jet injected into the main nozzle flow numerically. The numerical results were compared with (Waithe & Deere, 2003) experimental data. The numerical analysis was carried out using two – dimensional Navier – Strokes equations with the Spalart – Allarmas turbulence model. The result showed the need for using appropriate turbulence models in order to study the details of fluidic thrust vectoring.

(Wu & Dong Kim, 2019) systematically carried out the investigation of SVC system on rectangular supersonic nozzle. The effects of the momentum flux ratio, length – to – width ratio, injection angle and injection location on vectoring parameter; namely pressure distributions along the upper and lower nozzle surfaces, deflection angle, resultant thrust coefficient, and thrust efficiency were studied. The computational results were then compared with the experimental data for validation of the numerical method used. Following conclusions were drawn from the study:

- With the increase in the momentum flux ratio, the thrust vector deflection angle increased due to stronger shock interactions whereas the thrust coefficient and efficiency decreased because of the loss in the primary flow.
- Larger length – to – width ratio increased the thrust vector angle while reducing the thrust coefficient. Higher length – to – width ratio was found to be more efficient in generating thrust deflection with lower injection pressure requirement.
- Moving the injection location upstream (closer to the nozzle throat) increased the deflection angle whereas the thrust coefficient increased while moving the location downstream.
- The optimal injection angle for maximum deflection was found to be $120^0$. Larger injection angles (>120°) decreased the thrust vector angle, while smaller angles (<120°) reduced effectiveness.

(Waithe & Deere, 2003) carried out computational and experimental study to investigate the effects of multiple injection ports in a two – dimensional, convergent divergent nozzle, for fluidic thrust vectoring. The experimental study investigated the internal nozzle performance for nozzle pressure ration (NPR) ranging from 1 to 10 with secondary pressure ratio up to 5 for five different configurations. The computational analysis was carried out using Reynolds Averaged Navier-Stokes computational fluid dynamics code PAB3D with two-equation turbulence closure and linear Reynolds stress modeling. Nozzle performance was predicted for nozzle pressure ratios up to 10 with secondary pressure ratio of 0.7 for two configurations. The study concluded that the multiple injection as beneficial up to nozzle pressure ratio of 4 with higher secondary pressure ratios. Results from the computational study were also found to be in an

excellent agreement with the experimental results signaling to the use of PAB3D as a tool for predicting internal nozzle performance of a 2- D CD nozzle with multiple injection ports.

(Shakouchi & Fukushima, 2022) proposed a simple method for the thrust vector control of a supersonic jet by a Fluidic Coanda nozzle (FC – nozzle). The flow characteristics and deflection characteristics of the supersonic jet from the FC-nozzle were examined by the visualized flow pattern using the Schlieren method and measurements of the velocity distribution. The research demonstrated that by changing the number of Suction pipes and the locations at which they are closed, the deflection angle and circumferential position of the jet from the Pi-nozzle could be easily controlled.

# CHAPTER THREE : RESEARCH METHODOLOGY

## 3.1 Research Nature

The research study is classified as empirical research because it is an experimental study. The researcher's personal experiences with fluid-flow phenomena serve as the basis for observation and measurement. This study uses the Mach contours produced by numerical analysis performed in a commercial software program (ANSYS Fluent) and Schlieren images. They are contrasted with one another as well as with a well-established fluid-flow theory. Although secondary data from a literature review might be taken into consideration in certain instances, the data collected would be primary data. The research uses a deductive methodology, taking into account a theoretical understanding of the fluid-flow phenomenon and testing it in a manufactured Schlieren setup to confirm the sensitivity and correctness of the results.

## 3.2 Overview of Methodology

The proposed methodology for the research work is shown in the Figure 3.1.

## 3.3 Literature Review

It was the first phase in the research methodology. It was conducted with the help of different books, academic reports from campus library and scholarly articles. In this paper, the book ‘Schlieren and Shadowgraph Techniques’ of G.S. Settles was mainly used as a source for general schlieren systems. During the course of this research, number of works from various researchers were referred and borrowed, especially the works related to Schlieren imaging and its setup, design and analysis of CD – nozzle, fluidic thrust vectoring for the CD – nozzle and experimentation using Schlieren setup.

## 3.4 Construction Schlieren Imaging Setup

The Schlieren technique requires a precise experimental setup in order to produce a uniformly lit monochromatic image on the camera and in the cutoff plane. This covers the entire process, from deciding where to put the Schlieren setup to selecting specifics like the cutoff type, mirrors, light source, and camera. All these were dealt individually and meticulously in order to construct the setup that provided high quality Schlieren images.

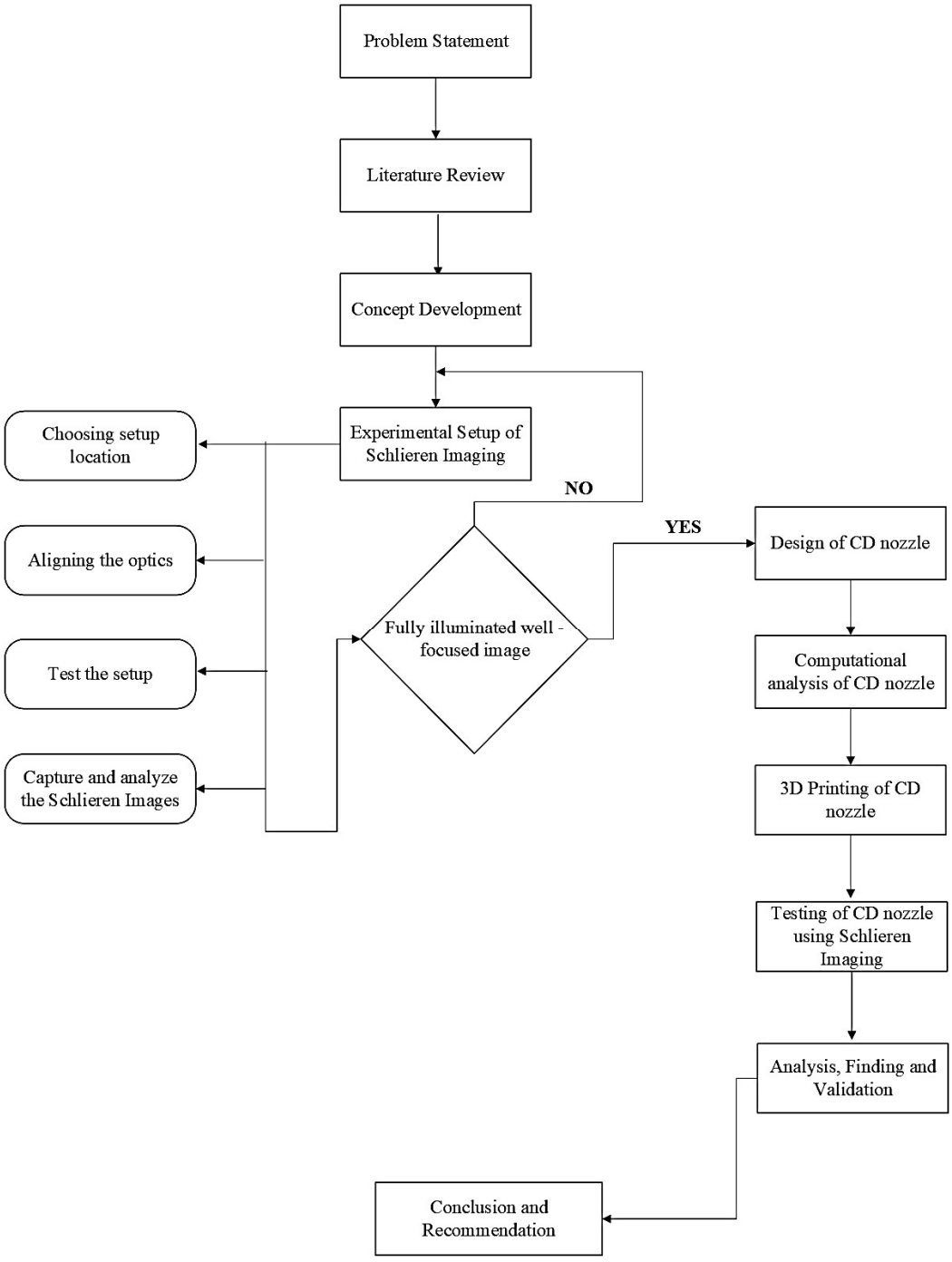


Figure 3.1: Flowchart for research process

### 3.5 Design of Converging – Diverging (CD) Nozzle with Fluidic Thrust Vectoring

A 2 dimensional CD nozzle was designed for Mach number of 2. The contour and dimensions for the convergent part were assumed while the contour for the divergent part was determined using Method of Characteristics (MOC). Among various types of fluidic thrust vectoring methods, shock vector control (SVC) was taken for this study.

### 3.6 Numerical Simulation of Flow through the nozzle

The numerical simulation of CD nozzle with SVC was carried out using ANSYS fluent software package. During the simulation, the location of the secondary inlet, nozzle pressure ratio and secondary pressure ratios were varied to observe the thrust vectoring angle.

### 3.7 Testing of CD Nozzle Using Schlieren Setup

The designed nozzle was 3 D printed using fused deposition modeling. Furthermore, test rig was setup to visualize and capture the intricacies in the fluid flow from nozzle using the Schlieren setup constructed.

### 3.8 Findings and Reporting

The results from numerical analysis and experimentations were analyzed and compared both qualitatively and quantitatively. All the findings were documented and reported in the final report.

### 3.9 Conclusions and Recommendations

After analyzing all the findings, conclusions were drawn and further works were recommended for future researches in the field of Schlieren imaging and fluidic thrust vectoring.

# CHAPTER FOUR : SCHLIEREN IMAGING SETUP

## 4.1 Experimental Setup and Equipment

A single mirror Schlieren imaging setup consist of four components; a concave mirror, light source, knife edge and camera.

### 4.1.1 Mirror and Mirror Mount

A telescopic parabolic mirror of following specification is used for the setup:

Table 4.1: Specification of the mirror used

| | |
|---|---|
| Mirror type | Concave parabolic mirror |
| Diameter | 206 mm |
| Focal length | 1260 mm |
| Thickness | 20 mm |

The mirror is placed on a simple 3D printed mirror mount as shown in the Figure 4.1.

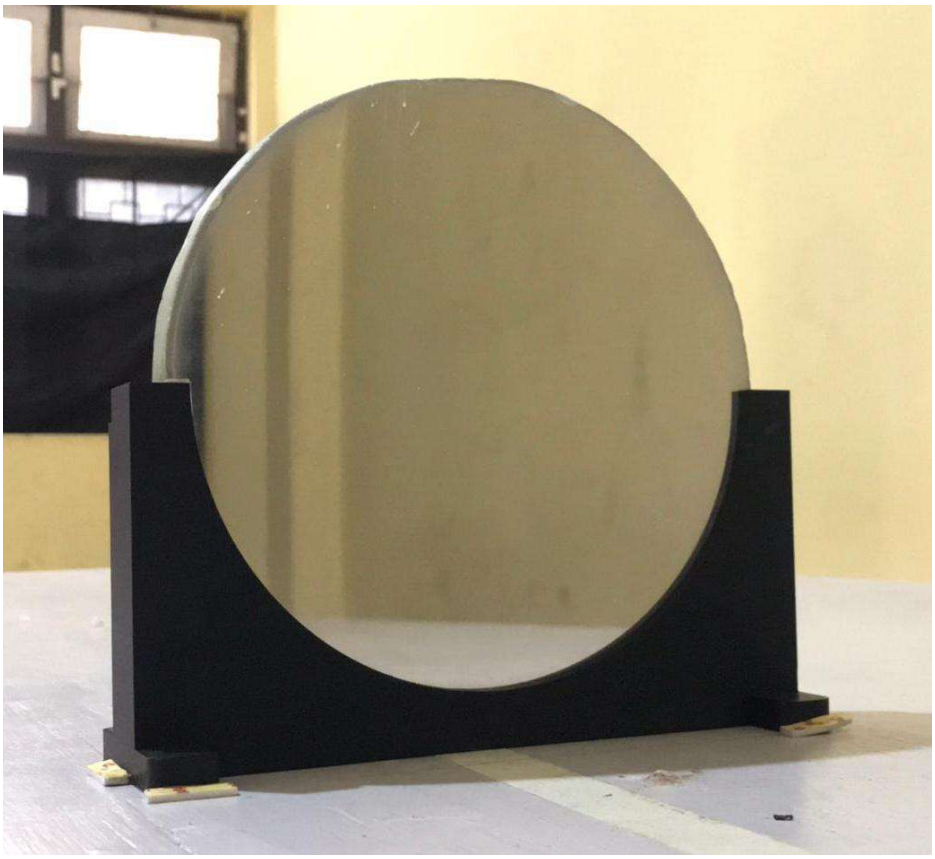

Figure 4.1: Parabolic mirror along with 3D printed mirror mount

### 4.1.2 Light source

A bright white LED diode bulb with heat sink of following specification was used as the light source for the setup:

Table 4.2: Specification of light source

| | |
|---|---|
| Power | 3 W |
| DC forward Current (IF) | 700 mA |
| DC forward Voltage (VF) | 2.8 – 3.6 V |
| Beam angle | 120 degrees |
| Life span time | 50,000 hours |

An AC to DC adapter of 4.5 V output was used to power the LED. Due to the higher voltage output of the adapter, a current – limiting resistor of 22 Ω was used to protect the LED. The LED light source along with resistor connected to it is shown in the Figure 4.2.


Figure 4.2: LED source along with resistor connected to limit the current flow

### 4.1.3 Knife Edge

Due to the sharpness of the cutting edge, a paper cutter blade was used as the knife edge to block a part of converged light at focal point after the light has been reflected by the mirror.

### 4.1.4 Light Source and Knife Edge mount with Adjustable cutoff

A mount was modeled and fabricated in the carpentry workshop that housed the light source and knife edge. The mount was fabricated in such a way that the cut – off could be varied by adjusting the height of the knife edge. This helped in testing the sensitivity of the setup. The fabricated mount is shown in the Figure 4.3.

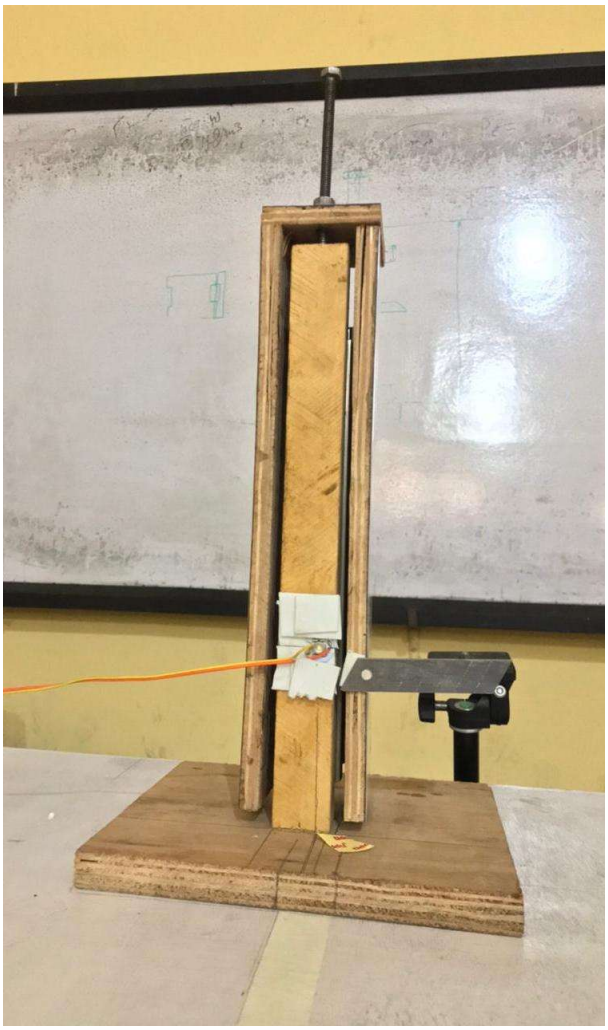

Figure 4.3: A fabricated LED and knife edge mount with adjustable cut - off

### 4.1.5 Camera

A Nikon D3400 DSLR camera with 18 – 270 mm, F/3.5 – 6.3 zoom lens was used to capture the Schlieren images. A large zoom lens was required due to long focal length of the mirror.


Figure 4.4: Camera used for image capturing in the Schlieren setup

### 4.1.6 Complete setup

The mirror with mirror mount and light source and knife edge mounts were placed on table top fabricated locally. The components were placed at calculated distance and adjusted manually to obtain the best arrangement. Once the best arrangement was obtained, the components' positions were marked and secured with the help of tape. The camera was mounted on the camera stand at the edge of the table. The complete setup is shown in the Figure 4.5.

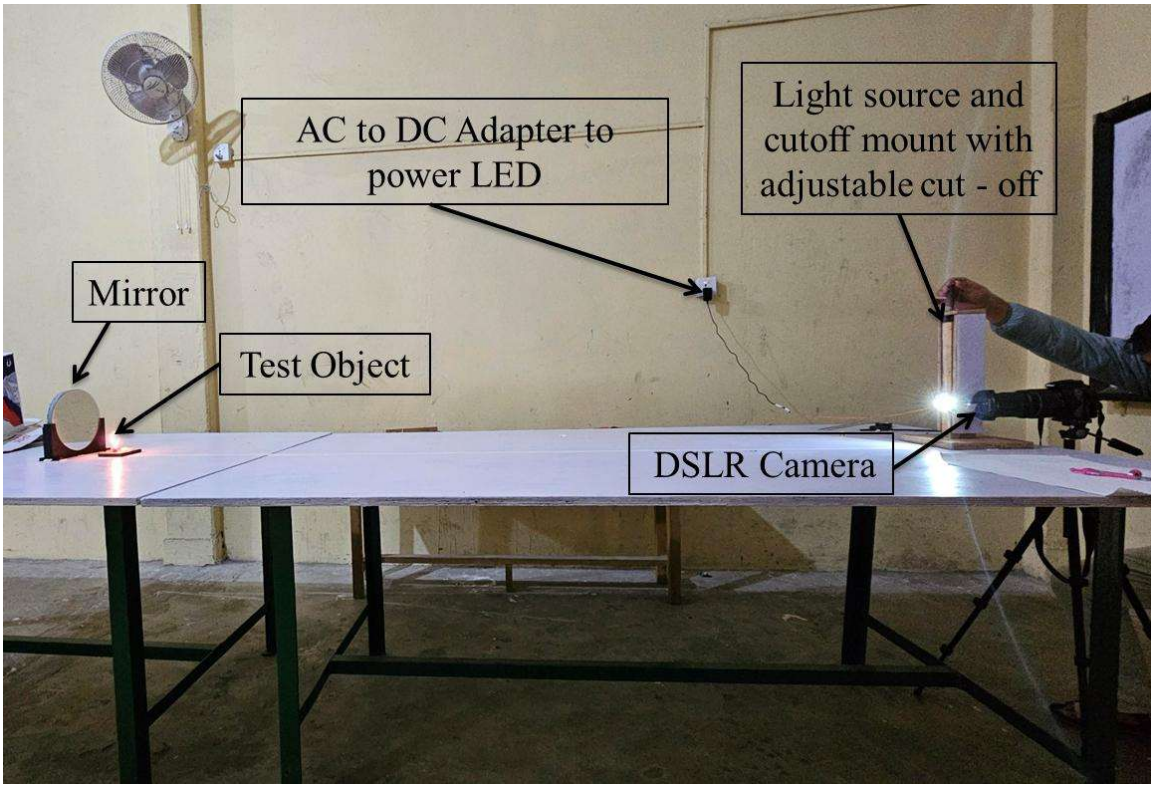


Figure 4.5: A complete single mirror Schlieren setup

### 4.2 Testing of the Schlieren Setup

For the testing of the Schlieren setup, thermal plumes from burning candle and human hand were observed.

#### 4.2.1 Thermal Plume from Burning Candle

A burning candle was placed at the test section and the thermal plume emitted by the burning candle was captured using camera. The cutoff was varied by adjusting the height of the knife edge and the sensitivity of the setup was checked. All the images were captured at the same setting of the camera. The setting taken was f/6.3, 1/2000 sec and ISO 100. The images obtained during testing are shown in Figure 4.6. It was observed from the images that the Schlieren imaging setup constructed was able to capture the intricacies of the thermal plumes emitted from the burning candle. The cut – offs could be adjusted to obtain clear images.

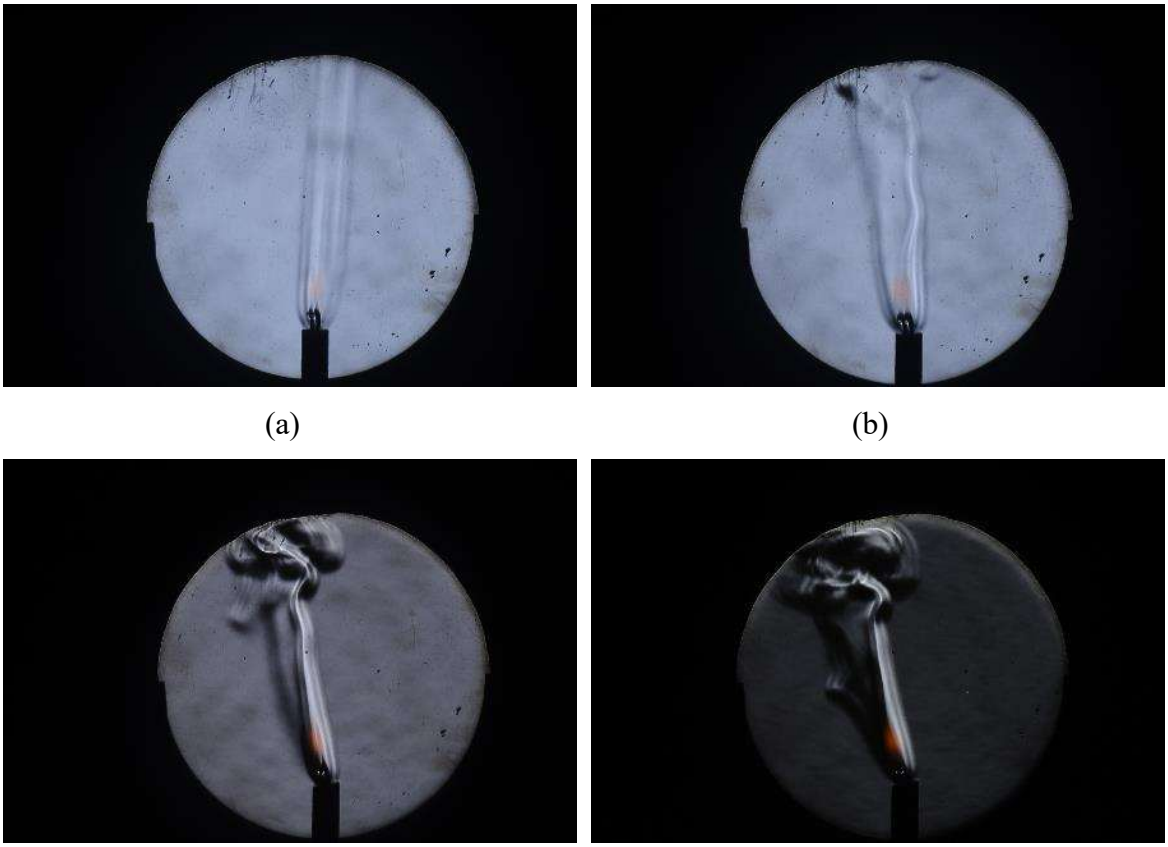

(a) (b)

(c) (d)

Figure 4.6: Schlieren images of thermal plume from candle at different cut - offs. (a) 0%, (b) 20%, (c) 79% and (d) 94%

### 4.2.2 Thermal Plumes from Human Hand

Human hand was placed in the test section and the hot air rising from the hand due to natural convection was observed. The test result is shown in the Figure 4.7.

Figure 4.7: Schlieren image of hot air rising from hand

# CHAPTER FIVE : DESIGN, NUMERICAL SIMULATION AND EXPERIMENTAL ANALYSIS OF CD - NOZZLE

This chapter deals with the design, numerical simulation and experimental analysis of CD – nozzle for exit Mach number of 2.

## 5.1 Design Parameters

The design parameters were selected such that they could be realized easily in practical scenario. Following design parameters were chosen for the design of a convergent – divergent nozzle:

Table 5.1: Input design parameters

| | |
|---|---|
| Mach number (M) | 2 |
| Gas constant (R) | 287 J/kg.K |
| Specific heat ratio ($\gamma$) | 1.4 |
| Atmospheric pressure ($P_a$) / Exit pressure | 101325 Pa |
| Stagnation temperature ($T_0$) | 300 K |

## 5.2 Thermodynamic Parameters

### 5.2.1 Inlet Chamber Condition

For large inlet chamber, the flow velocity could be considered to be zero and thus the properties in the inlet chamber correspond to stagnation properties (i.e. $P_c = P_0$, $T_c = T_0$, $\rho_c = \rho_0$). Using Equation 2.13 , for exit pressure ($P_e$) = 101325 Pa and exit Mach number = 2, it was obtained that

$$P_0 = 7.824 \times P_e = 792766.8 \text{ Pa}$$

Similarly, using ideal gas equation, density of the air was determined as follows:

$$\rho_0 = \frac{P_0}{R \times T_0} = 9.2075 \text{ kg/m}^3$$

### 5.2.2 Nozzle Throat Conditions

Using Equation 2.15, Equation 2.16 and Equation 2.17 to calculate the throat properties, following values were obtained:

Table 5.2: Thermodynamic properties at throat

| | |
|---|---|
| Temperature at throat ($T^*$) | 250 K |
| Static pressure at throat ($P^*$) | 418804.26 Pa |
| Density at throat ($\rho^*$) | 5.837 kg/m$^3$ |

Sonic velocity at throat was given by

$$a^* = \sqrt{\gamma R T^*} = 316.94 \text{ m/s}$$

### 5.2.3 Nozzle Exit Condition

For exit Mach number (M) = 2 and exit pressure (P) = 101325 Pa, using Equation 2.12 and Equation 2.14 respectively, following thermodynamic properties were obtained at the exit of the nozzle:

Table 5.3: Thermodynamic properties at nozzle exit

| | |
|---|---|
| Exit temperature ($T_e$) | 166.67 K |
| Exit density ($\rho_e$) | 2.118 kg/m$^3$ |
| Exit sonic velocity ($a_e$) | 258.78 m/s |
| Exit velocity ($u_e$) | 517.56 m/s |

Using Equation 2.18, the exit area to throat area ratio was obtained as follows:

$$\frac{A_e}{A^*} = \frac{1}{M}\left[\frac{2}{\gamma+1}\left(1 + \frac{\gamma-1}{2}M^2\right)\right]^{\frac{(\gamma+1)}{2(\gamma-1)}} = 1.6875$$

## 5.3 Nozzle Contour Design

The flow velocity in convergent section of the nozzle is always relatively low in comparison to the diverging section. So, there is no one contour that is superior to another and minimum energy losses can be achieved with well – rounded smoothed convergent nozzle surface (Ranabhat, Darlami, Bhattarai, & Shrestha, 2022). On the other hand, performance of supersonic CD nozzle is dictated by the diverging section due to the fact that there involve very high velocities in the diverging section. The diverging section contour was generated using Method of Characteristics (MOC). A MATLAB code was used to generate the contour coordinate of diverging section as shown in Figure 5.1.

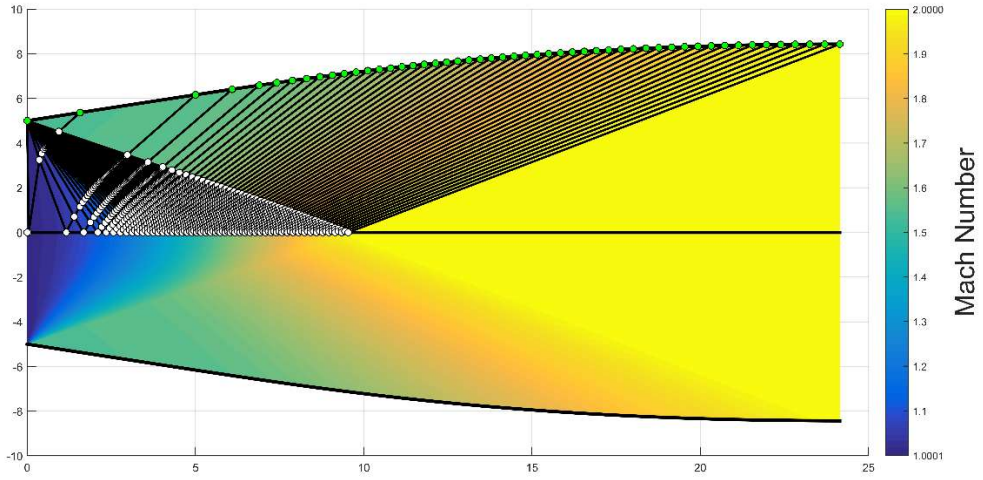


Figure 5.1: Diverging section contour of the nozzle developed using MOC in MATLAB

### 5.4 Numerical Simulation

The numerical simulation was carried out on ANSYS Fluent, which is the CFD solver package of ANSYS 2019 R2 program.

#### 5.4.1 Geometry Creation

The symmetric half geometry of 2 - dimensional nozzle along with the flow domain behind the nozzle exit was modeled in 3D modeling software Solidworks by importing the wall coordinates generated by MATLAB program. The geometry for the flow simulation along with primary dimensions is shown in Figure 5.2.

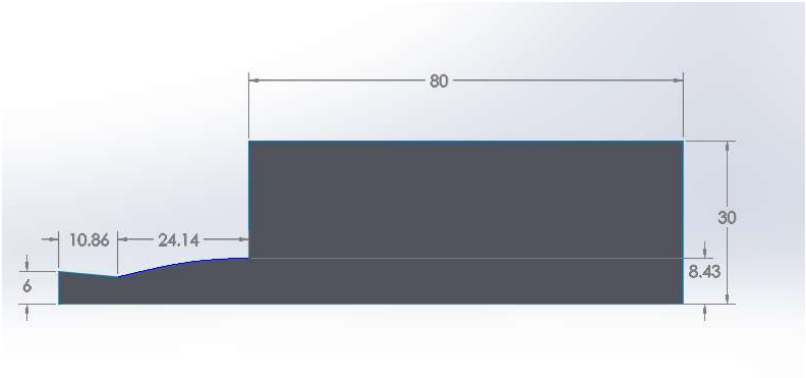


Figure 5.2: Symmetric half of the nozzle along with flow field behind nozzle exit

### 5.4.2 Mesh Creation

The meshing was carried out in ANSYS fluent. Due to 2 - dimensional geometry, structured quadrilateral mesh was used for meshing. The total flow domain was divided into multiple small sub – domains to assist proper meshing. The discretized geometry after meshing is shown in the Figure 5.3.

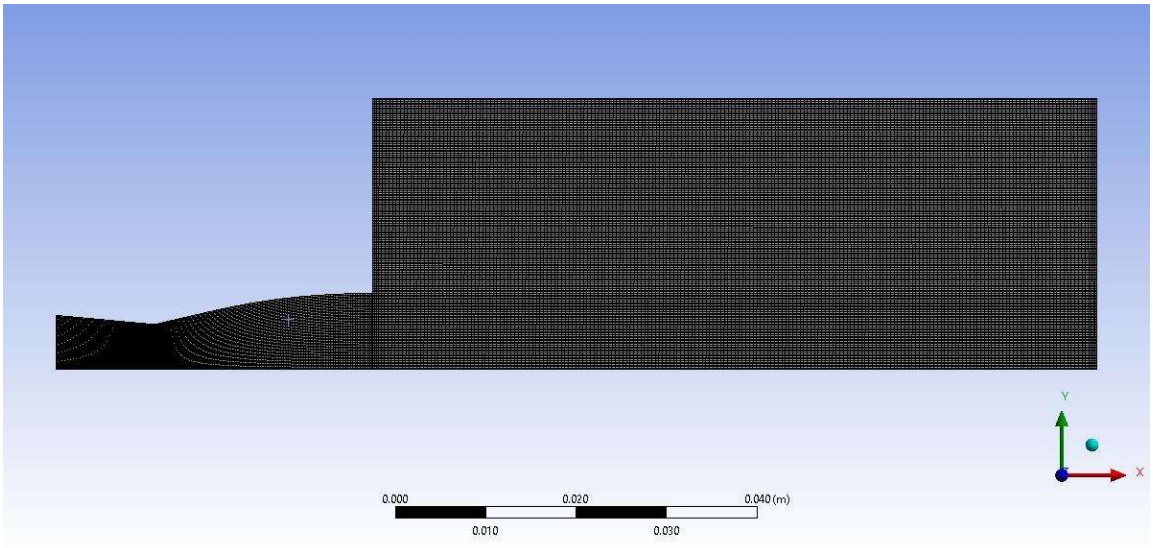


Figure 5.3: Meshing of the flow domain

### 5.4.3 Fluid Domain Setup

The setup used for the numerical simulation is summarized in the Table 5.4.

Table 5.4: Fluid domain setup for CD nozzle

| | | |
|---|---|---|
| General | Type | Density based |
| | Time | Steady |
| | Velocity Formulation | Absolute |
| | 2D – space | Planar |
| Models | Energy | On |
| | Viscous model | k – epsilon (2 equation) realizable |
| | Density | Ideal gas |
| | Viscosity | Sutherland (Three coefficient method) |
| Boundary Conditions | Inlet | Type: Pressure inlet |

| | | |
|---|---|---|
| | | Gauge total pressure : 150000 – 1000000 Pa |
| | | Total temperature: 300 K |
| | Outlet | Type: Pressure outlet |
| | | Gauge pressure: 0 Pa |
| | Wall | Stationary wall |
| | | No slip condition |
| | Center – line | Symmetry |
| Solution Controls | Courant number | Up to 1 |

### 5.4.4 Results

The numerical simulations were carried out in the convergent – divergent nozzle by varying the inlet pressure from 1.5 bars to 8 bars. Some of the Mach contours obtained from the simulation are shown in the Figure 5.4.

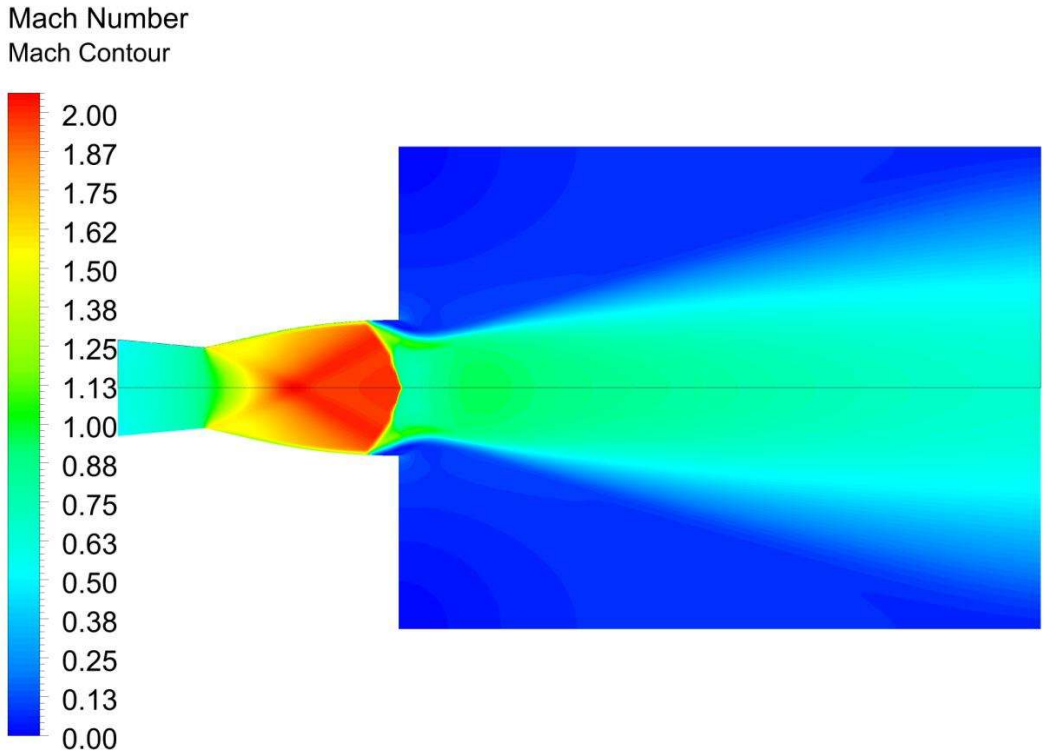


(a)

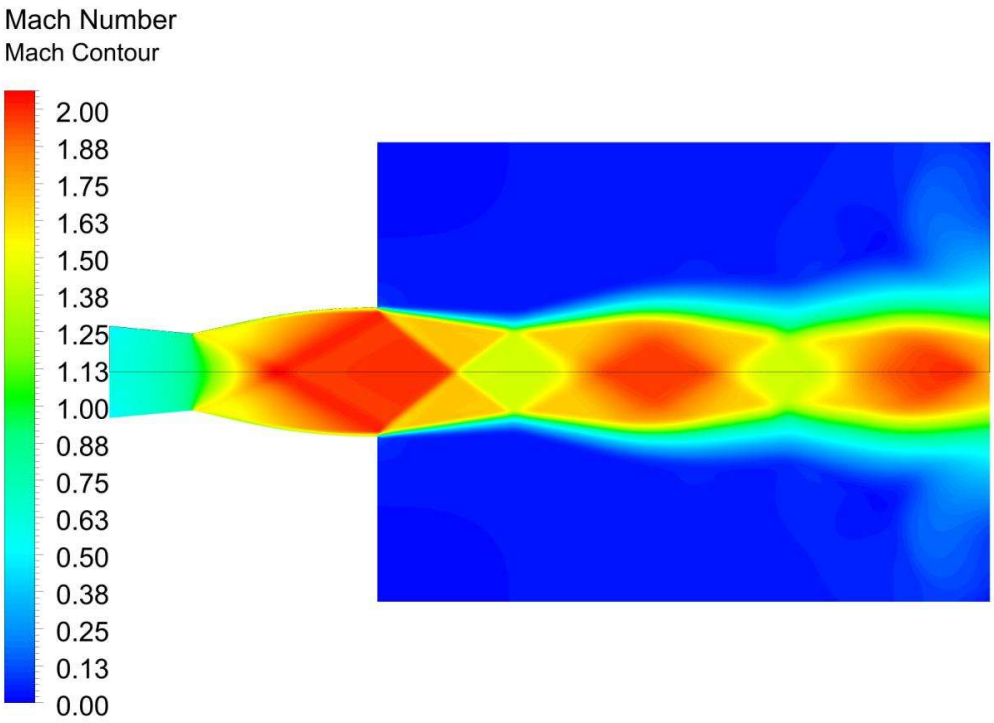


(b)

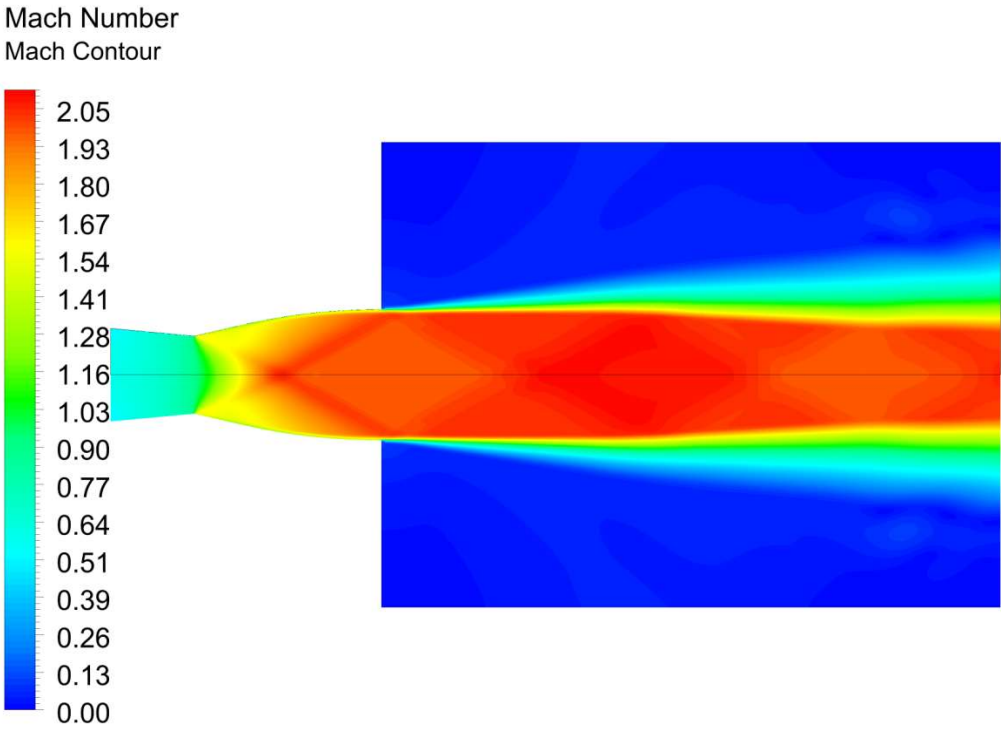


(c)

Figure 5.4: Mach contours at different inlet gauge pressures: (a) 1.5 bar, (b) 4 bar, and (c) 7.5 bar

At lower inlet pressure, a normal shock was formed inside the nozzle as seen in figure 5.4 (a). As a consequence, the velocity of jet emitted from the nozzle became subsonic. On further increasing the inlet gauge pressure, the normal shock shifted towards the nozzle exit and the flow from the nozzle became supersonic. At lower pressures, the jet emitted from the nozzle were found to be over - expanded. Over – expanded jet from the nozzle along with the Mach diamonds is seen in the figure 5.4 (b) where, the gauge inlet pressure was taken to be 4 bar. Similarly, almost perfectly expanded jet is seen in the figure 5.4 (c) for which the gauge inlet pressure was taken to be 7.5 bar.

## 5.5 Experimental Analysis

### 5.5.1 Modeling and Fabrication of CD Nozzle

A planar CD nozzle was modeled in Solidworks in the same dimension as taken for numerical simulation. As the convergent section did not have much effect on the flow behavior in supersonic region, the convergent part of the nozzle was taken to be circular in section. The throat had square section and the divergent section had planar section as shown in the Figure 5.5.

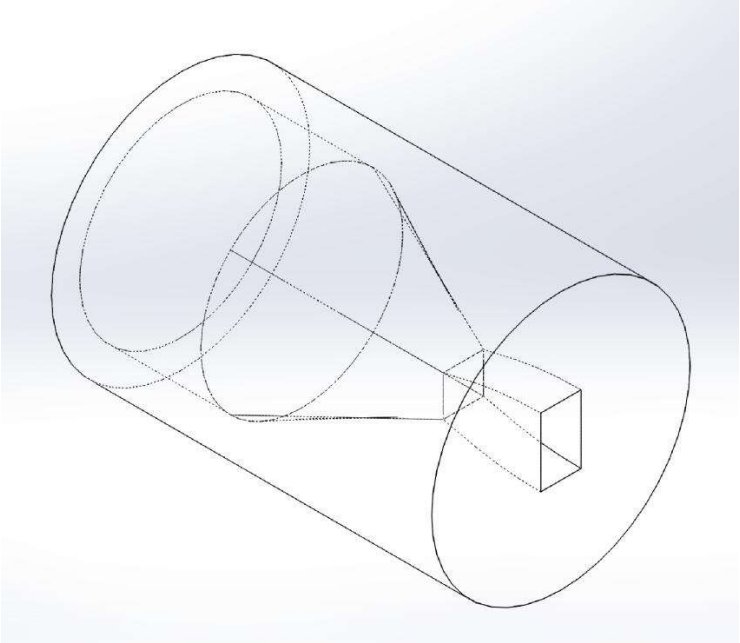

Figure 5.5: 3 D model of the CD nozzle used for 3 D printing

The 3 D modeled nozzle was 3 – D printed using Fused Deposition Modeling (FDM) technique and the material used for printing was Polylactic Acid (PLA). The 3 D printed nozzle in shown in the Figure 5.6.

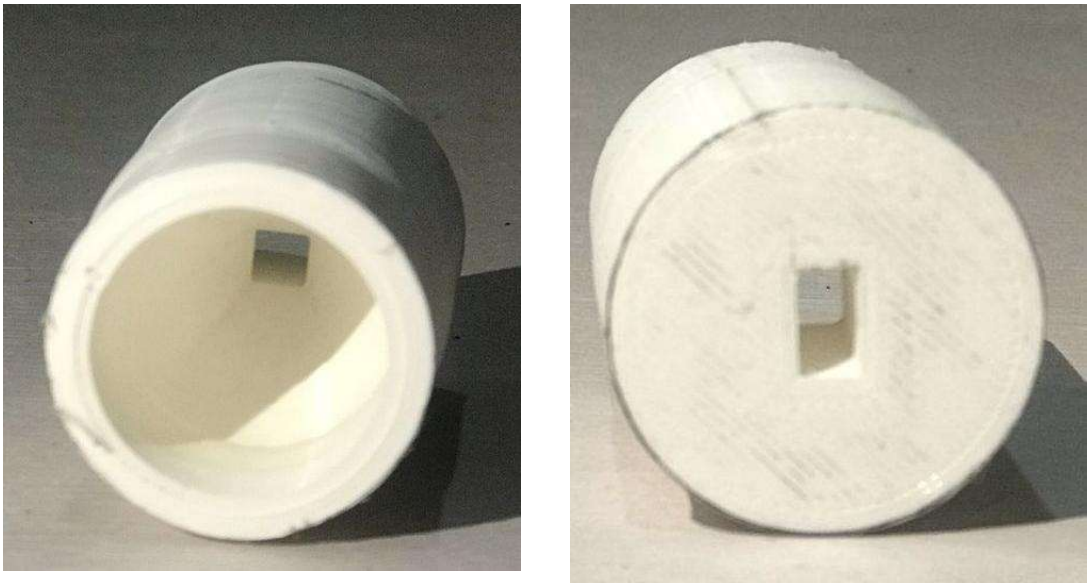

Figure 5.6: 3 D printed nozzle showing the inlet section and exit section

### 5.5.2 Construction of Experimental Test Rig

The experimental test rig consisted of two stage reciprocating compressor with a large reservoir, a stand to hold the nozzle in place and resist the thrust force produced by the nozzle, pneumatic hoses along with its pneumatic attachments and a socket to hold the nozzle in place. The different components are shown in the Figure 5.7.

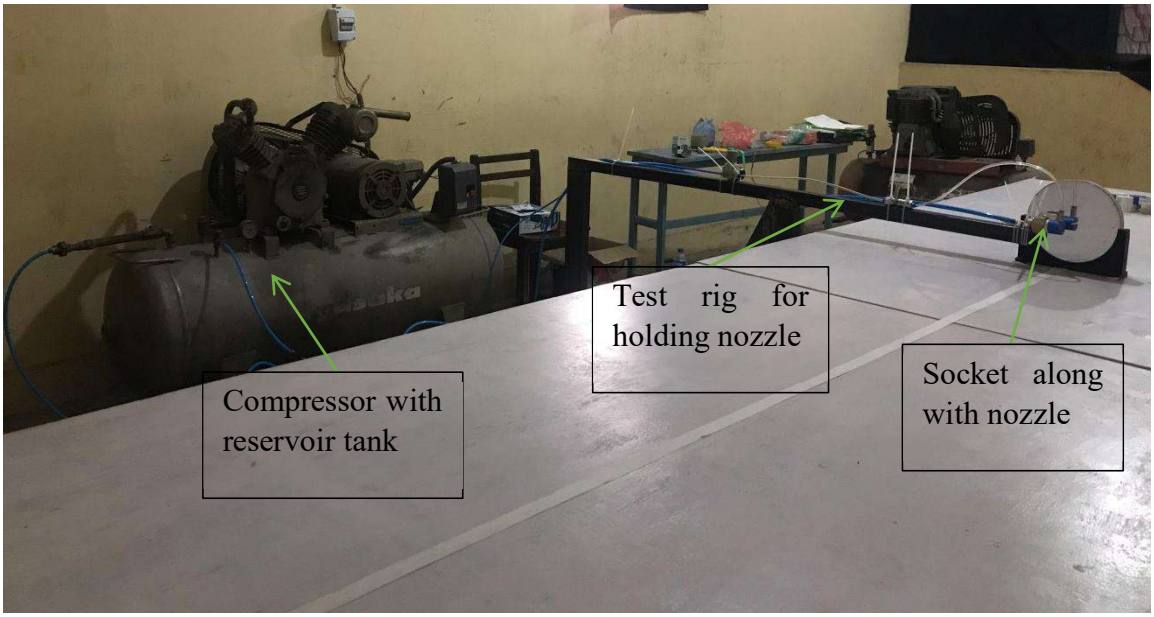


Figure 5.7: Experimental test rig with different components

### 5.5.3 Experimental Results

The compressed air at different inlet pressure was passed through the CD nozzle and the flow behavior of air behind the exit of the nozzle was captured using Schlieren imaging setup.

At lower pressure ratio, over - expanded jet were observed at the exit of the nozzle as shown in the Figure 5.8.

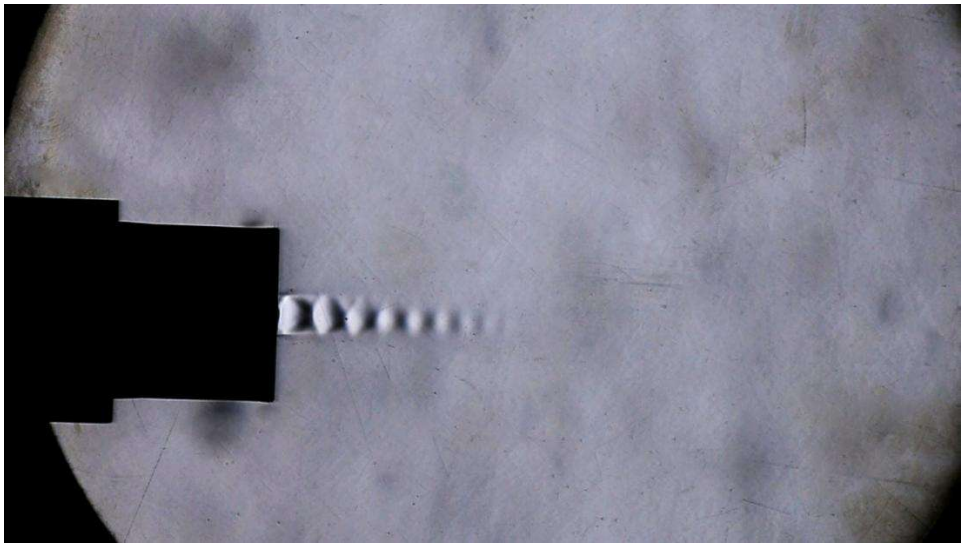

Figure 5.8: Over expanded jet captured by the Schlieren setup at NPR = 7

Similarly, on increasing the inlet pressure, the under expanded jet were observed at the exit of the nozzle. The Mach diamonds that are formed for under expanded jets were clearly seen in the images captured by the Schlieren setup. Some of the images are shown in the Figure 5.9.

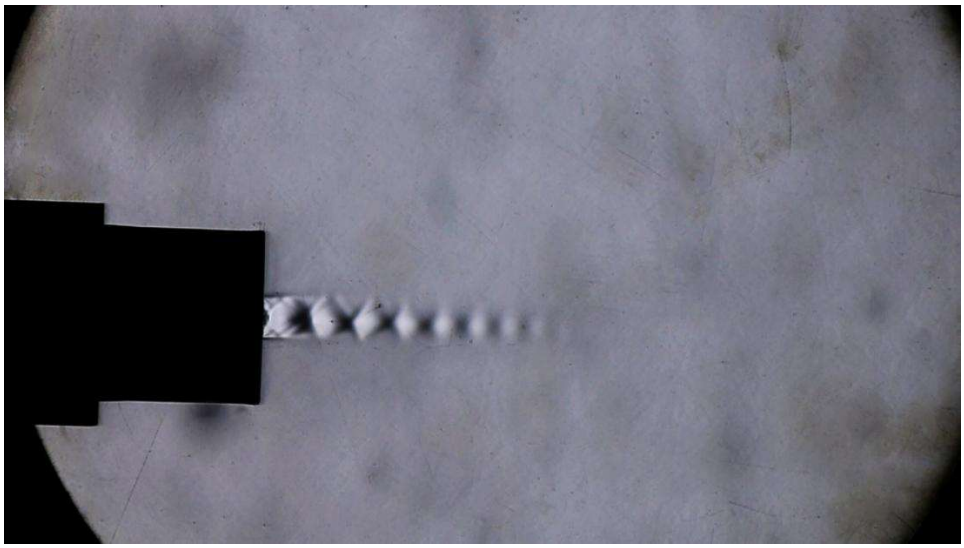

(a)

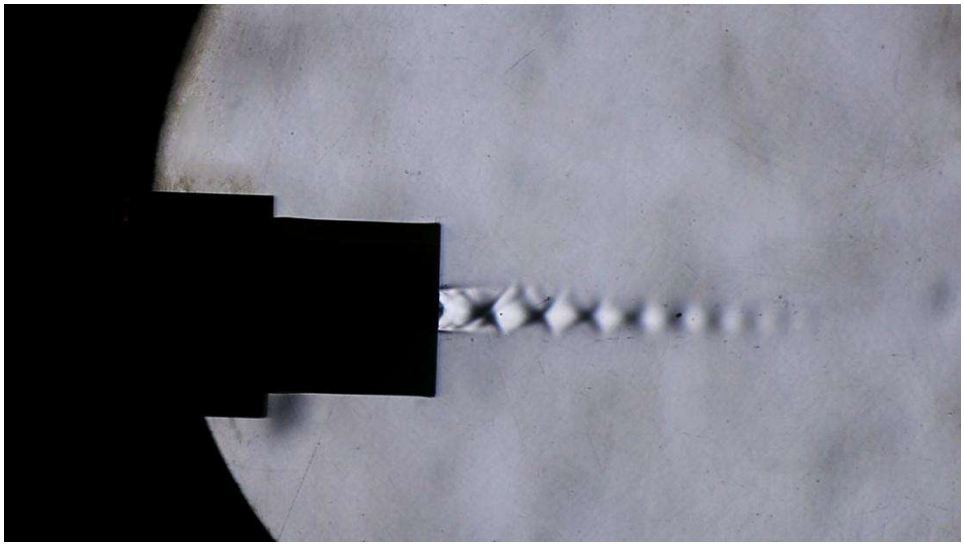

(b)

Figure 5.9: Under expanded flow at the exit of the nozzle as captured by the Schlieren setup at (a) NPR = 9 and (b) NPR =11

# CHAPTER SIX : NUMERICAL SIMULATION AND EXPERIMENTAL STUDY OF SHOCK VECTOR CONTROL

## 6.1 Numerical Simulation of Shock Vector Control

Numerical simulations were conducted to determine the effects of secondary flow location, nozzle pressure ratio (NPR) and secondary pressure ratio (SPR) on thrust vector angle on the CD nozzle designed earlier. Three different secondary flow locations were taken into consideration (at 25 %, 50% and 75%) for this study. The secondary flows were introduced perpendicular to the flow direction in all cases. NPR ratios were varied from 5 up to 11. Similarly, the SPR were varied from 0.1 to 0.7.

### 6.1.1 Geometry Creation

The geometry for the numerical simulation was created in Solidworks and imported to ANSYS in .iges format. The flow domain behind the exit of the nozzle was extended up to 16 throat height in vertical direction and 30 throat heights behind the exit. The geometry of the flow domain with secondary inlet locate at 75% of the throat length is shown in Figure 6.1.

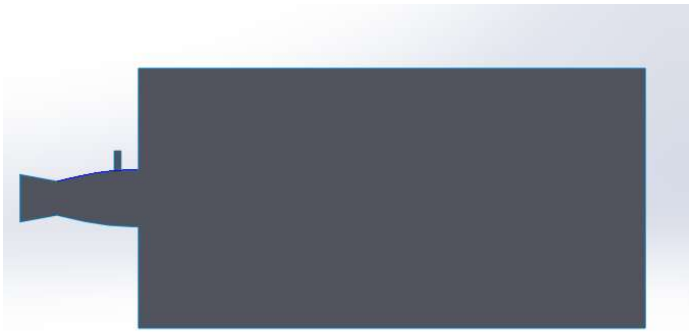

Figure 6.1: Geometry of nozzle along secondary inlet and flow domain behind the nozzle

### 6.1.2 Computational Domain and Boundary Conditions

A 2 – dimensional computational domain was created to conduct the numerical simulations and detailed boundary conditions are depicted in Figure 6.2. Fully structured grids were created and the high grid density was maintained at the nozzle throat, injection port, and nozzle exit because of the critical importance of computational grids at these locations. Furthermore, in order to calculate viscous flows, boundary layer grids were

created close to the nozzle surface, considering the impact of the boundary layers that formed along the nozzle surfaces.

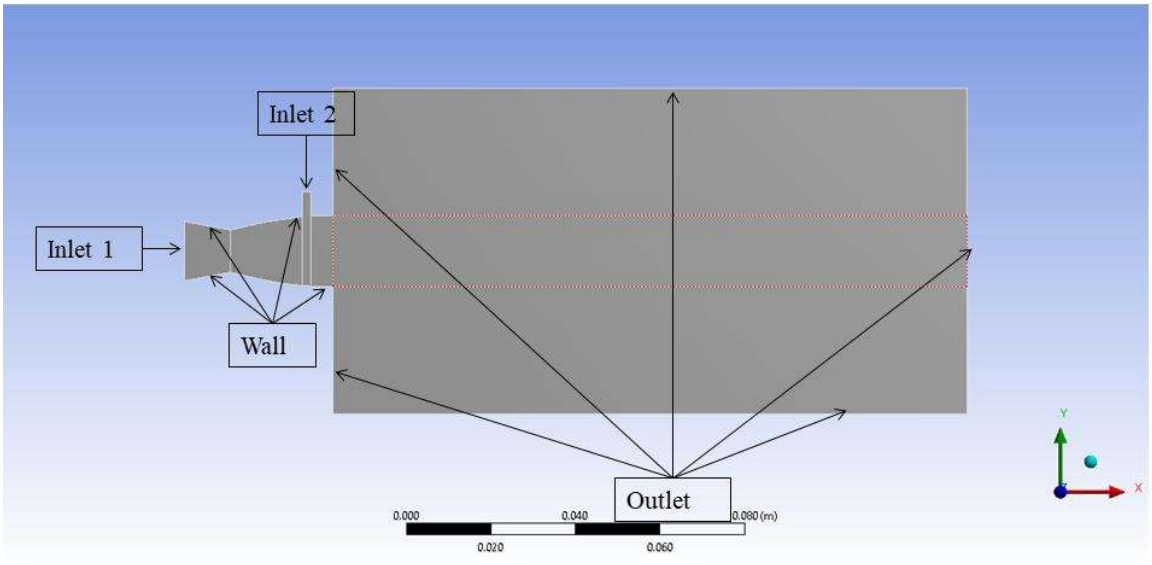


Figure 6.2: Computational domain with boundary conditions

ANSYS Fluent v 19.2 was used as a solver for the current simulation. Following setup was taken for the numerical simulation:

Table 6.1: Fluid domain setup for thrust vectoring

| | | |
|---|---|---|
| General | Type | Density based |
| | Time | Steady |
| | Velocity Formulation | Absolute |
| | 2D – space | Planar |
| Models | Energy | On |
| | Viscous model | k – ω |
| | Density | Ideal gas |
| | Viscosity | Sutherland (Three coefficient method) |
| Boundary Conditions | Inlet | Type: Pressure inlet |
| | | Gauge total pressure : 400000 – 1000000 Pa |

| | | |
|---|---|---|
| | | Total temperature: 300 K |
| | Outlet | Type: Pressure outlet |
| | | Gauge pressure: 0 Pa |
| | Wall | Stationary wall |
| | | No slip condition |
| Solution Controls | Courant number | Up to 1 |

### 6.1.3 Validation of Numerical Methodology

In order to validate the numerical methodology used in this research, the experiment carried out by Waithe and Deere at NASA Langley Research Center was replicated and the results from the numerical simulation was compared with the experimental data. The nozzle geometry used by (Waithe & Deere, n.d.) is shown in the Figure 6.3.

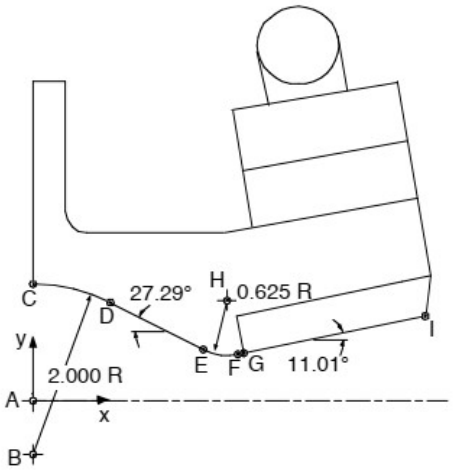


| POINT | COORDINATES (IN.) | |
|---|---|---|
| | x | y |
| A | 0.000 | 0.000 |
| B | 0.000 | -0.614 |
| C | 0.000 | 1.386 |
| D | 0.917 | 1.163 |
| E | 1.988 | 0.611 |
| F | 2.394 | 0.553 |
| G | 2.430 | 0.559 |
| H | 2.275 | 1.166 |
| I | 4.550 | 0.972 |

Figure 6.3: Nozzle geometry used in experimental study in NASA Langley Research Center

The experimental study was conducted at static conditions in the Jet Exit Test Facility of the 16-Foot Transonic Tunnel Complex at NASA Langley Research Center. Models were mounted to the dual-flow propulsion simulation system on a test stand located in the test bay of the facility (Waithe & Deere, K.A.). The studies were carried out for NPR = 4.6 and SPR = 0.7 and quantitatively, the thrust vector angle was found to be $7^0$. The numerical simulation was carried out for the same geometry and input parameters using

ANSYS fluent 19 v2 and the deflection angle was found to be equal to $7.5^0$, which is very close to $7^0$. This concludes that the numerical simulations carried out in this study are valid. The *Figure 6.4* compares the experimental and computational results.

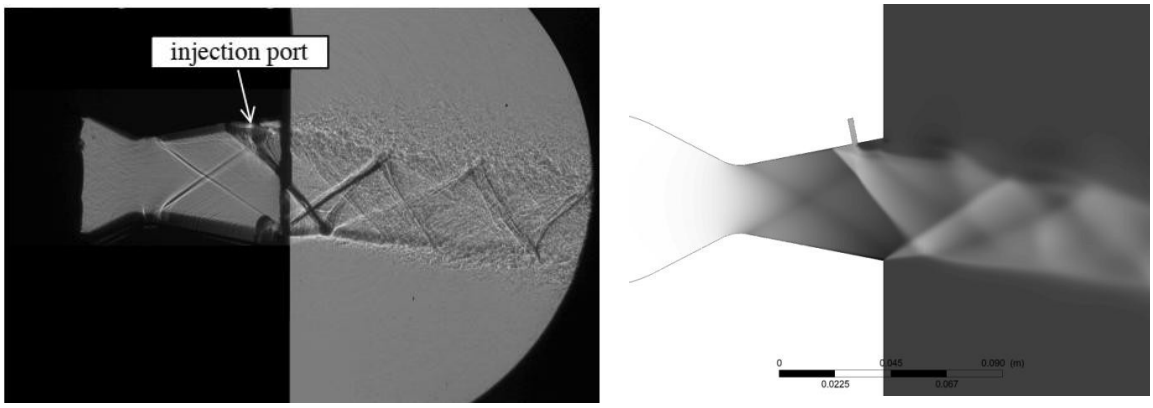


(a) (b)

Figure 6.4: Comparison between experimental shadowgraphy and density contour (NPR = 4.6 and SPR = 0.7): (a) experimental shadography, (b) density contour obtained from computational analysis

### 6.1.4 Mesh Independence Test

In order to ascertain the mesh independence and obtain the least number of nodes that yields accurate results, the number of elements was varied and average Mach number at throat observed. It was found that on decreasing the number of elements from 35812 to 28970, the discrepancy in Mach number was below 0.3 % and on further decreasing the element numbers the discrepancy was above 0.3%. Thus, 28970 was the number of elements selected. The variation of Mach number with the number of elements is shown in the Figure 6.5.

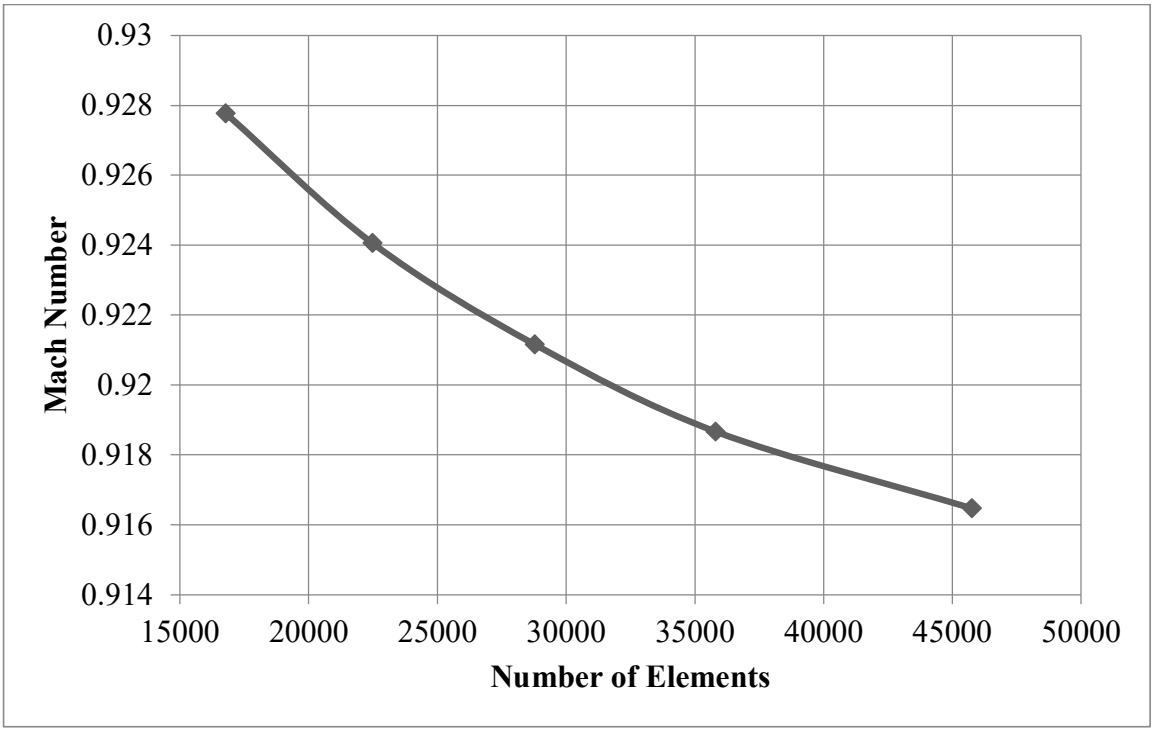


Figure 6.5: Variation of Mach number at throat with number of elements

### 6.1.5 Results and Discussions

#### 6.1.5.1 Effect of NPR

Four different NPRs were taken for the study; 5, 7, 9 and 11. Among the four different pressure ratios, two (5 and 7) resulted in over - expanded jet, while the remaining two (9 and 11) resulted in under - expanded jet as the design pressure ratio was 7.824. Increasing the NPR had an inverse effect on the deflection angle. The deflection angle decreased with the increase in NPR for the given secondary inlet location as well as for the given SPR. The variation of deflection angle with NPR for the given secondary inlet locations is represented in the Figure 6.6.

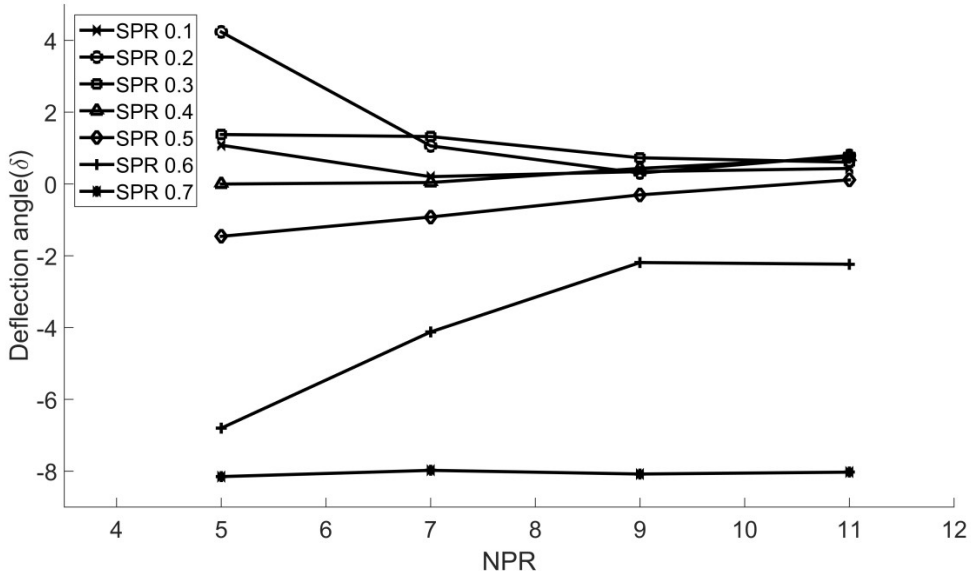
SPR 0.1
SPR 0.2
SPR 0.3
SPR 0.4
SPR 0.5
SPR 0.6
SPR 0.7
Deflection angle(δ)
NPR
4
2
0
-2
-4
-6
-8
4
5
6
7
8
9
10
11
12

(a)

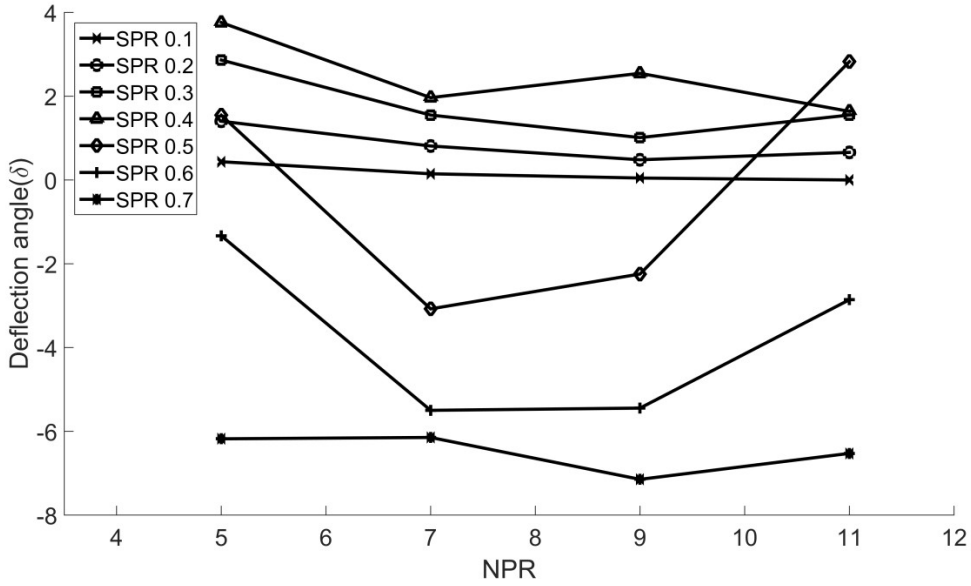
SPR 0.1
SPR 0.2
SPR 0.3
SPR 0.4
SPR 0.5
SPR 0.6
SPR 0.7
Deflection angle(δ)
NPR
4
2
0
-2
-4
-6
-8
4
5
6
7
8
9
10
11
12

(b)

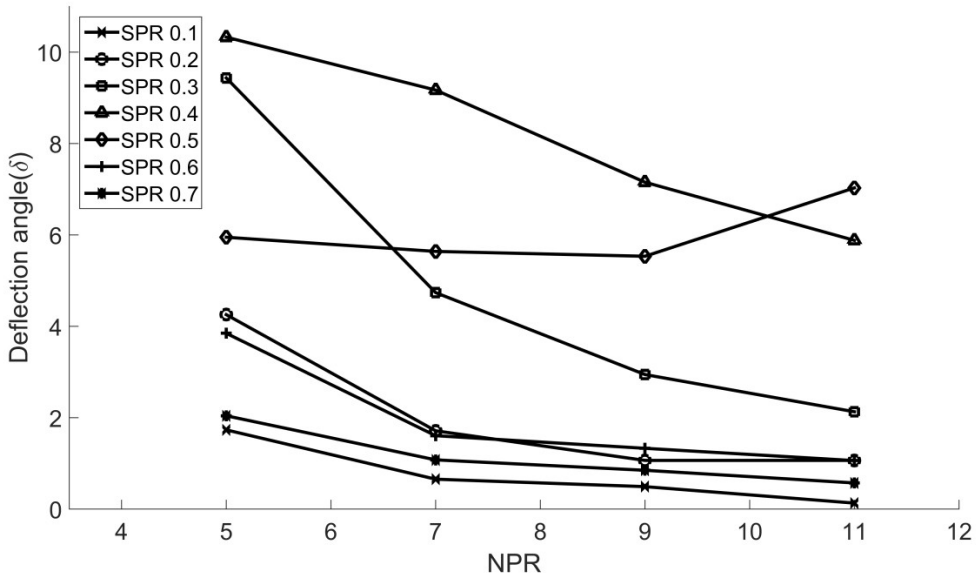


(c)

Figure 6.6: Variation of deflection angle with NPR for secondary inlet located at (a) 25 % , (b) 50 % and (c) 75 % of divergent section length

It was found from the numerical simulations that when the secondary inlets were located at 25 % and 50 % of the divergent section length, the jets deflected in direction opposite to that anticipated when the SPR was increased above 0.4. For these two secondary inlet locations, the deflection angle decreased with increase in NPR. It was found that the deflection angle was maximum for the NPR of 5 for all SPRs and secondary inlet locations, even for jet deflected in opposite direction (SPR 0.5 and more). Similarly, the minimum deflection of jet was found to occur for NPR of 11 for majority of the cases. Although the deflection was in opposite direction, for secondary inlet located mid – way of divergent section length, jet deflection increased with NPR, reached maximum around NPR of 7 and 9 and decreased for SPRs corresponding to 0.5 and 0.6. For both secondary inlet locations mentioned above, there was no significant change in deflection angle with the change in NPR for SPR corresponding to 0.7. For secondary inlet located at ¾ th length of divergent section, the deflection angle almost invariably decreased with increase in NPR except for SPR of 0.5 wherein the deflection angle increased with increase in NPR.

Looking at the graphical results from the simulation it was found that at lower NPR, the shock wave was found to form way upstream of the secondary inlet with a large boundary layer separation region upstream and downstream of the secondary inlet causing a large deflection in jet. With the further increase in the NPR, the shock wave became closer to the secondary inlet and thus reducing the flow separation region. This phenomenon is clearly depicted by the Figure 6.7 wherein, the secondary inlet is located at 75 % of the divergent section length and the SPR is 0.4 for both the cases and the NPRs are 5 and 9 respectively.

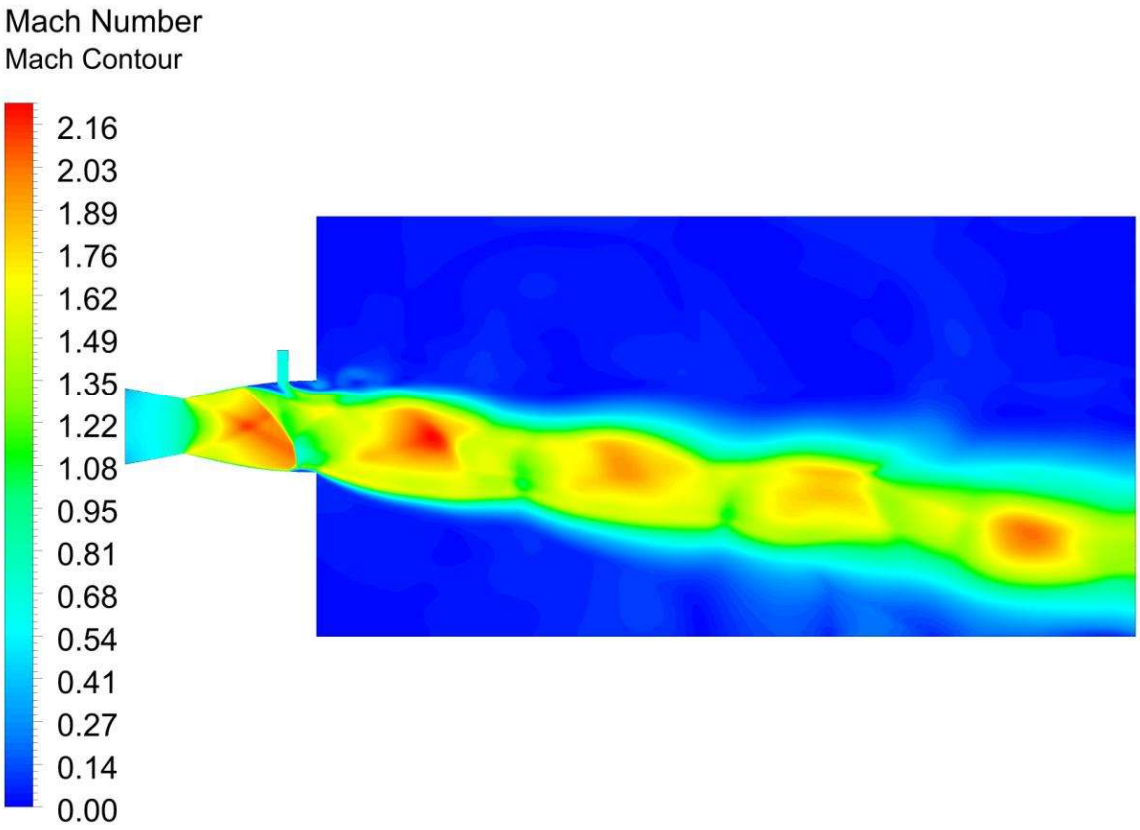


(a)

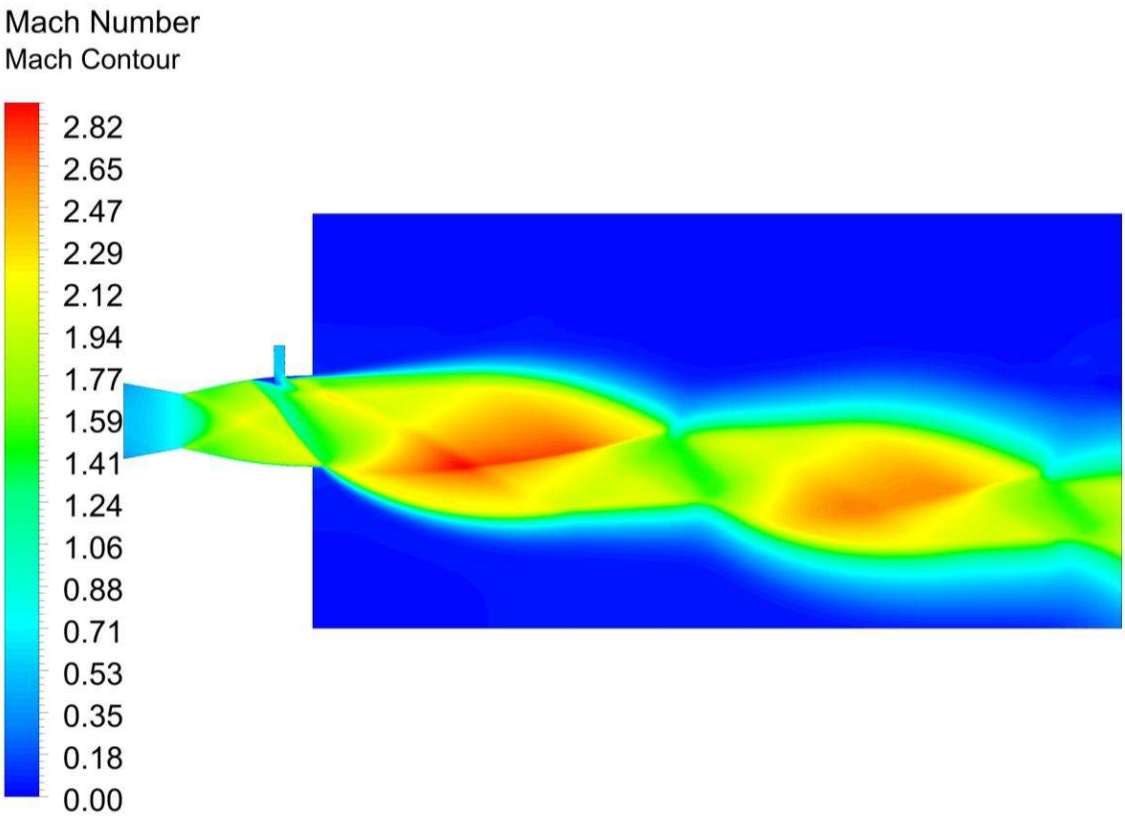


(b)

Figure 6.7: Mach contours for SPR = 0. 4 when (a) NPR = 5 and (b) NPR = 9

#### 6.1.5.2 Effect of SPR

Secondary pressure ratio refers to the ratio of total gauge pressure at secondary inlet to the total nozzle pressure at main inlet. Seven different SPRs (0.1 to 0.7 with 0.1 increments) were taken for the study. The variation of jet deflection with SPRs was studied. Figure 6.8 shows the variation of deflection angle with SPRs at different secondary inlet locations.

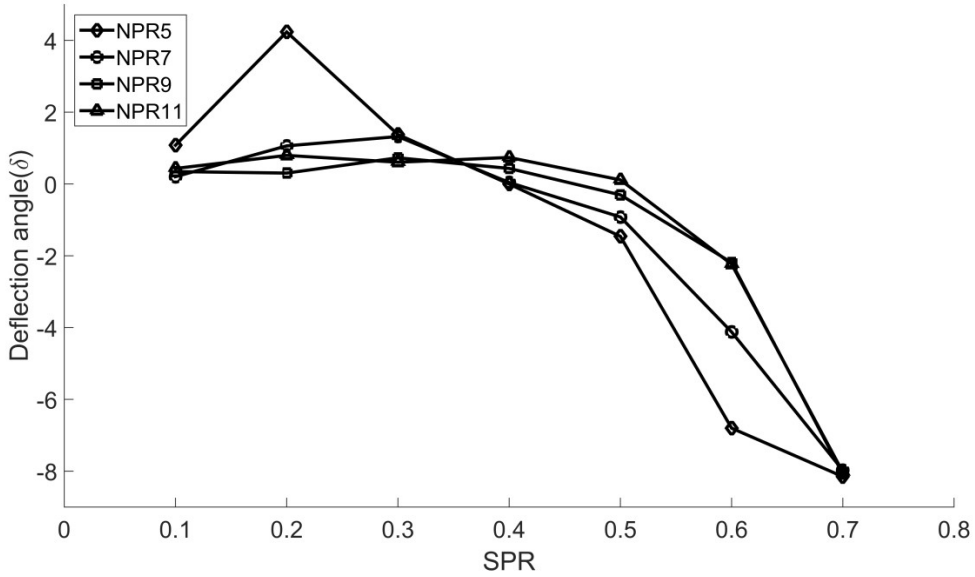
NPR5
NPR7
NPR9
NPR11
Deflection angle(δ)
SPR
4
2
0
-2
-4
-6
-8
0
0.1
0.2
0.3
0.4
0.5
0.6
0.7
0.8

(a)

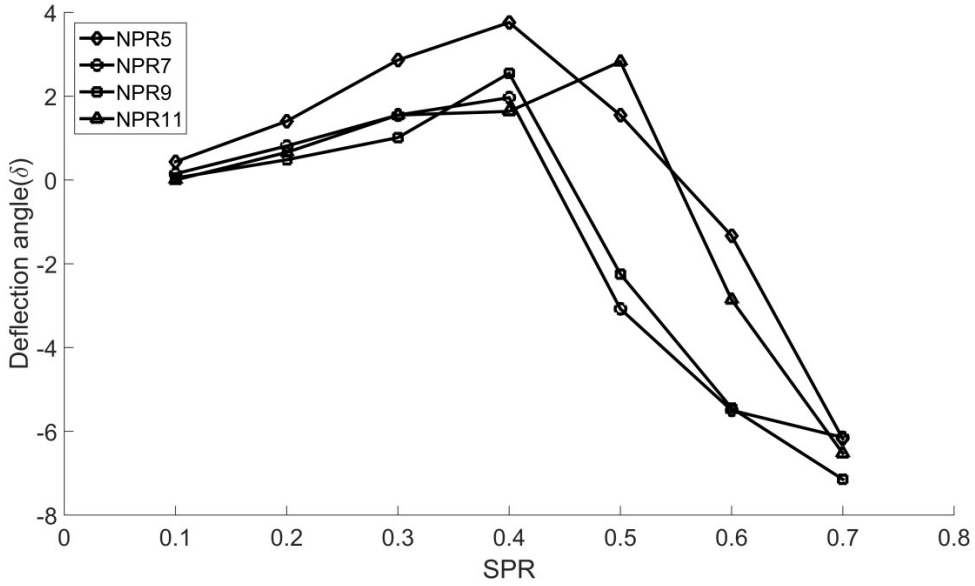
NPR5
NPR7
NPR9
NPR11
Deflection angle(δ)
SPR
4
2
0
-2
-4
-6
-8
0
0.1
0.2
0.3
0.4
0.5
0.6
0.7
0.8

(b)

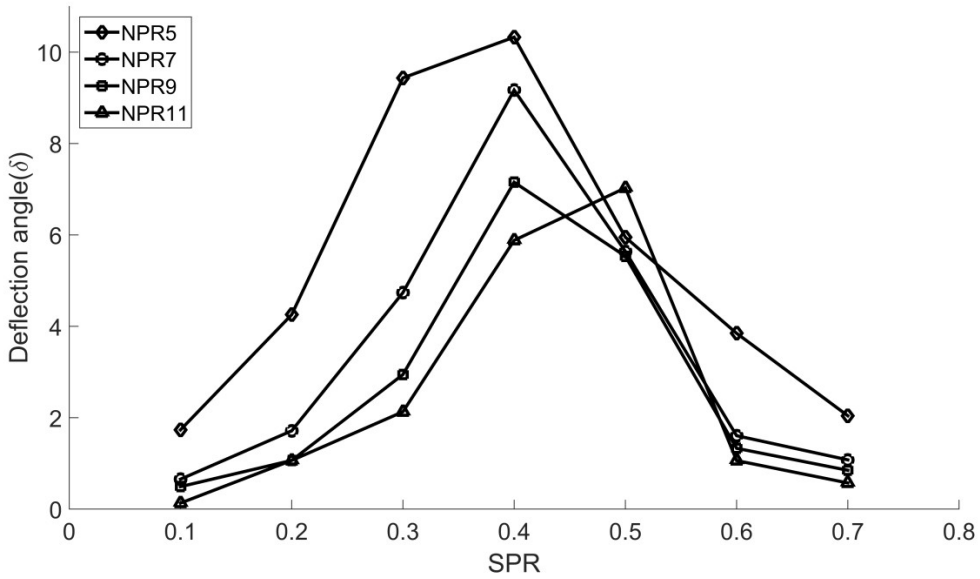


(c)

Figure 6.8: Variation of deflection angle with SPR for the given NPRs when the secondary inlets are locations at (a) 25 %; (b) 50%; (c)75 % of divergent section length

For secondary inlets located at 25 % of the divergent section length, the deflection angle peaked at around the SPR of 0.2 and 0.3 for all the NPRs. Beyond this SPR, the deflection angle decreased and the jet started deflecting in opposite direction and the angle of deflection in opposite direction increased with increase in SPR, reaching maximum deflection in opposite direction at SPR corresponding to 0.8. The same phenomenon was seen for secondary inlet located at mid – length of the divergent with the only difference of positive deflection angle peaking at rather larger SPR (0.4 for NPRs corresponding to 5, 7 and 9 and 0.5 for NPR 11). The jet being deflected in rather opposite direction at these two secondary inlet locations can be attributed to complex interaction of shock wave, boundary layer and reflection wave on the nozzle wall opposite to the secondary inlet, which deflected the jet in the opposite direction. This Mach contour at NPR 5 and SPR 0.6 when the secondary inlet is located at 25% of the divergent section from throat is shown in the Figure 6.9.

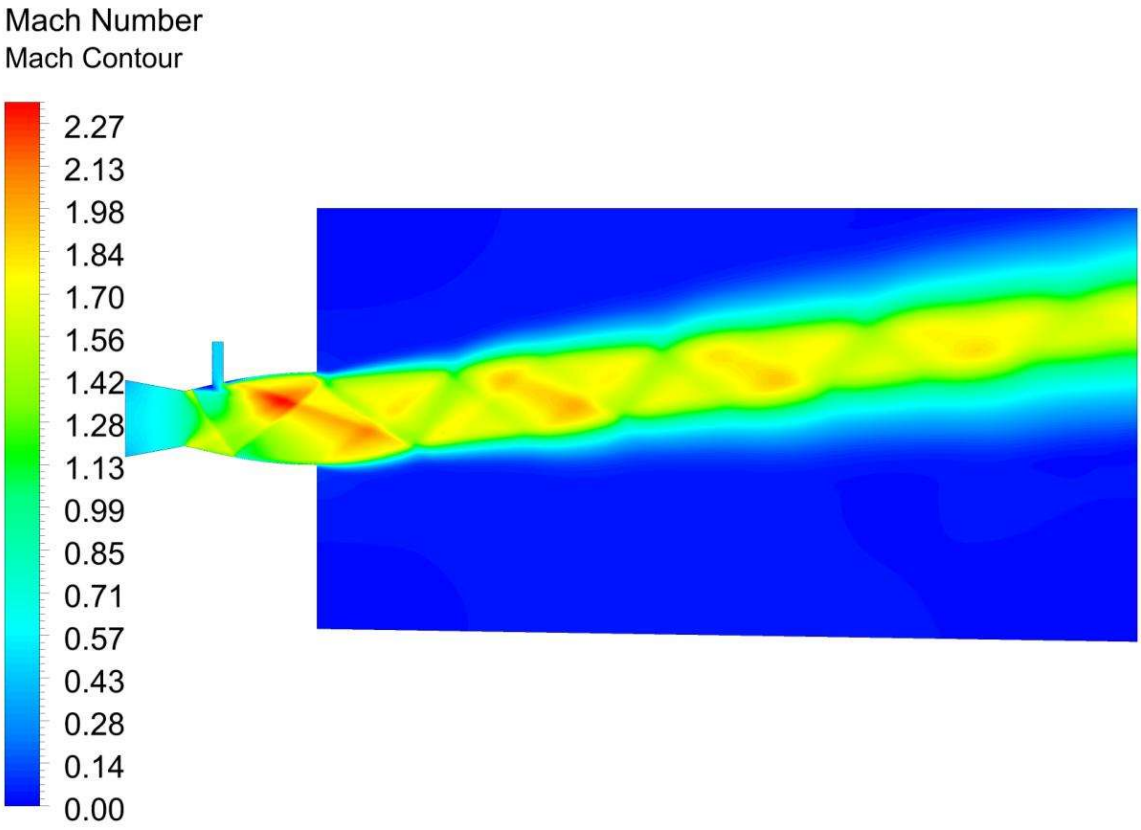


Figure 6.9 : Mach contour for secondary inlet located at 25 % of diverging section length, NPR = 5; SPR =0.6

From the *Figure 6.8*, it can be also be seen that for the secondary inlet located at 75 % of divergent section length, increasing the SPR increased the deflection angle but only up to SPR = 0.4 for all NPRs except for NPR of 11. For NPR corresponding to 11, the maximum deflection occurred at SPR of 0.5. Beyond this value, increasing the SPR had contour – intuitive effect and the deflection angle decreased beyond this limit. The same phenomenon described above can be attributed for this behavior of the jet.

The variation of jet deflection with respect to SPR is demonstrated by the Mach contours in the Figure 6.10. The contours were obtained at different SPRs when the secondary inlet was located at 75 % of divergent section length and NPR was taken to be 5.

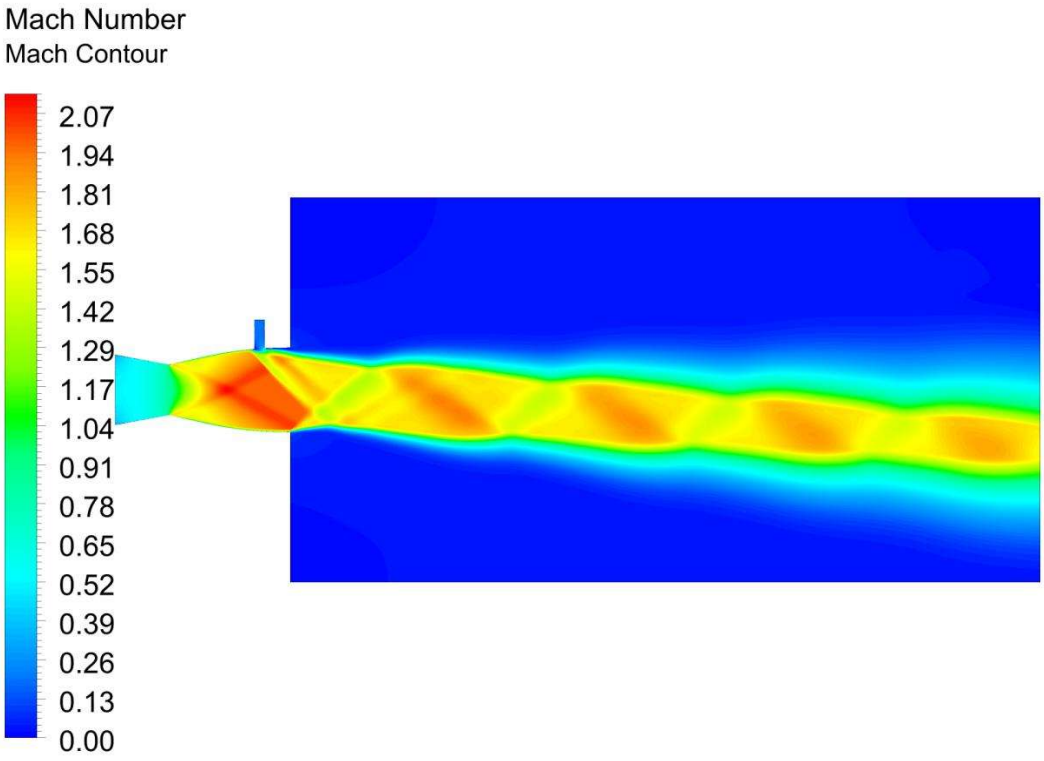
Mach Number
Mach Contour
2.07
1.94
1.81
1.68
1.55
1.42
1.29
1.17
1.04
0.91
0.78
0.65
0.52
0.39
0.26
0.13
0.00

(a)

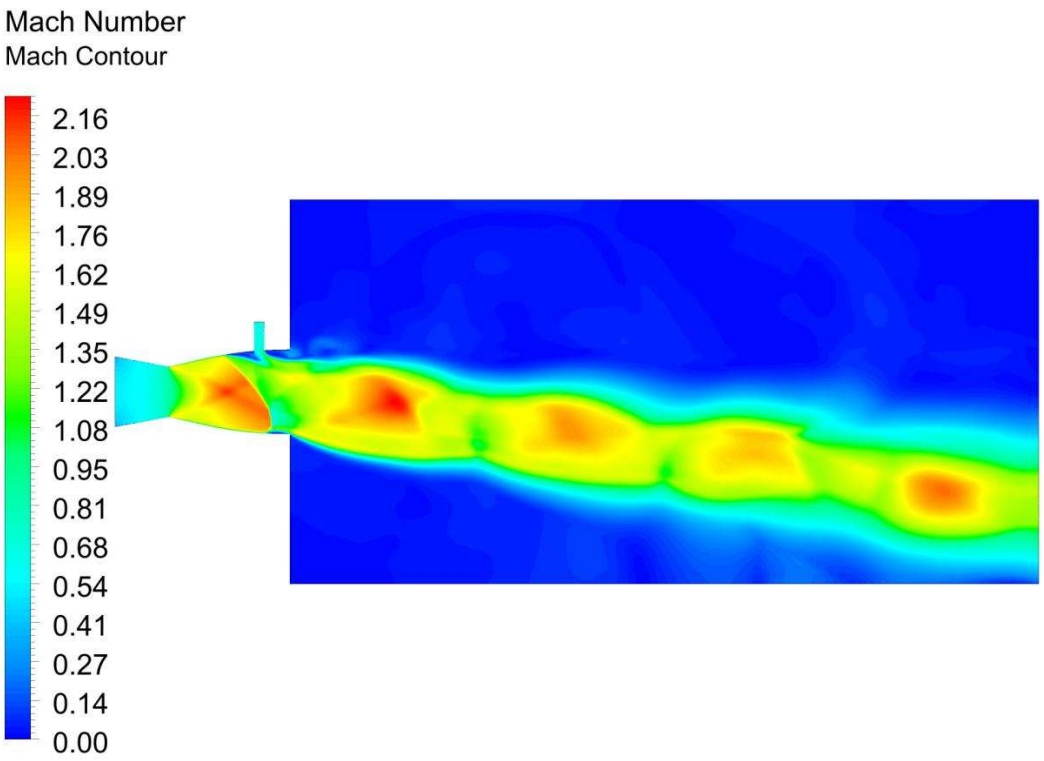
Mach Number
Mach Contour
2.16
2.03
1.89
1.76
1.62
1.49
1.35
1.22
1.08
0.95
0.81
0.68
0.54
0.41
0.27
0.14
0.00

(b)

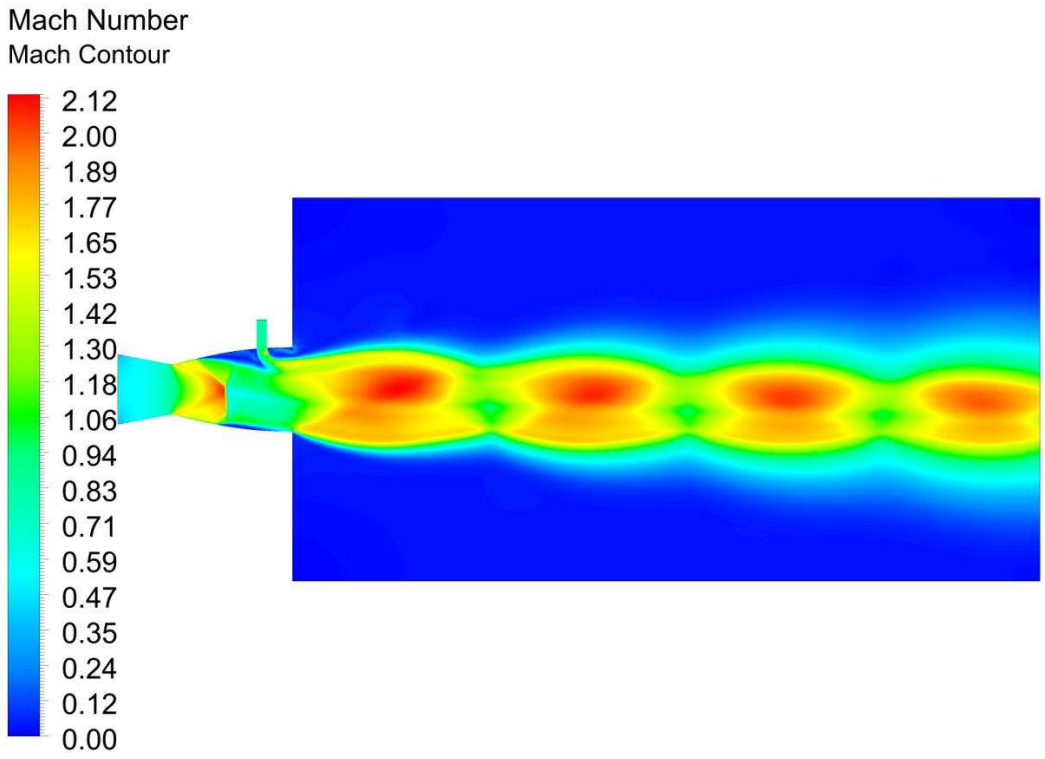


(c)

Figure 6.10: Mach contours for secondary inlet location 75 % of divergent section, NPR = 5 and (a) SPR = 0.2, (b) SPR = 0.4 and (c) SPR = 0.7

#### 6.1.5.3 Effect of Secondary Inlet Locations

Three different secondary inlet locations; at 25 %, 50 %, and 75 % of the divergent section length, were taken for the current study. The width of the secondary inlet was kept constant at 2 mm. The variation of jet deflection with secondary inlet locations is summarized in Figure 6.11 and Figure 6.12.

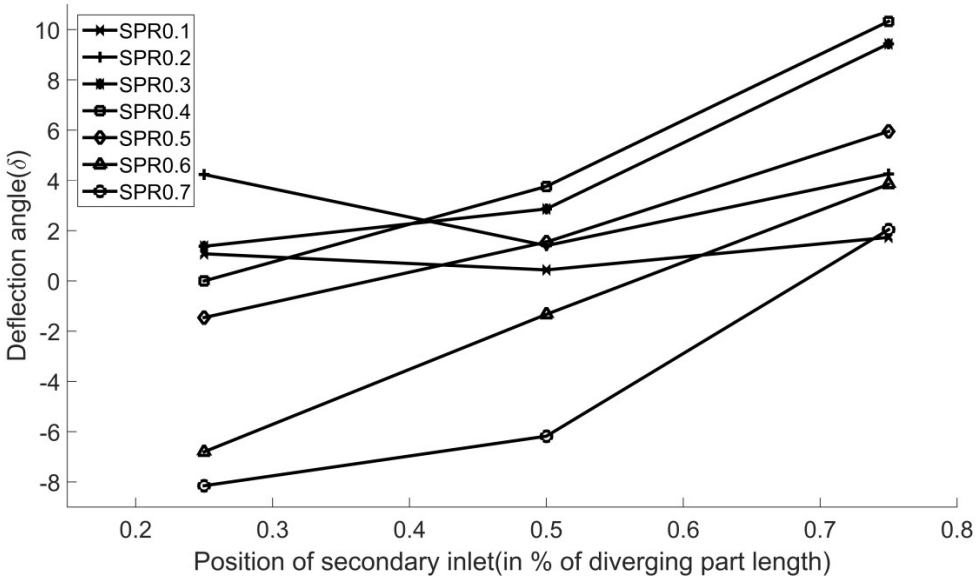
SPR0.1
SPR0.2
SPR0.3
SPR0.4
SPR0.5
SPR0.6
SPR0.7
Deflection angle(δ)
Position of secondary inlet(in % of diverging part length)

(a)

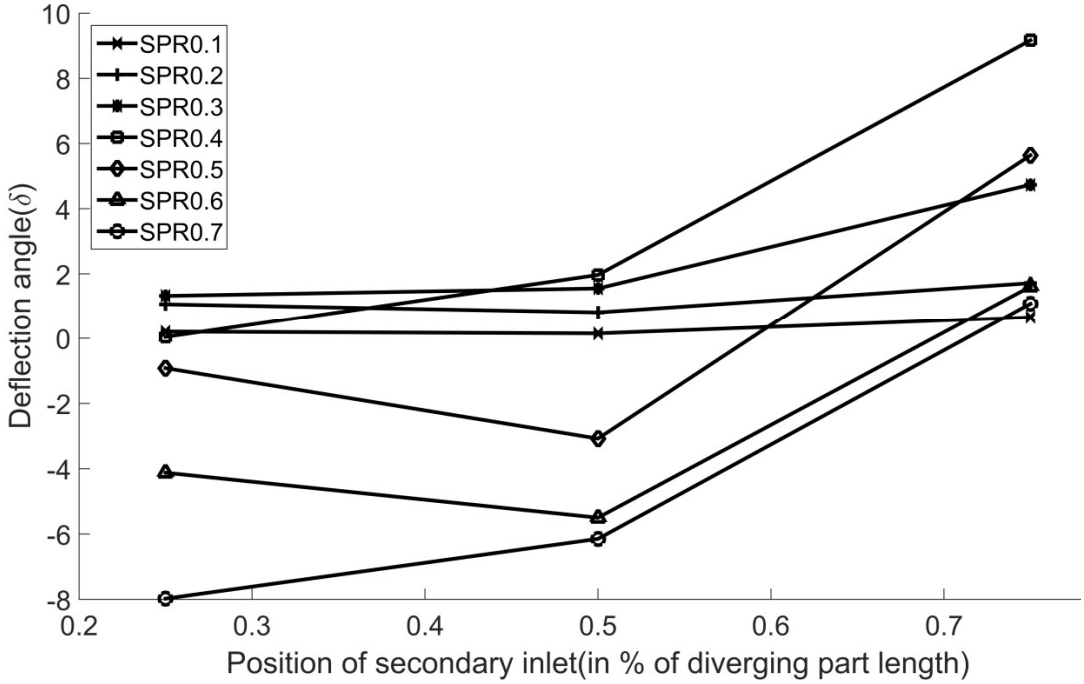
SPR0.1
SPR0.2
SPR0.3
SPR0.4
SPR0.5
SPR0.6
SPR0.7
Deflection angle(δ)
Position of secondary inlet(in % of diverging part length)

(b)

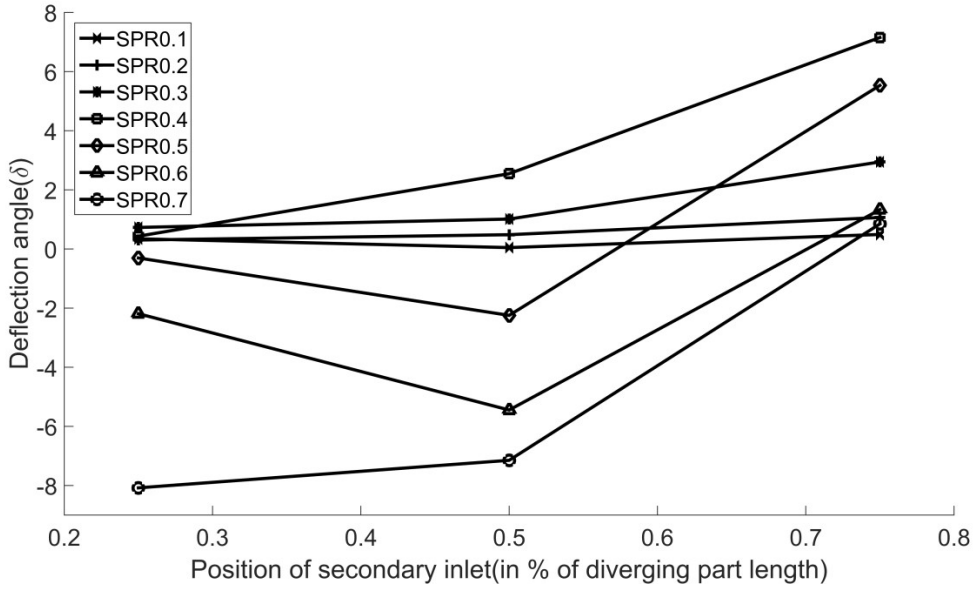


(c)

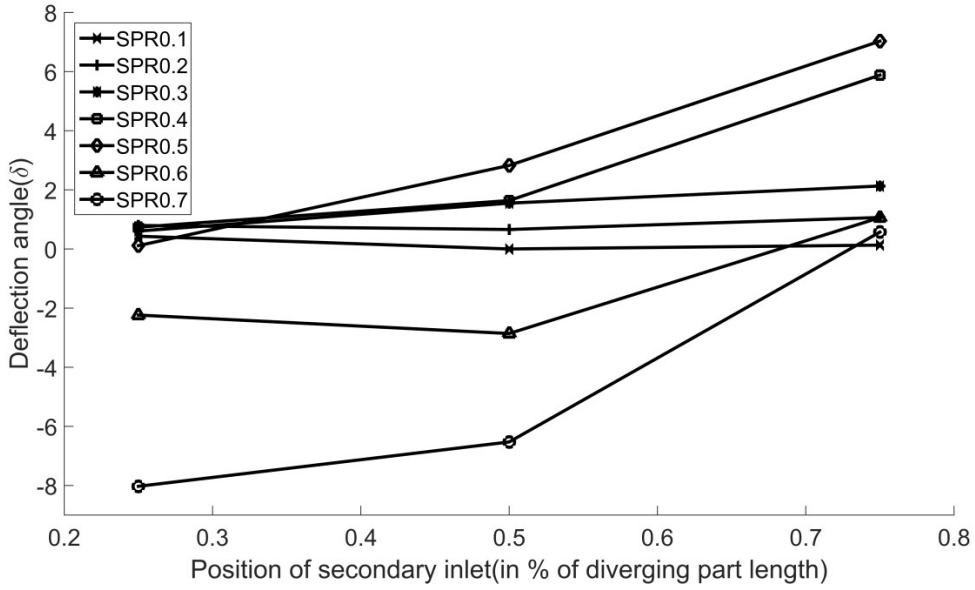


(d)

Figure 6.11 : Variation of deflection angle with secondary inlet locations at given SPRs (a) NPR = 5; (b) NPR = 7; (c) NPR = 9 and (d) NPR = 11

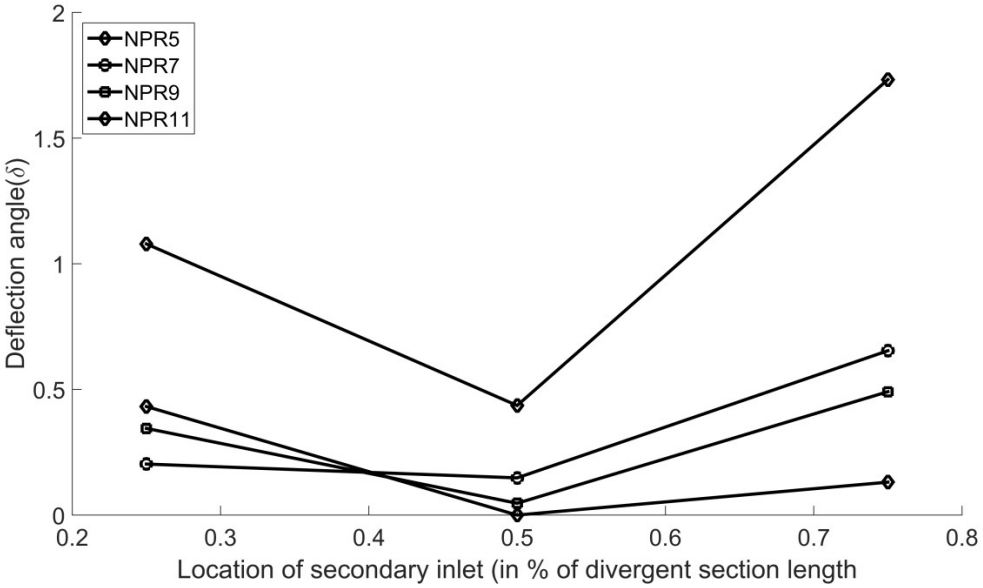
NPR5
NPR7
NPR9
NPR11
Deflection angle(δ)
Location of secondary inlet (in % of divergent section length
0
0.5
1
1.5
2
0.2
0.3
0.4
0.5
0.6
0.7
0.8

(a)

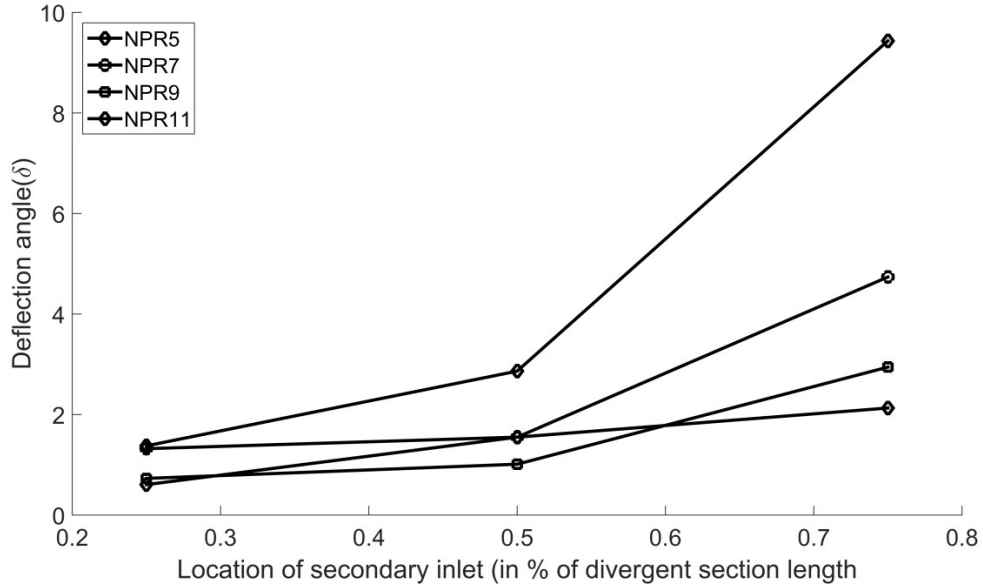
NPR5
NPR7
NPR9
NPR11
Deflection angle(δ)
Location of secondary inlet (in % of divergent section length
0
2
4
6
8
10
0.2
0.3
0.4
0.5
0.6
0.7
0.8

(b)

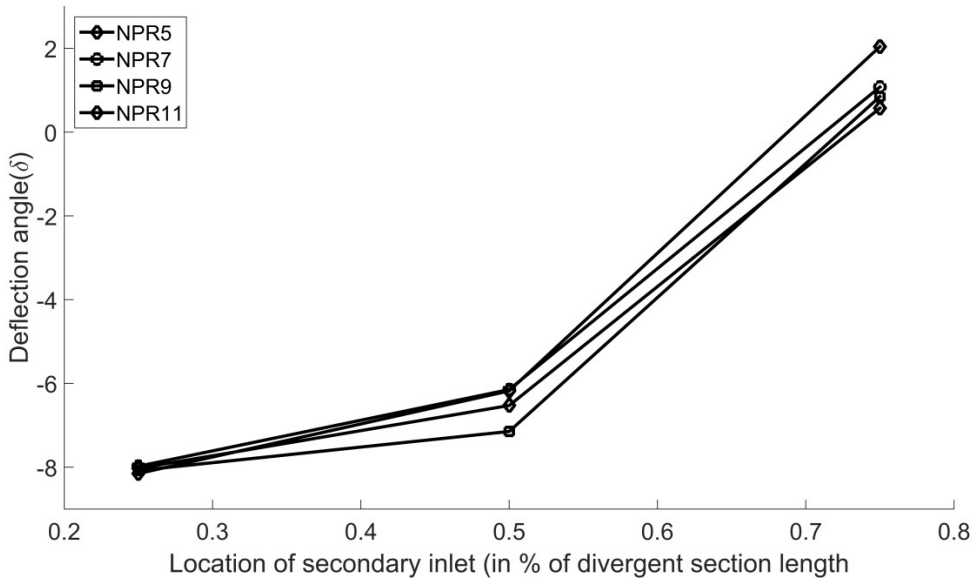


(c)

Figure 6.12 : Variation of deflection angle with secondary inlet locations at given NPRs (a) SPR = 0.1 ; (b) SPR = 0.3; (c) SPR = 0.7

The jet deflection angle was seen to increase as the secondary inlet location shifted away from the nozzle throat. For the given NPR and SPR, the deflection angle was minimum at the secondary inlet location located near to the throat for almost all the cases with some exception. The exceptions being when the NPR equaled 5 (and SPR = 0.2) and when the NPR equaled 11 (and SPR = 0.1). The maximum deflection angles were obtained when the secondary inlet was located at 75 % of the nozzle divergent section except for the same exceptions discussed above. This phenomenon was observed because for the secondary inlets located near the throat, the oblique shock wave produced by the secondary inlet was reflected by the opposite wall of the nozzle. This reflected wave turned the jet towards the center line of the nozzle reducing and even sometimes superseding the jet deflection achieved by the shock wave upstream. The phenomenon of change in deflection angle with secondary inlet location is demonstrated by Mach contours in Figure 6.13. The Mach contours were obtained for NPR of 5 and SPR of 0.4 for different secondary inlet locations.

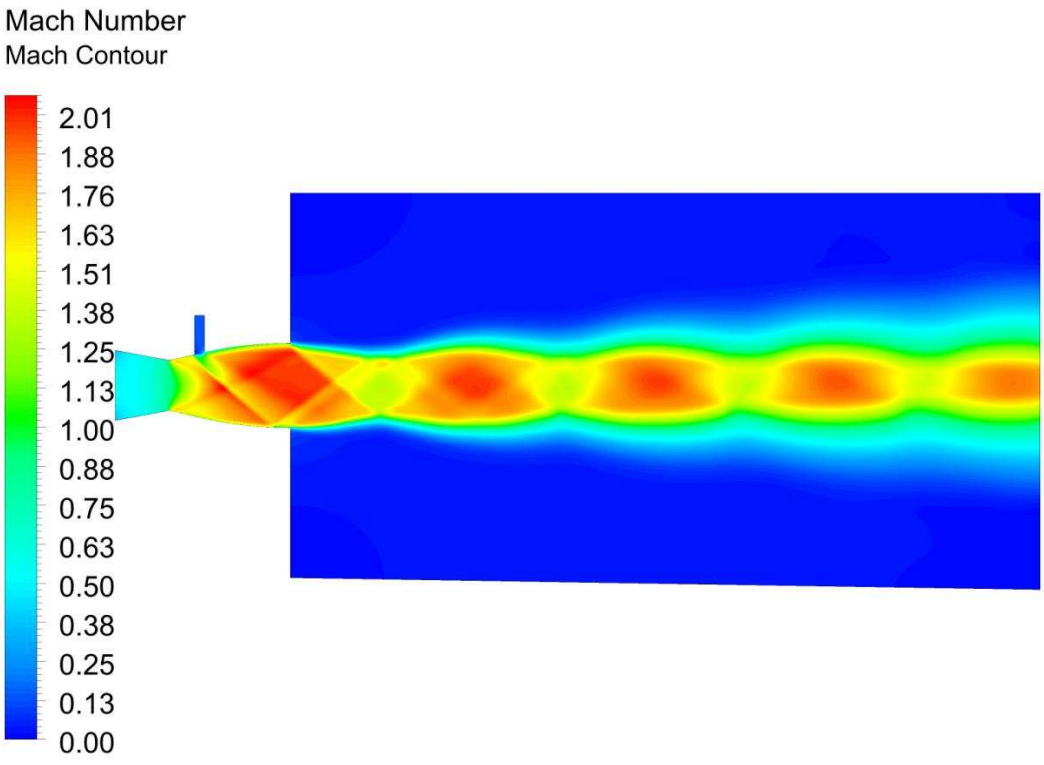
Mach Number
Mach Contour
2.01
1.88
1.76
1.63
1.51
1.38
1.25
1.13
1.00
0.88
0.75
0.63
0.50
0.38
0.25
0.13
0.00

(a)

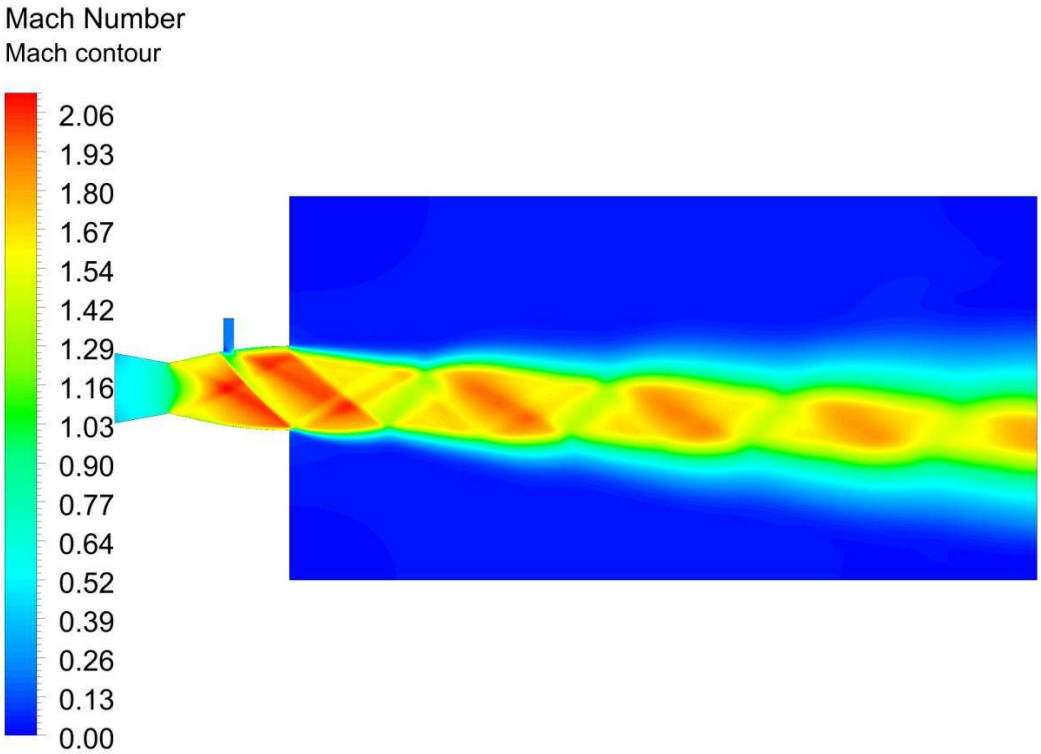
Mach Number
Mach contour
2.06
1.93
1.80
1.67
1.54
1.42
1.29
1.16
1.03
0.90
0.77
0.64
0.52
0.39
0.26
0.13
0.00

(b)

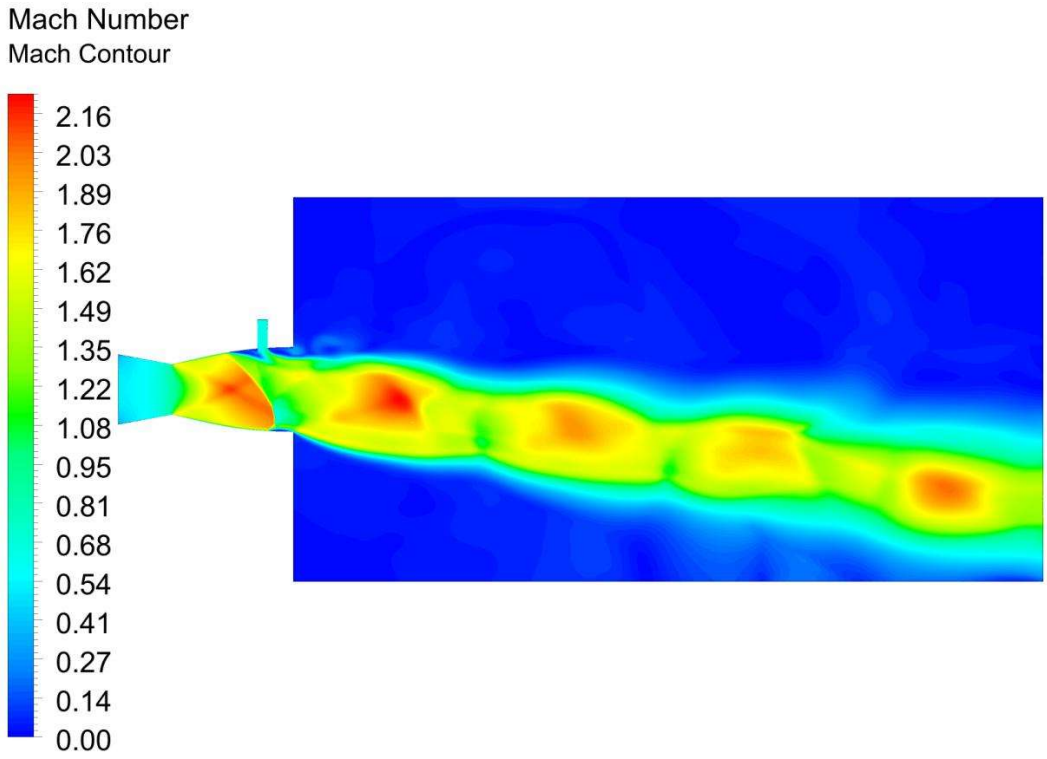


(c)

Figure 6.13: Mach contour when NPR = 5 and SPR = 0.4 for secondary inlet located at (a) 25 %, (b) 50 % and (c) 75 % of the divergent section length

#### 6.1.5.4 Effect of Secondary Inlet Angles

Computational studies were carried out to study the effect of secondary inlet angles for limited number of cases; NPR corresponding to 5 and 11 and SPRs corresponding to 0.2, 0.4 and 0.7 for each NPR. The secondary inlet angles taken for study were 45, 60, 75 and 90 degrees. The variation of deflection angles with secondary inlet angles is summarized in the Figure 6.14. It can be seen that for higher SPR of 0.7, the deflection angle decreased with the increase in secondary inlet angle for both the NPRs. At lower SPR of 0.2, no significant change in deflection angle was observed for both NPRs. Similarly, for the SPR of 0.4, the deflection angle was seen to increase with increase in secondary inlet angle for NPR of 5 and decrease for the NPR of 11.

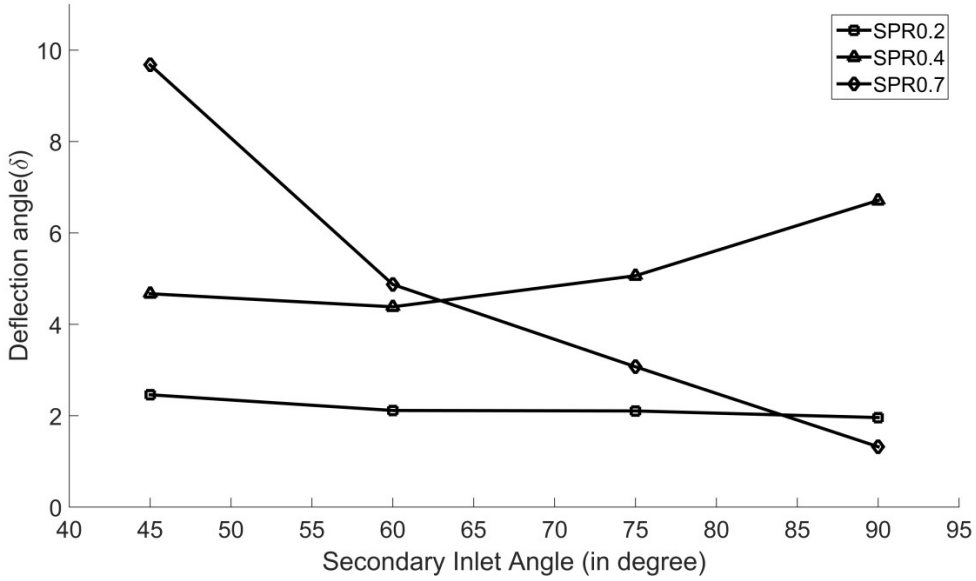


(a)

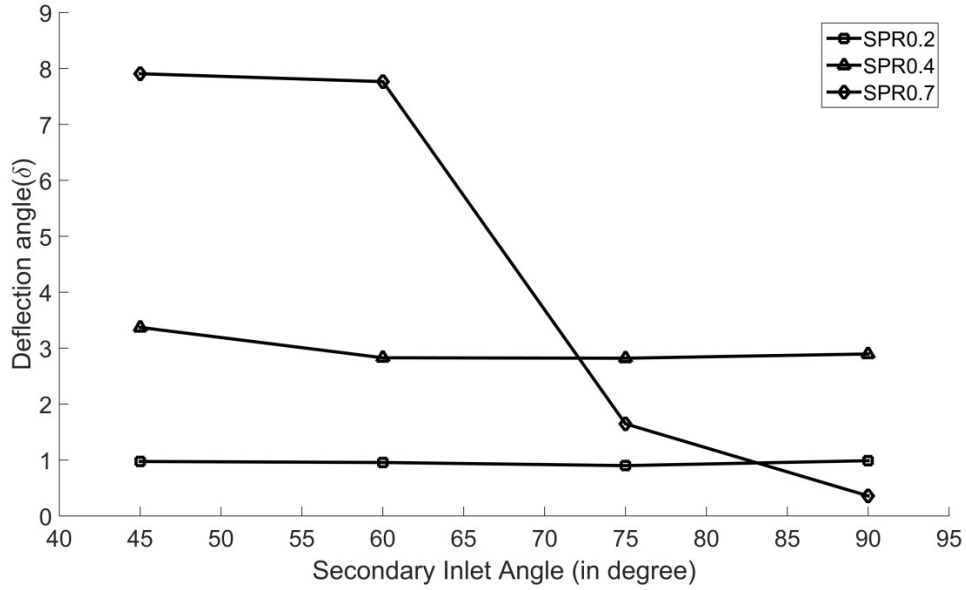


(b)

Figure 6.14: Variation of deflection angle with secondary inlet angle for the given SPRs and the secondary inlet located at 75 % of the divergent section length (a) NPR = 5 and (b) NPR = 11

## 6.2 Experimental Analysis of Shock Vector Control

### 6.2.1 Modeling and Fabrication of Convergent Divergent Nozzle with Secondary Inlet

The CD nozzles with secondary inlet at three different locations were modeled in 3 – D modeling software Solidworks and printed using FDM method. The material used for printing all the nozzles was Polylactic Acid (PLA). The 3 - D model and the corresponding printed nozzles along with secondary inlet is shown in the Figure 6.15.

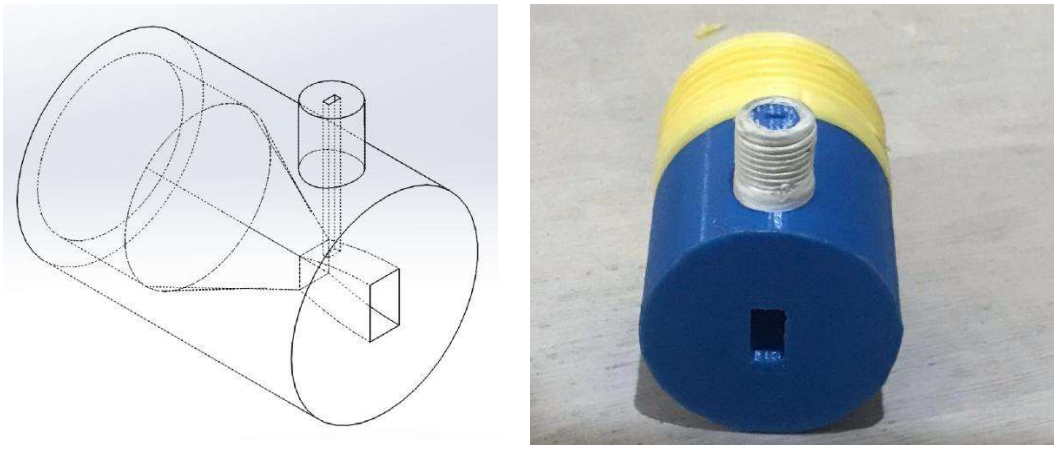

(a)

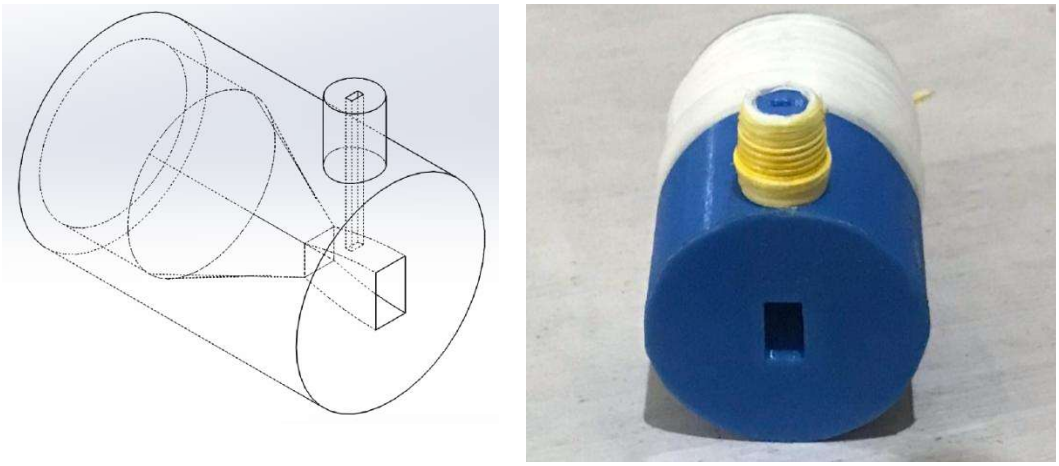

(b)

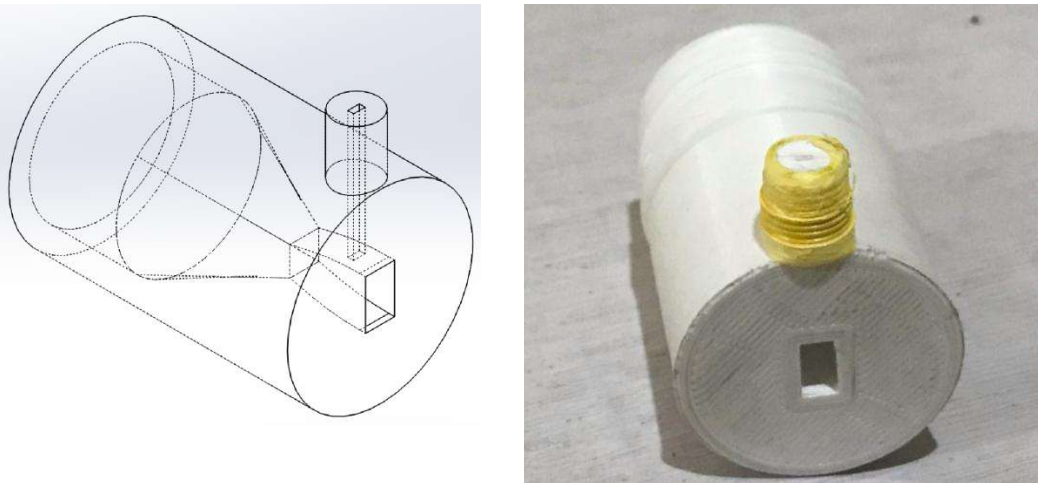

(c)

Figure 6.15: 3 D model and printed nozzles when the secondary inlet is locates at (a) 25 %, (b) 50 %, and (c) 75 % of the divergent section length

For the sake of visualizing the internal flow in the divergent section of the nozzle, the nozzles with transparent diverging section were also fabricated. Such nozzle is shown in the Figure 6.16.

Figure 6.16: 3 D printed nozzles with transparent divergent section with secondary inlet located at 25 %

### 6.2.2 Fabrication of Test Rig

The same test rig used for flow visualization of CD nozzle was used for the visualization of SVC. A secondary flow inlet was incorporated to the earlier setup. For the proper controlling of secondary inlet pressure, pressure reducing valve along with bulb valve were used. The test rig used for the experiment is shown in the *Figure 6.18*.

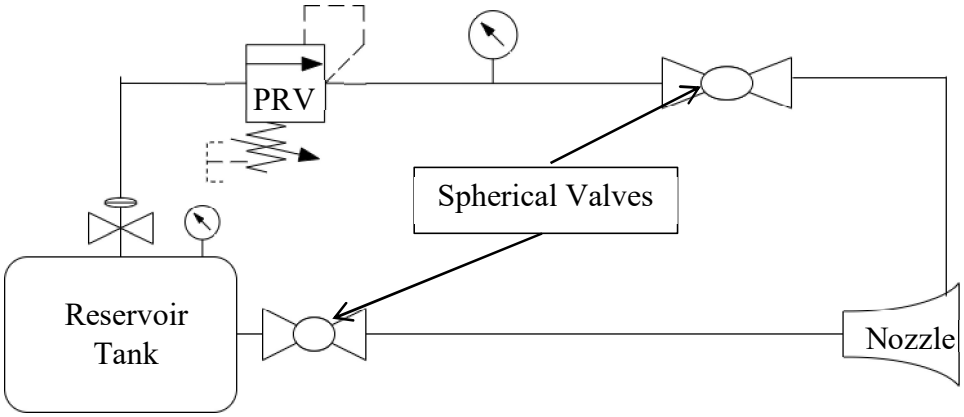


Figure 6.17: Schematic diagram of pneumatic components used in the test rig

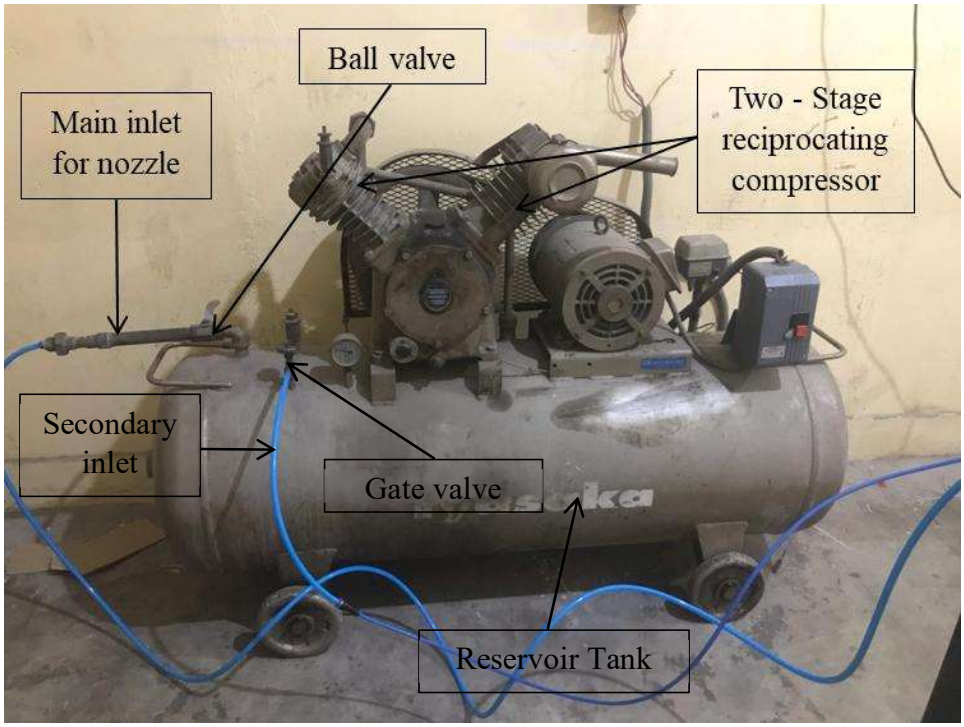


(a)

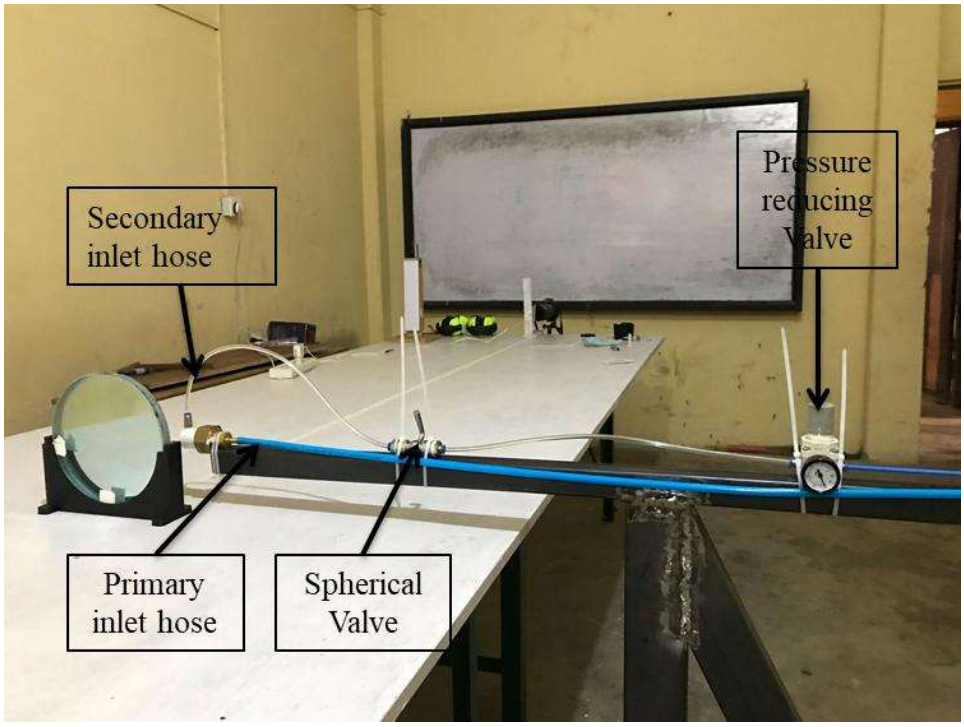


(b)

Figure 6.18: Test Rig for shock vector control analysis; (a) Compressor; (b) Pneumatic attachments with nozzle and mirror

### 6.2.3 Results and Discussions

The same parameters taken for numerical analysis were taken for experimental analysis of the shock vector control in CD nozzle. Nozzles with three different secondary inlet locations, located at 25 %, 50 % and 75 % of the divergent section length were taken. Similarly, three different NPRs, namely: 7, 9 and 11 were taken. Although, experiments at NPR of 5 were carried out, the images captured at that NPR could not be characterized properly and thus the deflection angle could not be measured accurately. Similarly, for all the secondary inlet locations and NPRs, 7 SPRs were taken; from 0.1 to 0.7 with 0.1 increment. These three parameters, namely: location of secondary inlet, NPR and SPR were varied and their effect on deflection angle was studied.

#### 6.2.3.1 Effects of NPRs

NPRs taken for experimental analysis were 7, 9, and 11. The effect of varying NPR for the given secondary inlet position and SPR is summarized in the Figure 6.19.

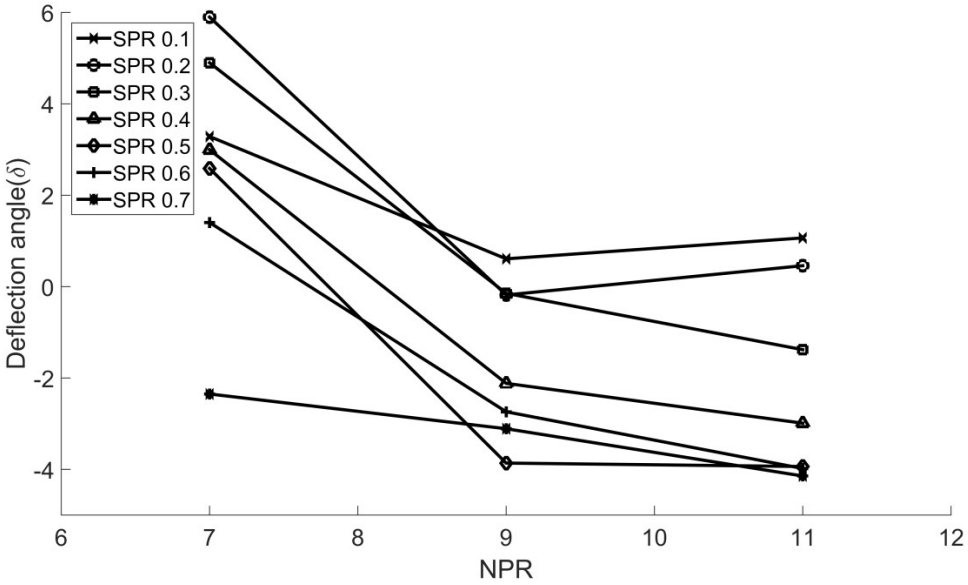
SPR 0.1
SPR 0.2
SPR 0.3
SPR 0.4
SPR 0.5
SPR 0.6
SPR 0.7
Deflection angle(δ)
NPR
6
4
2
0
-2
-4
6
7
8
9
10
11
12

(a)

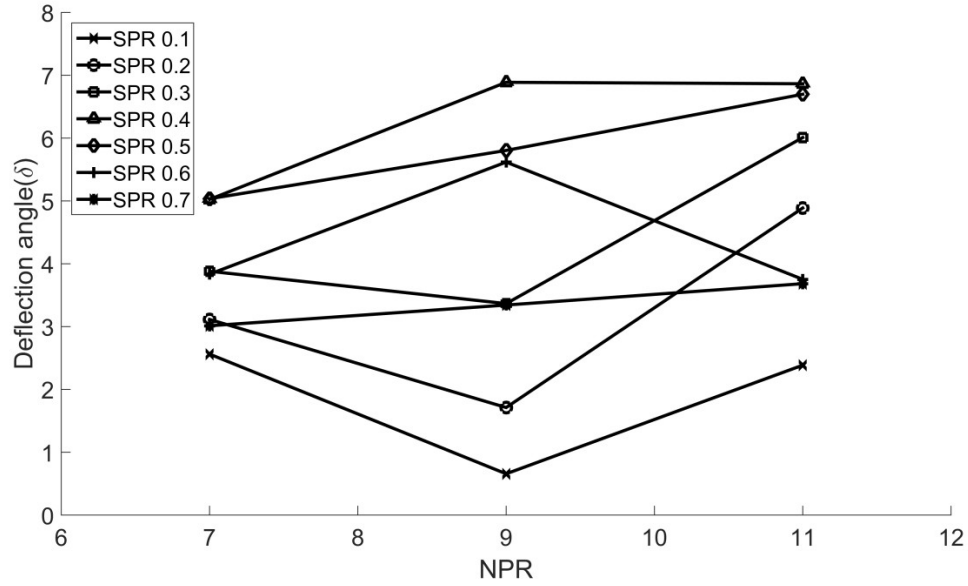
SPR 0.1
SPR 0.2
SPR 0.3
SPR 0.4
SPR 0.5
SPR 0.6
SPR 0.7
Deflection angle(δ)
NPR
8
7
6
5
4
3
2
1
0
6
7
8
9
10
11
12

(b)

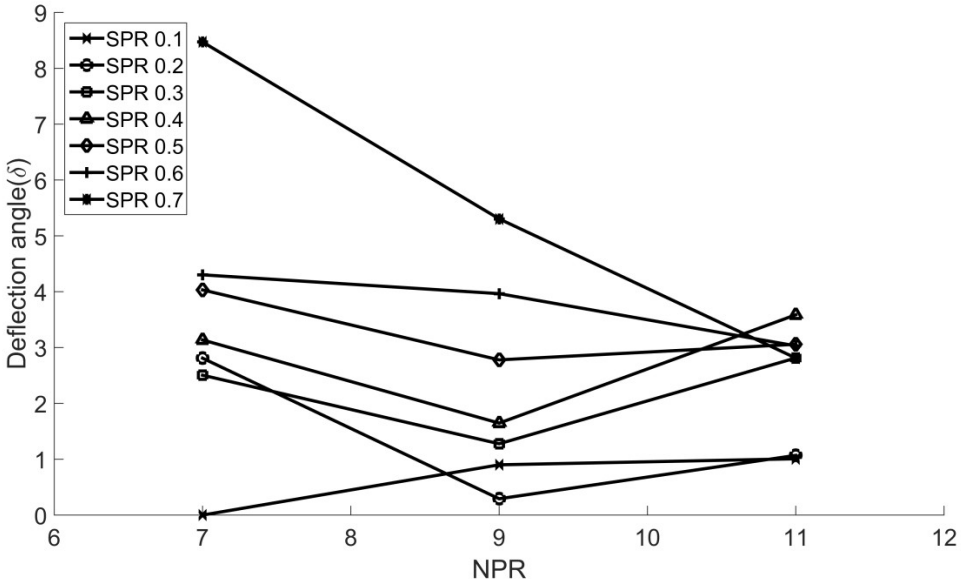


(c)

Figure 6.19: Variation of deflection angle with NPR for the given SPRs when the secondary inlet is located at (a) 25 % , (b) 50 %, and (c)75 % of the divergent section length

It was observed from experiments that when the secondary inlet was situated at ¼ th of the divergent section length, the deflection angle decreased and even deflected in opposite direction with the increase in NPR. At this location, for NPR equal to 7, the deflections were positive and maximum for all SPR except 0.7. On further increasing the NPR to 9, the deflection angle decreased but remained positive for SPR up to 0.3 and negative for the SPR above 0.3. At NPR corresponding to 11, jets corresponding to SPR up to 0.2 deflected in positive direction. For other secondary pressures, the jet deflected away in negative direction and the deflection angle even increased in the negative direction. Similarly, in case of secondary inlet located half way of the divergent section length, deflection angles were seen to decrease when the NPR increased from 7 to 9 and again increased when the NPR increased to 11 for lower SPRs. For higher SPRs, the angles kept on increasing while increasing the NPRs. Finally, for secondary inlet located ¾ th of the divergent section length, increasing the NPR lead to the decrease in deflection angle with some exceptions.

Figure 6.20 shows the Schlieren images showing even the internal flow characteristics captured during experimental studies in the nozzle where the secondary inlet was located halfway of the divergent section length, the NPR were varied but the SPR was kept at 0.1.

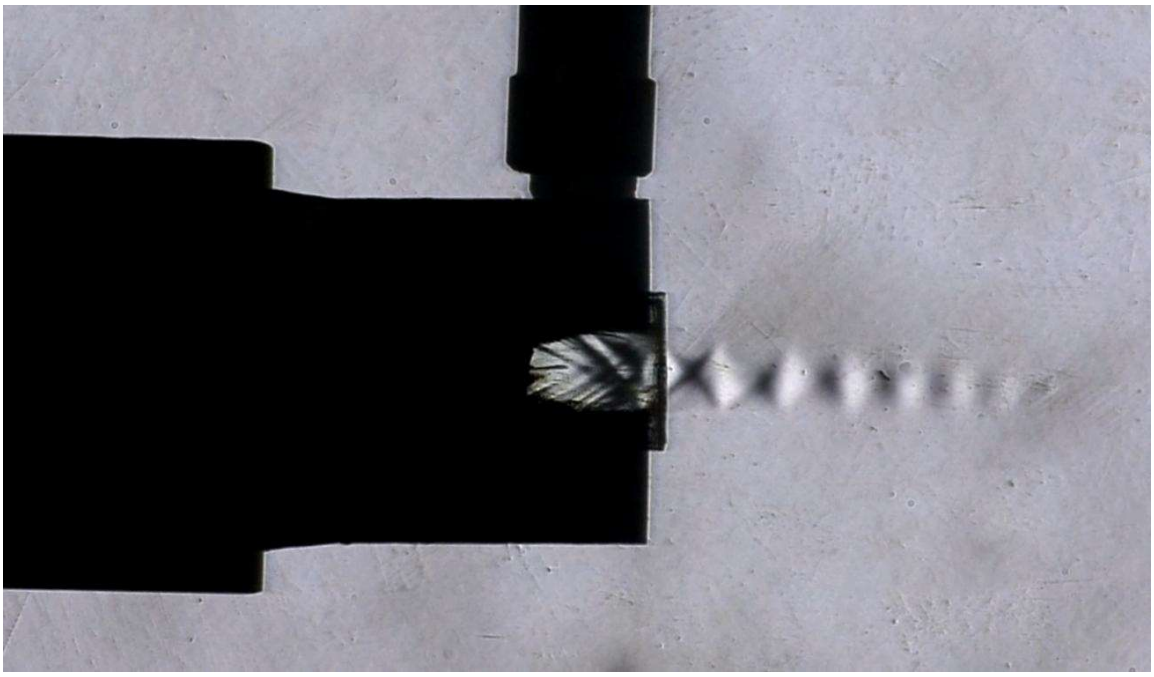

(a)

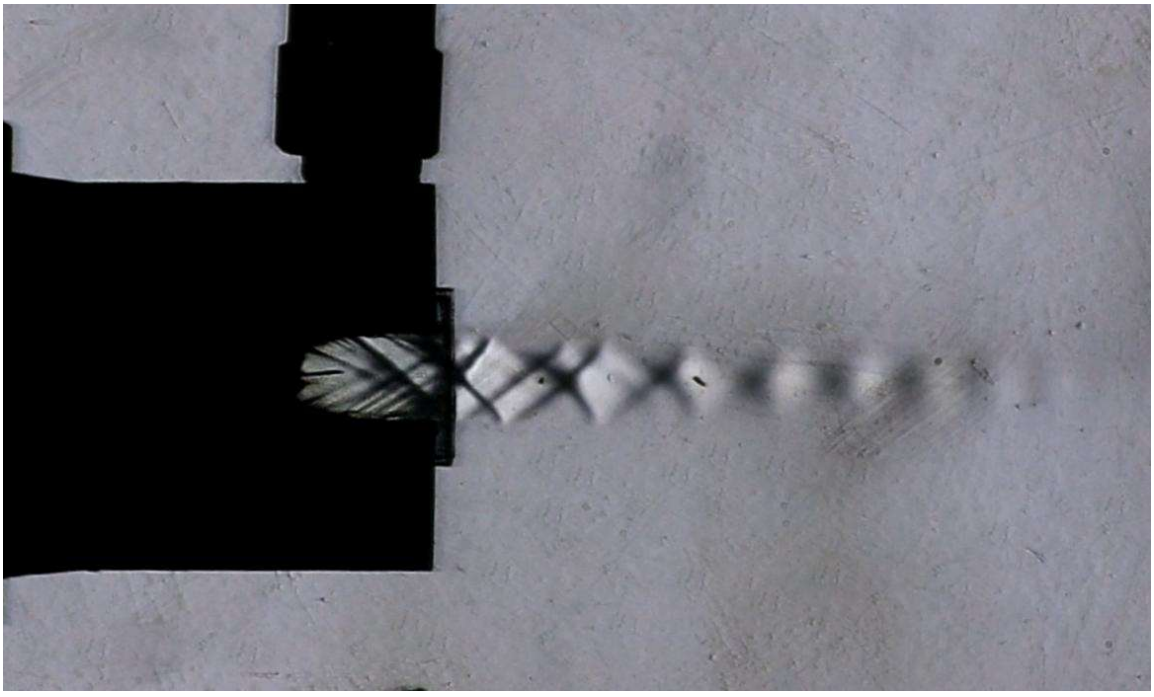

(b)

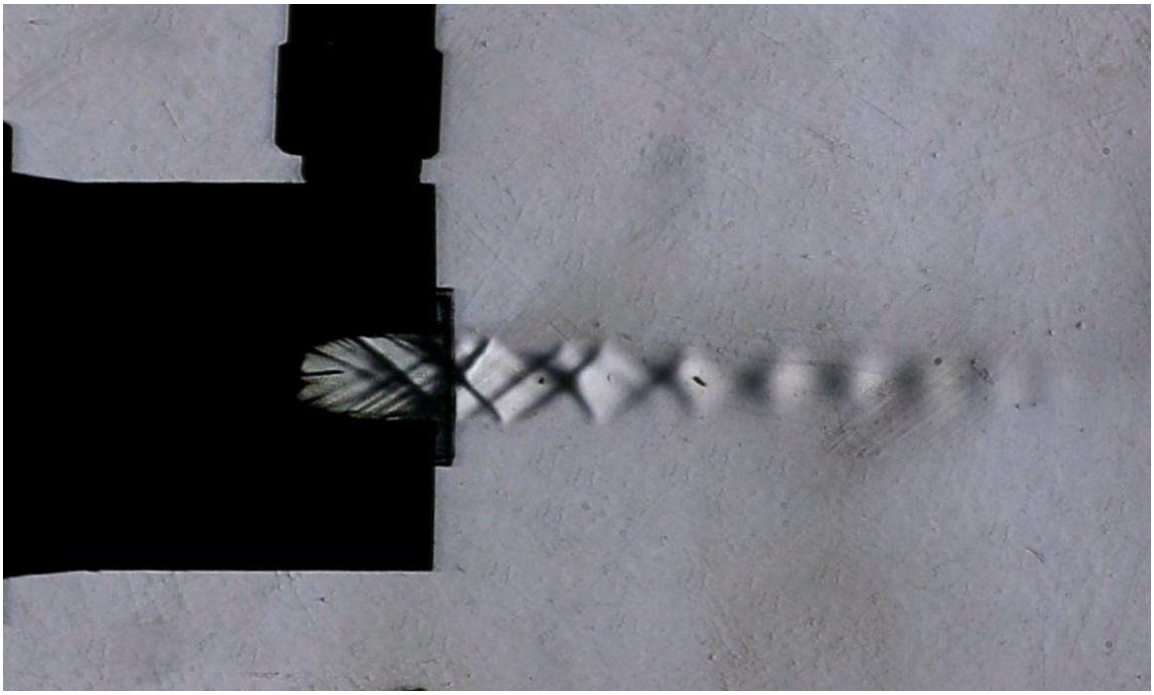

(c)

Figure 6.20: Jet deflections for secondary inlet located half way of divergent section, SPR = 0.1 and (a) NPR = 7, (b) NPR = 9, and (c) NPR = 11

It can be observed from the above figures that for a low SPR of 0.1, the jet deflection decreased with the increase in NPR. The shock waves formed inside the nozzle due to introduction of secondary inlet and other smaller shock waves formed most probably produced due to surface roughness of the wall (as the nozzle was 3 D printed and did not have smooth wall) are clearly seen in the Schlieren images.

#### 6.2.3.2 Effect of SPRs

As mentioned earlier, the SPRs taken for experimental study were 0.1, 0.2, 0.3, 0.4, 0.5, 0.6 and 0.7. Figure 6.21 summarizes the variations in deflection angle at different NPRs and secondary inlet locations.

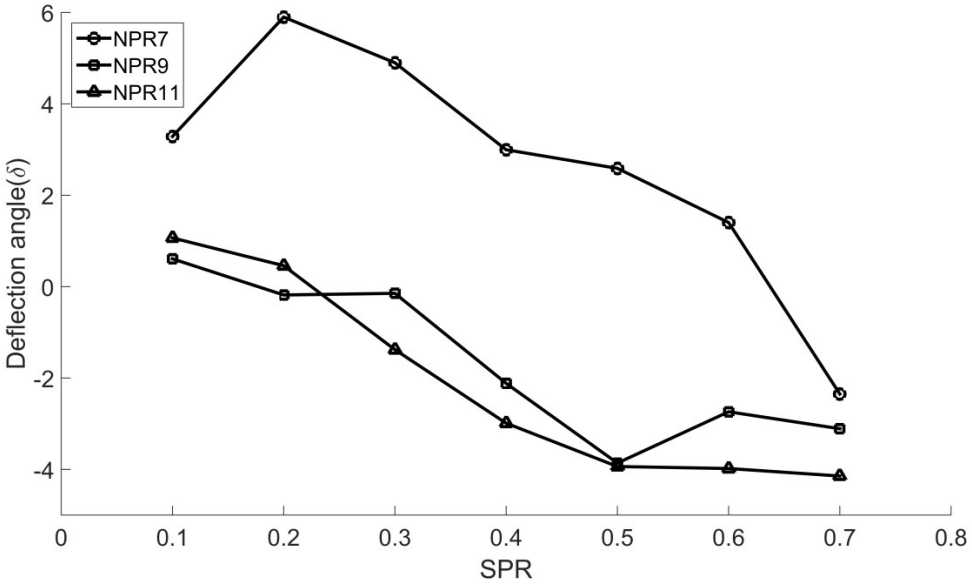
NPR7
NPR9
NPR11
Deflection angle($\delta$)
SPR
6
4
2
0
-2
-4
0
0.1
0.2
0.3
0.4
0.5
0.6
0.7
0.8

(a)

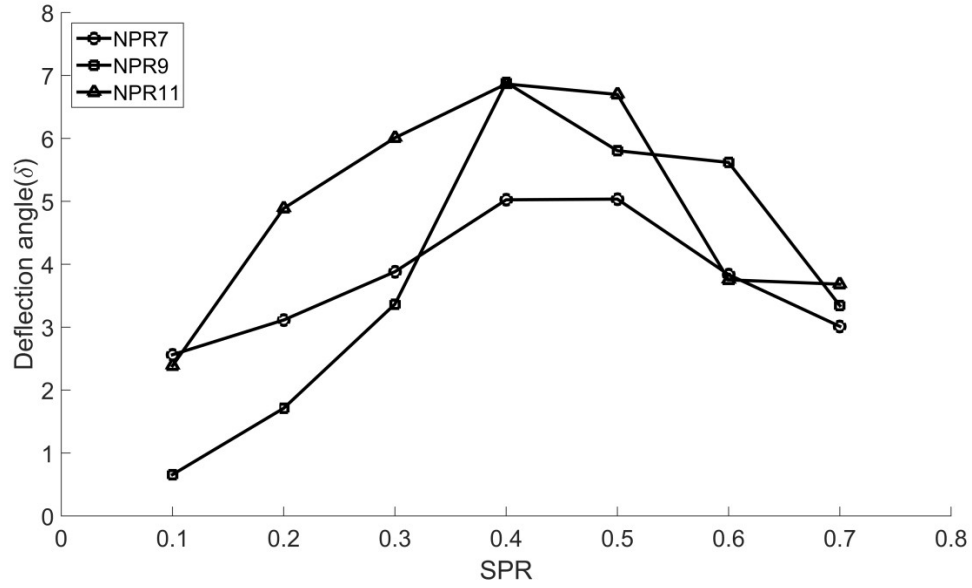
NPR7
NPR9
NPR11
Deflection angle($\delta$)
SPR
8
7
6
5
4
3
2
1
0
0
0.1
0.2
0.3
0.4
0.5
0.6
0.7
0.8

(b)

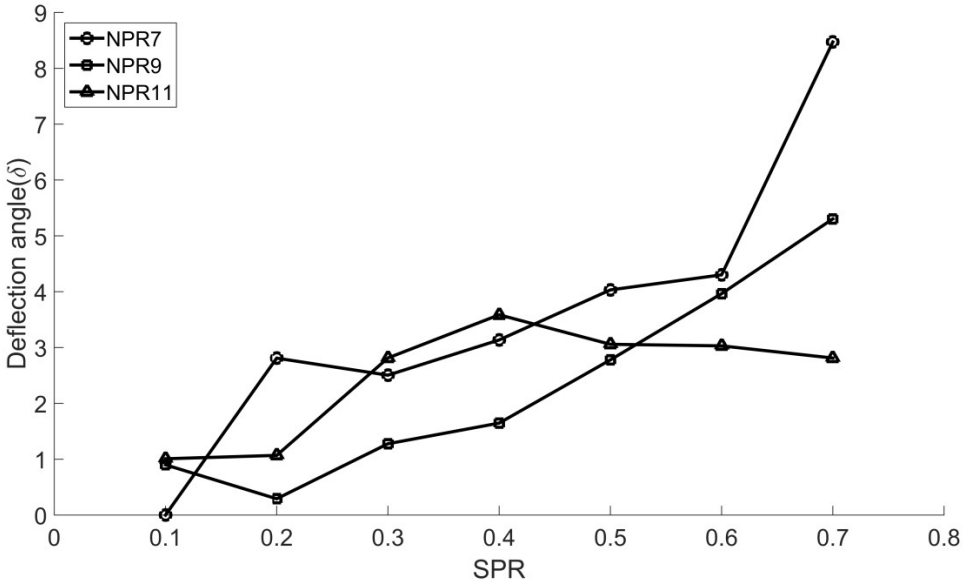


(c)

Figure 6.21: Variation of deflection angle with SPR for the given NPRs when the secondary inlet is located at (a) 25 %, (b) 50 %, and (c) 75 % of the divergent section length

For secondary inlet located at ¼ th of the divergent section length, the deflection angle increased with SPR reaching a maximum value at SPR corresponding to 0.2 for NPR 7. Further increasing the SPR saw decrease in the deflection angle. At this location, for the NPR 7, the deflection angles were positive for all the SPRs except for SPR of 0.7. Similarly, for NPR corresponding to 9 and 11, the jet deflection decreased with increase in SPR and the jet started to deflect in opposite direction beyond the SPR of 0.3. On further increasing the SPR, the jet deflected even more in the opposite direction i.e. the jet deflected increased in the opposite direction. This phenomenon can be seen in the images of Figure 6.22. It was seen that for the nozzle, where the secondary inlet was located at ¼ th of the divergent section length, the oblique shock produced due to introduction of secondary air was reflected by the nozzle wall at the opposite side. The strength of the incident and reflected shock wave however varied with the SPR. For lower SPR, a weak shock wave was produced along with even weaker reflected shock wave. As a result, there was a very small deviation in the jet as shown by Figure 6.22 (a). As the SPR increased, stronger shock waves were formed along with stronger reflected

shock wave. This reflected shock wave deflected the flow of jet in opposite direction compared to that deflected by incident shock wave. As a result the jet deflection occurred towards center line and even in opposite direction as evident in Figure 6.22 (b). When the SPR was further increased to 0.7, the oblique shock got even stronger and the incident shock wave caused boundary layer separation on the opposite wall and another oblique shock was seen to appear ahead of the point of separation. This oblique shock deflected the jet in the direction opposite to that caused by earlier oblique shock wave. This deflection caused the jet to deflect in opposite direction as evident from Figure 6.22 (c).

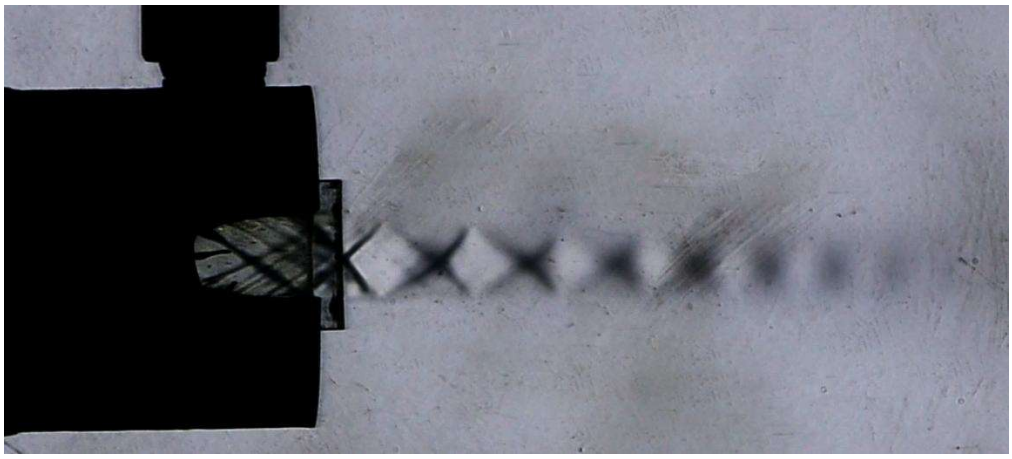

(a)

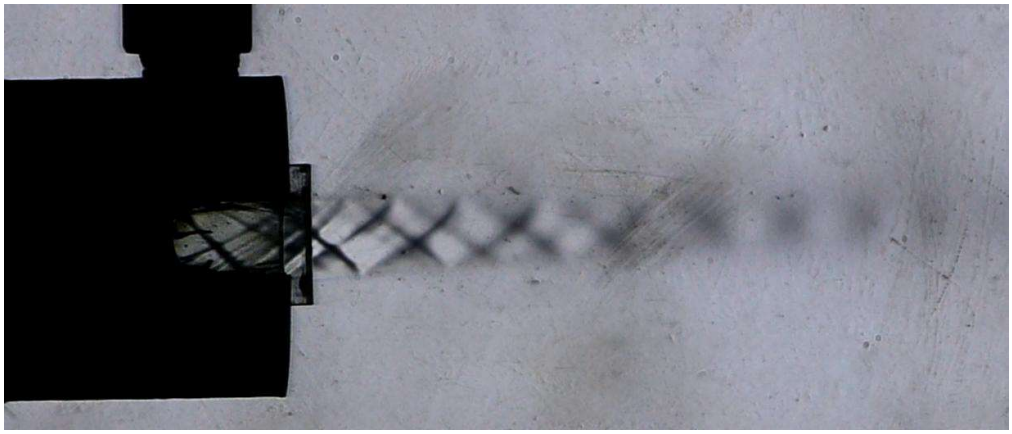

(b)

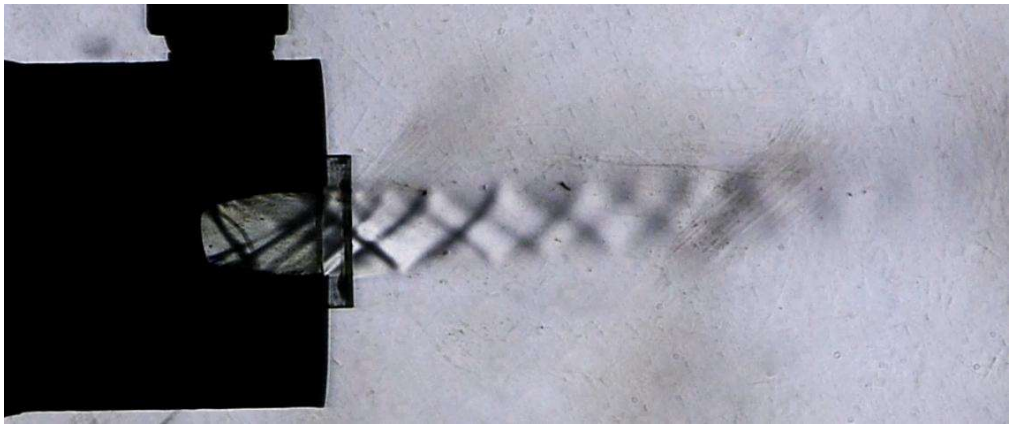

(c)

Figure 6.22: Schlieren images of jet along with internal flow characteristics in nozzle when secondary inlet is located at 25 % of divergent section length, NPR = 11 and (a) SPR = 0.1; (b) SPR = 0.4 and (c) SPR = 0.7

For secondary inlet located half way of the divergent section length, the jet deflection increased with the increase in SPR, reached maximum at SPR corresponding to 0.4 and decreased thereafter for all the NPRs as depicted in Figure 6.21 (b). The Schlieren images obtained for NPR = 11 and different SPRs when the secondary inlet was located at 50 % of the divergent section length are shown in the Figure 6.23. It was observed from the experiments that at lower SPRs (up to 0.4), the oblique shock caused by secondary air was not incident on the opposite wall of the nozzle, and thus the jet was deflected by the incident oblique shock alone. Also, the strength and thus inclination of the oblique shock increased with SPR and thus the jet deflection increased up to SPR of 0.4 as shown by Figure 6.23 (a) and (b). Beyond the SPR of 0.4, the shock angle increase and the shock wave were incident on the nozzle wall opposite to the secondary inlet. This caused a reflection shock wave which acted to deflect the jet in the direction opposite to that caused by incident shock wave and thus, resulting in lower deflection angle as seen in Figure 6.23 (c).

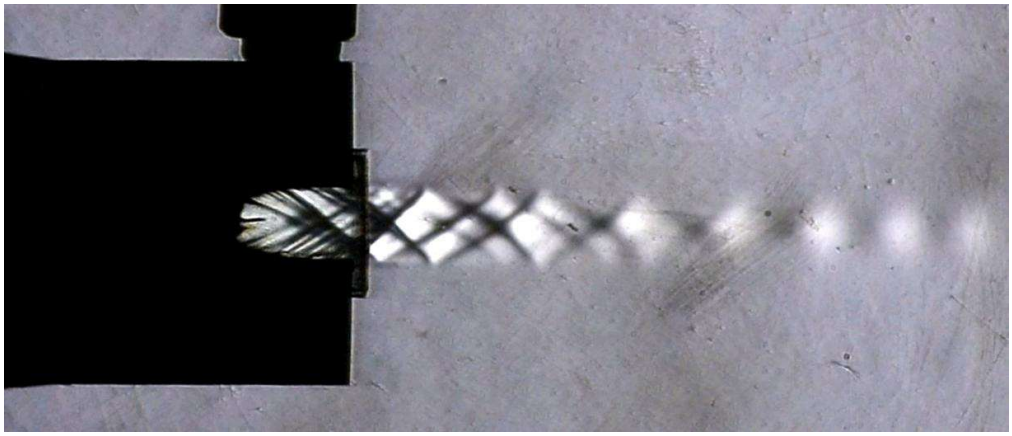

(a)

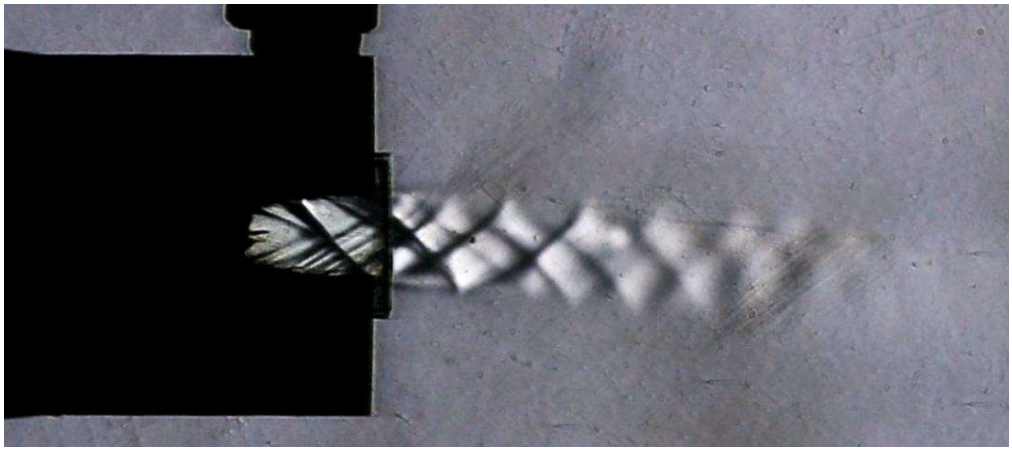

(b)

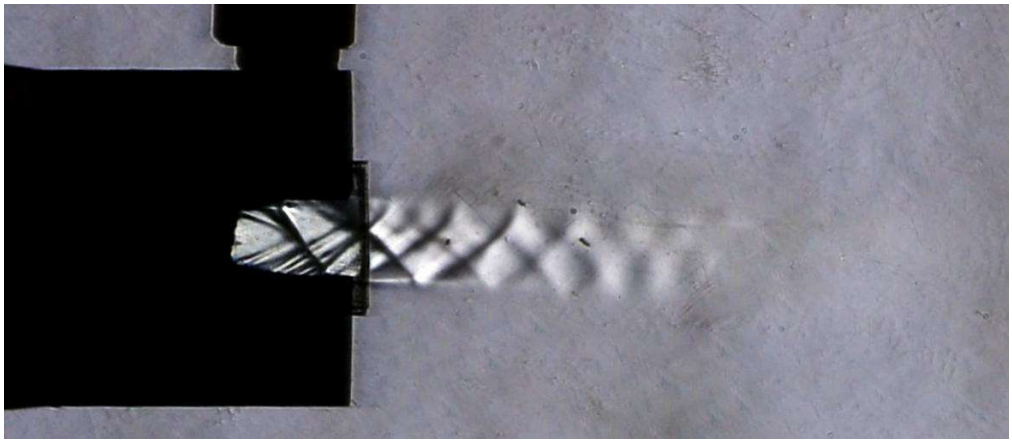

(c)

Figure 6.23: Schlieren images of jet along with internal flow characteristics in nozzle when secondary inlet is located at 50 % of divergent section length, NPR = 11 and (a) SPR = 0.1; (b) SPR = 0.4 and (c) SPR = 0.7

For the secondary inlet located at three quarter of the divergent section length, the deflection angles were seen to invariably increase while increasing the SPRs for the NPRs corresponding to 7 and 9. For NPR corresponding to 11, the jet deflection increased till the SPR of 0.4 and decreased thereafter.

#### 6.2.3.3 Effect of Secondary Inlet Locations

As aforementioned, 3 locations of secondary inlet were taken for the current study. The secondary inlets were located at 25 %, 50 % and 75 % of the divergent section length. In all cases, the secondary inlets had rectangular section and always opened perpendicularly to the primary flow direction. The effect of varying the secondary inlet location on the deflection angle of jet is summarized in the Figure 6.24.

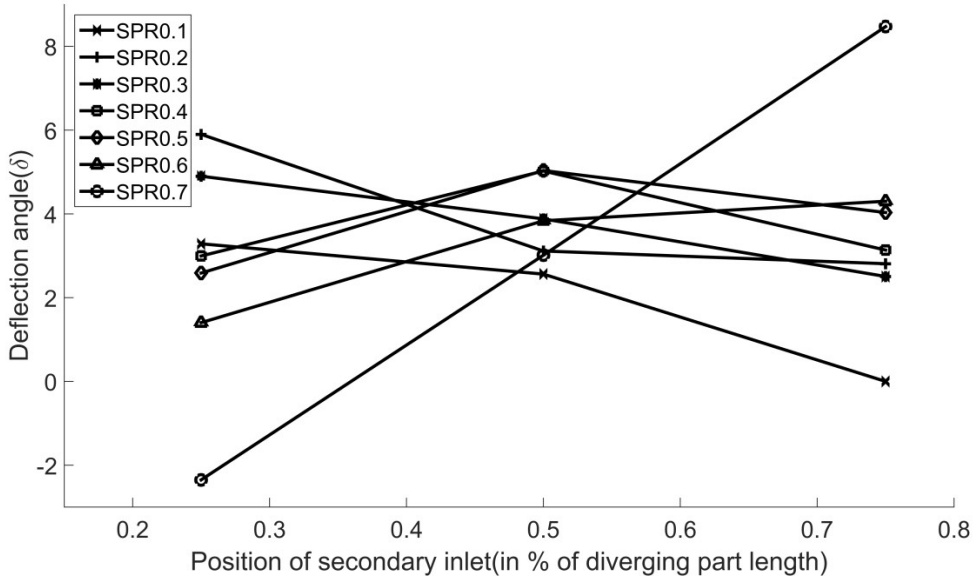


(a)

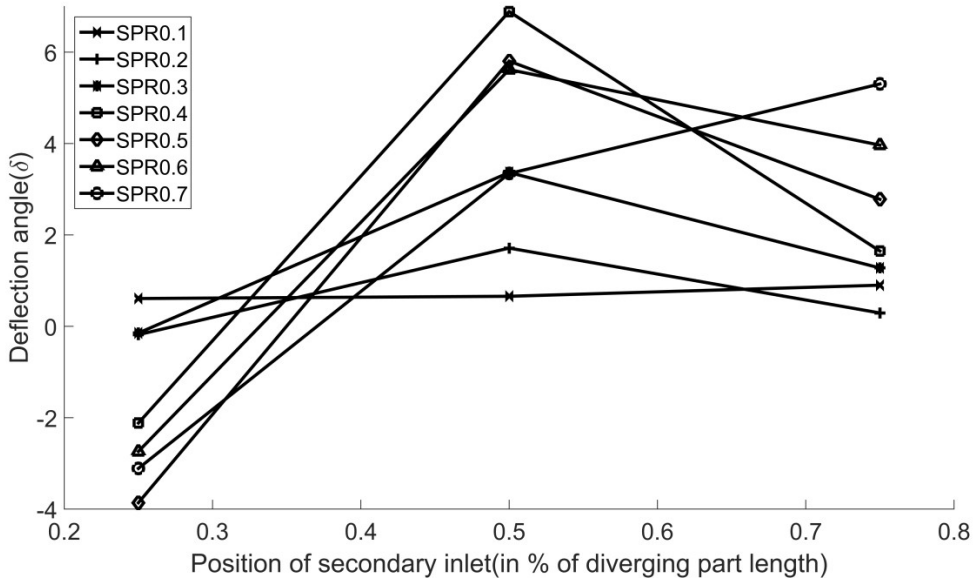


(b)

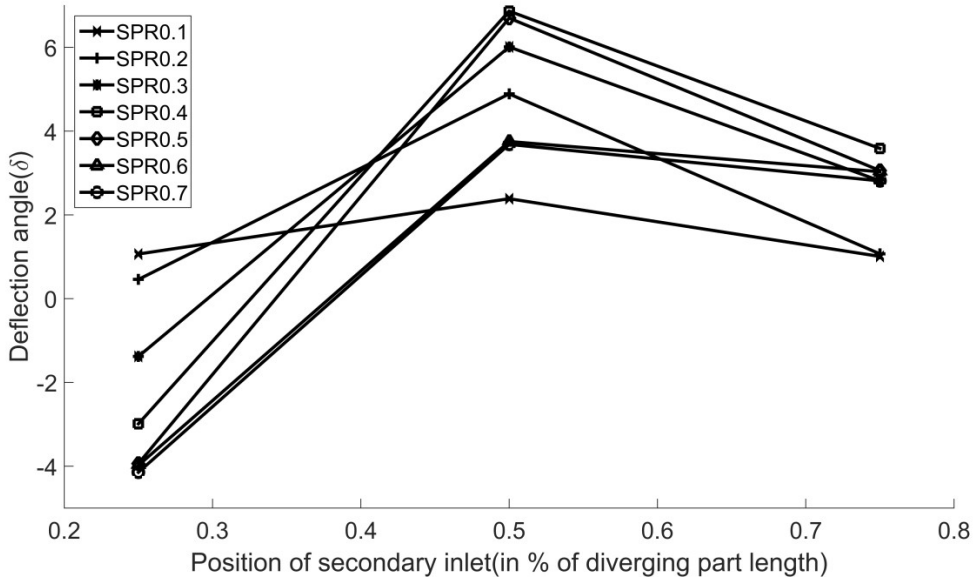


(c)

Figure 6.24: Variation of deflection angle with respect to secondary inlet position for the given SPRs when (a) NPR = 7, (b) NPR = 9, and (c) NPR = 11

The jets from nozzle were seen to increase in deflection with the when the secondary inlet changed from 25 % to 50 % of the divergent section length. For the secondary inlets located at 50 % of the divergent section length, the deflections were the maximum with few exceptions. On further shifting the secondary inlet to 75 % of the divergent section

length, the deflection angles decreased except for NPR corresponding to 7 and 9 and SPR corresponding to 0.7.

Some of the images captured by Schlieren setup showing the variation of deflection angle with secondary inlet locations are as follows:

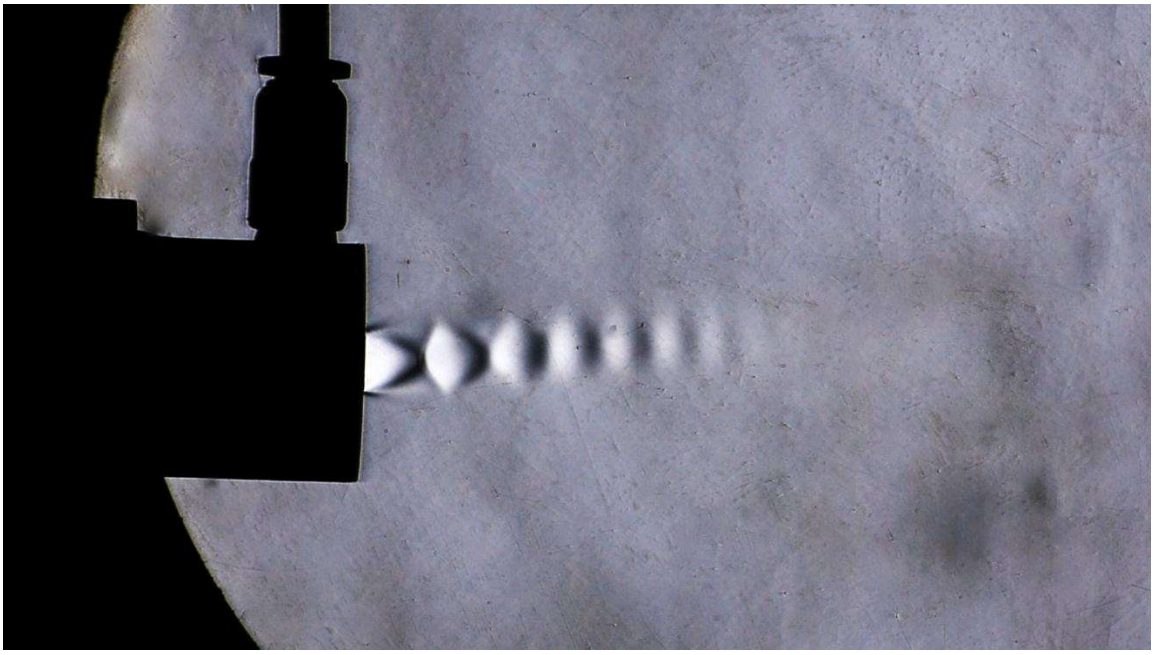

(a)

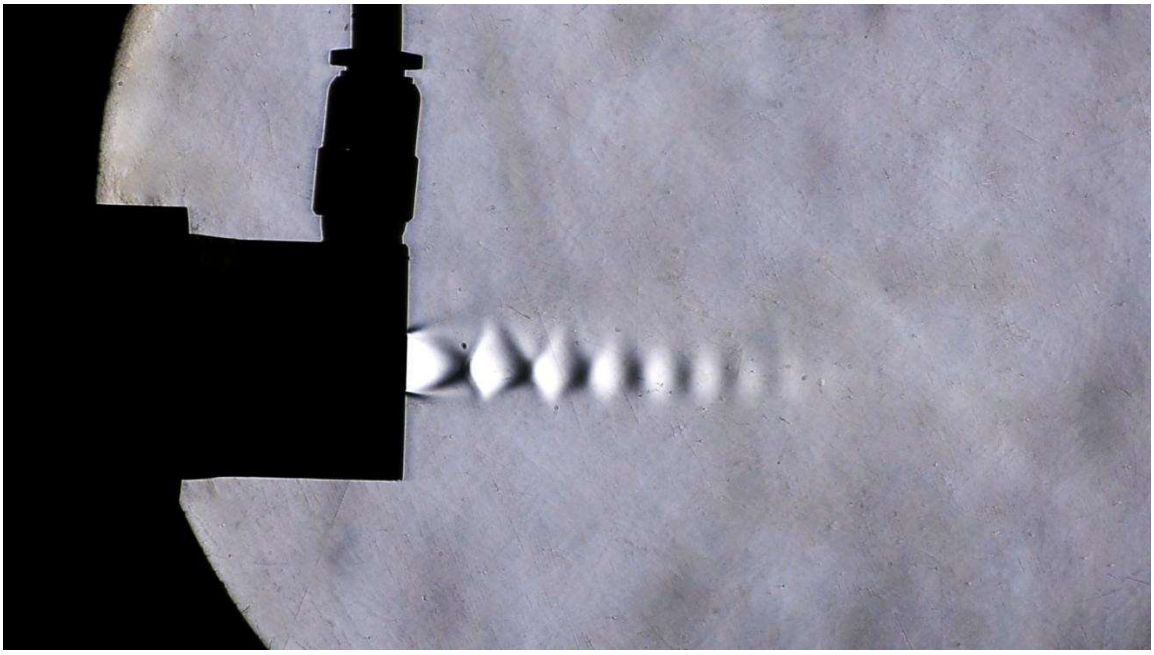

(b)

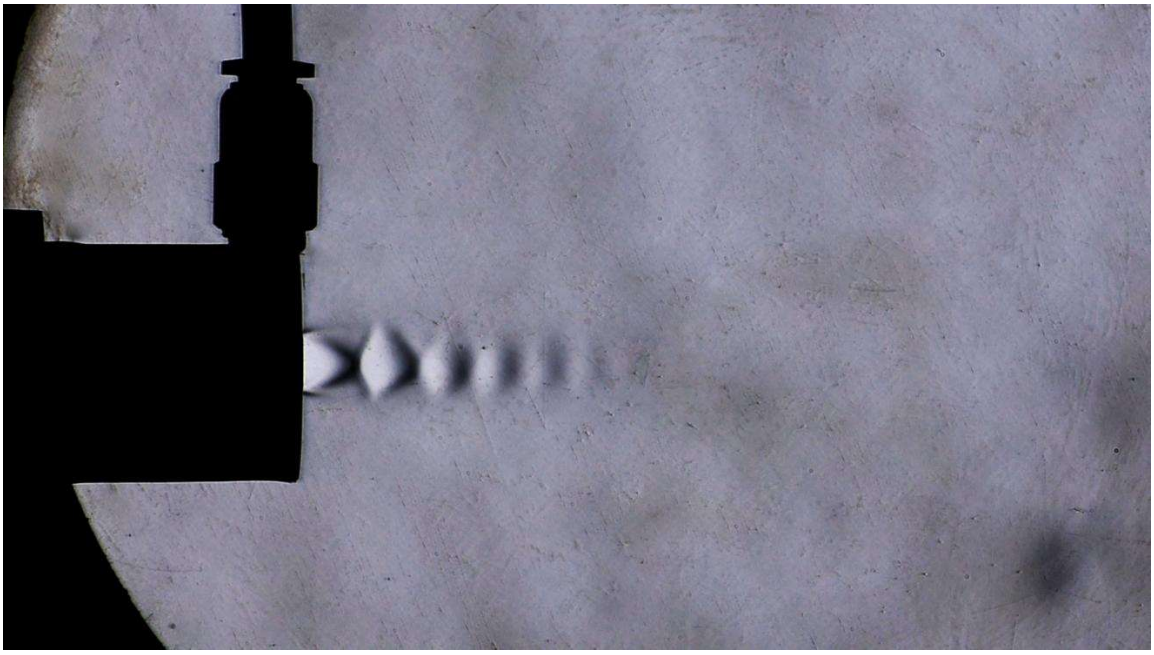

(c)

Figure 6.25: Jet deflection corresponding to NPR = 11, SPR = 0.7 and when the secondary inlet located at (a) 25 %, (b) 50 % and (c) 75 % of the divergent section length

## 6.3 Comparison between Computational and Experimental Results

### 6.3.1 Effect of NPR

In computational analysis, decrease in NPR values (5 and 7) resulted in over-expansion of the jets, and increase in NPR values (9 and 11) resulted in under-expansion of the jets. In the case of nozzles where secondary inlets were located at 25 % and 75 % of the divergent section length, deflection angle decreased when NPR increased at all SPR in computational study. In experimental study too, the over-expanded jets (NPR 7) underwent greater jet deflection than the under-expanded ones when secondary inlets were located at 25 % and 75 % of divergent section length. Increasing NPR reduced the jet deflection, as computationally predicted in these two cases. However, for the cases where secondary inlet was located at 50 % of divergent section length, there were mixed effects of NPR on jet deflection in both computational and experimental results. In this case, computational simulations predicted the decrease in deflection angle with the increase in NPR for SPR ranging from 0.1 to 0.4 whereas, for other SPRs, the deflection angles were predicted to increase with increase in NPR. Experimental results, on the

other hand, showed the decrease in deflection for change in NPR from 7 to 9 and increase in deflection angle thereafter for majority of the SPRs.

### 6.3.2 Effect of SPR

For both studies, seven values of SPR (0.1 - 0.7) were considered. When the secondary inlets were located at 25 % and 50 % of divergent section length, the computational results and experimental results depicted the similar trend. In both instances, the deflection angle increased up to certain SPR value (between 0.2 and 0.5) and decreased thereafter. In case of nozzle with secondary inlet located at 75 %, some differences were seen. In computational study, the deflections were predicted to increase with SPR and reach the maximum value at SPR of 0.4 – 0.5 and decrease beyond this SPR value. The experimental results confirmed this trend only for NPR of 11. For other NPRs (i.e. 7 and 9), the deflection angles kept on increasing with the increase in SPR.

### 6.3.3 Effect of Secondary Inlet Location

Three locations of secondary inlet were examined: 25%, 50%, and 75% of the divergent section length. In computational analysis, the maximum deflection happened when the secondary inlet was kept at 75%, except in a few instances (e.g., SPR = 0.2, NPR = 5). At 25% location, the oblique shock waves reflected from the opposite wall reduced the jet deflection and beyond the SPR of 0.4, the jet deflected in the direction opposite to that anticipated. This was also true for cases when the secondary inlet was kept at 50 % location. Experimental testing however showed opposite jet deflection beyond SPR of 0.3 for NPRs 9 and 11 and beyond SPR of 0.6 for NPR 7. In contrast to computational results, the experimental results didn't show opposite deflection in nozzle where secondary inlet was located at 50 % of the divergent section length. Similarly, the experimental analysis showed the maximum deflection at 50% of the divergent section, except in a few cases where 75% had higher deflection. At 75% location, deflection angles were lesser in most cases, conforming to numerical findings but deviating to a certain degree.

In summary, although the magnitude of jet deflection angle computed numerically and measured experimentally differed, the computational results predicted the trend of jet deflection properly for varying NPRs and SPRs. The variation in the deflection angle can

be attributed to the wall roughness of the 3 D printed nozzles. The roughness on the wall of the nozzle produced numerous weak shock waves which slowed and affected the dynamics of jet flow in the nozzle. The weak shock waves produced due to the nozzle wall roughness were clearly visible in the Schlieren image captured. Furthermore, variations of jet deflection with secondary inlet location obtained computationally and experimentally were in agreement for secondary inlets located at ¼ th and ½ of the divergent section length. However, the variations were not in proper agreement when the secondary inlet was located at ¾ th of the divergent section length.

# CHAPTER SEVEN : CONCLUSIONS AND RECOMMENDATIONS

## 7.1 Conclusions

This work focused on experimental and numerical analysis of fluidic thrust vectoring in a two-dimensional convergent-divergent (CD) nozzle using shock vector control. Computational fluid dynamics (CFD) analysis and experimental investigation with a Schlieren imaging system were coupled to investigate the effect of secondary injection on thrust vectoring. A single-mirror Schlieren system was fabricated and tested for its sensitivity in order to use it for the experimental study. The CD nozzle was designed using the Method of Characteristics (MOC) and simulated in ANSYS Fluent to evaluate flow patterns and jet behavior. Secondary air inlets were incorporated into the earlier designed CD nozzle. The study further explored the influence of key parameters on thrust vectoring, including: NPR, SPR and secondary inlet location using both computational and experimental analysis. Numerical simulations provided the insight regarding how secondary pressure ratio (SPR), nozzle pressure ratio (NPR) and secondary inlet locations influence jet deflection, and experimental observations validated these results with the aid of Schlieren imaging techniques.

The major findings of the research can be summed up in following points:

- For lower NPR values (5 and 7), the jets were over – expanded and they had larger deflections, while higher NPR values (9 and 11) resulted in under-expanded jets and they had smaller deflection when the secondary air was introduced.
- For secondary inlet locations at ¼ th and mid – way of the divergent section length, increasing SPR initially increased jet deflection, but beyond some limit (SPR = 0.4 – 0.5), deflection began to decrease due to complex shock interactions. This was true also true for NPR corresponding to 11 and secondary inlets located at ¾ th of the divergent section length. However, for other NPRs (7 and 9), experiments showed increase in deflection angle with the increase in SPR in contrast to computational observations, wherein, the deflections increased up to SPR of 0.4 and decreased thereafter.
- In experimental analysis, the largest deflections of the jet were found to occur when the secondary inlet was at 50% of the divergent section as opposed to when located at

75 % of the length as predicted by computational analysis. Deflections in the opposite direction than expected occurred in experiments as well in case of secondary inlet located at 25 % of divergent section length above the SPR of around 0.3 as stipulated by simulations.

- Numerical calculations performed in ANSYS Fluent were highly consistent with experimental results, validating the methodology. There were minor discrepancies owing to boundary layer characteristics, manufacturing tolerances of the nozzle, and accuracy of measurement in the experiment.

### 7.2 Recommendations

Based on the findings, the following recommendations are proposed for further research and practical applications:

- Constructing and using z – type Schlieren setup with higher sensitivity and using high end high speed cameras to capture the fluid flow along with higher-precision measurement techniques to reduce uncertainties in deflection angle measurements.
- Addressing fabrication imperfections in 3D-printed nozzles to minimize surface roughness effects.
- Expanding the study to include a wider range of NPRs and SPRs, particularly at extreme values, to observe the full spectrum of flow behaviors.
- Exploring the effect of other parameters such as injection angle and secondary flow shape on thrust vectoring performance.
- Conducting 3D simulations to capture more realistic flow behavior.
- Investigating other turbulence models.

# REFERENCES


Afridi, S., Khan, T. A., Ali Shah, S. I., Shams, T. A., Mohiuddin, K., & Kukulka, D. J. (2023). Techniques of Fluidic Thrust Vectoring in Jet Engine Nozzles: A Review. *Energies*.

Anderson, J. D. (2021). *Modern Compressible Flow with Historic Perspective.* New York: McGraw-Hill Education.

Çengel, Y. A., & Cimbala, J. M. (2006). *Fluid Mechanics Fundamentals and Applications.* New York: Mc Graw Hill.

Gena, A., & Voelker, C. (2018). *Schlieren Imaging and Analysis.*

Maharjan, S. (2023). *Design and Setup of Z-Type Schlieren Imaging System for Flow Visualization.* Lalitpur: Pulchowk Campus, Institute of Engineering.

Mazumdar, A. (2013). Principles and Techniques of Schlieren Imaging. *Columbia University*.

Merzkirch, W. (2011, February 11). *Thermopedia*. Retrieved from https://www.thermopedia.com/content/1245/

Prisăcariu, E., Vilag, V., Nicoară, R., Suciu, C., Dobromirescu, C., & Dombrovschi, M. (2020). Calculating and Setting up a Schlieren System. *Turbo*, 25-34.

Ranabhat, S., Darlami, K., Bhattarai, S., & Shrestha, N. (2022). Numerical and Experimental Investigation of Exhaust Flow from Convergent - Divergent Nozzle. *Proceedings of 12th IOE Graduate Conference*, (pp. 212 - 220). Kathmandu.

Robinson, C. (2016). Flow Through a de Laval Nozzle. *Boston University*.

Saito, T., & Fujimoto, T. (2009). Numerical studies of shock vector control for deflecting nozzle exhaust flows. *Shock Waves* (pp. 985 - 990). Springer: Berlin.

Settles, G. S. (2001). *Schlieren and Shadowgraph Techniques: Vvisualizing Phenomena in Transparent Media.* Berlin: Springers.

Shakouchi, T., & Fukushima, S. (2022). Fluidic Thrust, Propulsion, Vector Control of Supersonic Jets by Flow Entrainment and Coanda Effect. *Energies*.

Singh, J., Zerpa, L. E., Partington, B., & Gamboa, J. (2019). Effect of nozzle geometry on critical-subcritical flow transitions. *Heliyon*.

Sopeña i Martínez, P. (2014). Set up of a Schlieren Flow Visualization Device. *Treballs Finals de Grau (TFG) - Física*.

Waithe, K. A., & Deere, K. A. (2003). Experimental and Computational Investigation of Multiple Injection Ports in a Convergent-Divergent Nozzle for Fluidic Thrust Vectoring. *21st AIAA Applied Aerodynamics Conference.* Orlando, Florida.

Wu, K., & Dong Kim, H. (2019). Numerical study on the shock vector control in a rectangular supersonic nozzle. *Proceedings of the Institution of Mechanical Engineers* (pp. 4943-4965). Journal of Aerospace Engineering.

# APPENDICES

## Appendix A: Deflection Angles Obtained From Computational and Experimental Analysis

Table A1: Deflection angles obtained from computational analysis at different secondary inlet locations and different NPRs and SPRs

| Location | At 25 % of divergent section | | | |
|---|---|---|---|---|
| SPRs | NPR5 | NPR7 | NPR9 | NPR11 |
| 0.1 | 1.079 | 0.203 | 0.345 | 0.432 |
| 0.2 | 4.234 | 1.061 | 0.303 | 0.796 |
| 0.3 | 1.377 | 1.321 | 0.729 | 0.606 |
| 0.4 | -0.002 | 0.0406 | 0.433 | 0.738 |
| 0.5 | -1.459 | -0.92 | -0.304 | 0.114 |
| 0.6 | -6.802 | -4.122 | -2.189 | -2.235 |
| 0.7 | -8.151 | -7.977 | -8.079 | -8.027 |
| Location | At 50 % of divergent section | | | |
| SPRs | NPR5 | NPR7 | NPR9 | NPR11 |
| 0.1 | 0.436 | 0.148 | 0.047 | 0 |
| 0.2 | 1.403 | 0.812 | 0.483 | 0.659 |
| 0.3 | 2.864 | 1.55 | 1.012 | 1.55 |
| 0.4 | 3.76 | 1.966 | 2.547 | 1.638 |
| 0.5 | 1.546 | -3.077 | -2.245 | 2.825 |
| 0.6 | -1.331 | -5.499 | -5.446 | -2.859 |
| 0.7 | -6.179 | -6.147 | -7.147 | -6.527 |
| Location | At 75 % of divergent section | | | |
| SPRs | NPR5 | NPR7 | NPR9 | NPR11 |
| 0.1 | 1.733 | 0.654 | 0.491 | 0.131 |
| 0.2 | 4.255 | 1.713 | 1.065 | 1.065 |
| 0.3 | 9.436 | 4.737 | 2.944 | 2.13 |
| 0.4 | 10.328 | 9.17 | 7.153 | 5.881 |

| | | | | |
|---|---|---|---|---|
| 0.5 | 5.949 | 5.639 | 5.533 | 7.029 |
| 0.6 | 3.847 | 1.606 | 1.33 | 1.061 |
| 0.7 | 2.042 | 1.077 | 0.849 | 0.572 |

Table A2 : Deflection angles obtained from experimental analysis at different secondary inlet locations and different NPRs and SPRs

| NPR | SPR | 0.25 | 0.5 | 0.75 |
|---|---|---|---|---|
| 11 | 0.1 | 1.066 | 2.386 | 1.008 |
| | 0.2 | 0.458 | 4.888 | 1.069 |
| | 0.3 | -1.38 | 6.009 | 2.813 |
| | 0.4 | -2.989 | 6.865 | 3.586 |
| | 0.5 | -3.937 | 6.698 | 3.058 |
| | 0.6 | -3.981 | 3.752 | 3.03 |
| | 0.7 | -4.145 | 3.683 | 2.812 |
| | | | | |
| 9 | 0.1 | 0.608 | 0.657 | 0.9 |
| | 0.2 | -0.183 | 1.712 | 0.292 |
| | 0.3 | -0.147 | 3.366 | 1.277 |
| | 0.4 | -2.117 | 6.888 | 1.647 |
| | 0.5 | -3.862 | 5.804 | 2.779 |
| | 0.6 | -2.739 | 5.618 | 3.965 |
| | 0.7 | -3.11 | 3.343 | 5.304 |
| | | | | |
| 7 | 0.1 | 3.286 | 2.562 | 0 |
| | 0.2 | 5.899 | 3.114 | 2.81 |
| | 0.3 | 4.899 | 3.881 | 2.505 |
| | 0.4 | 2.995 | 5.024 | 3.136 |
| | 0.5 | 2.588 | 5.035 | 4.032 |
| | 0.6 | 1.403 | 3.835 | 4.302 |
| | 0.7 | -2.35 | 3.013 | 8.471 |

## Appendix B: Some Schlieren Images Captured During Experiment

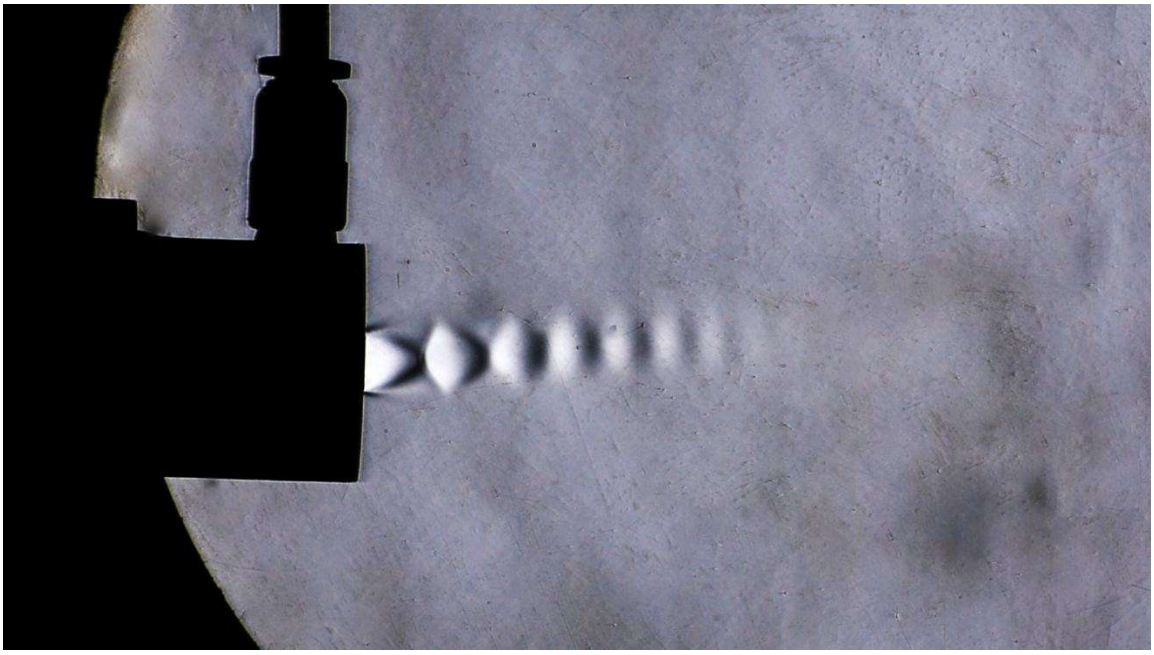

(a)

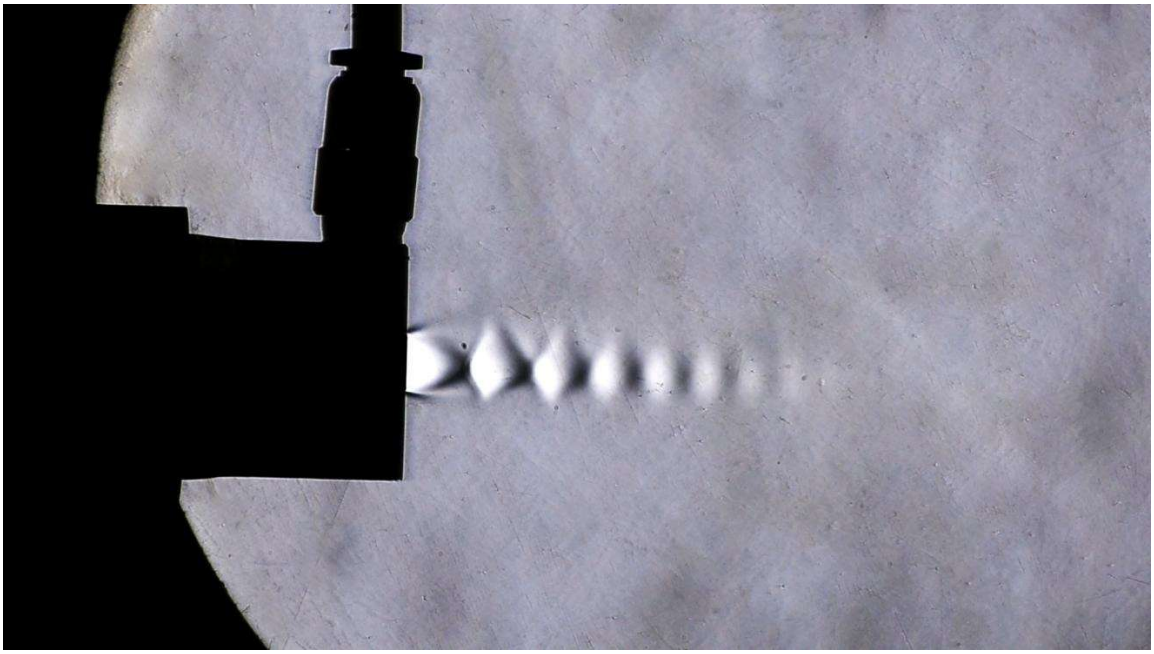

(b)

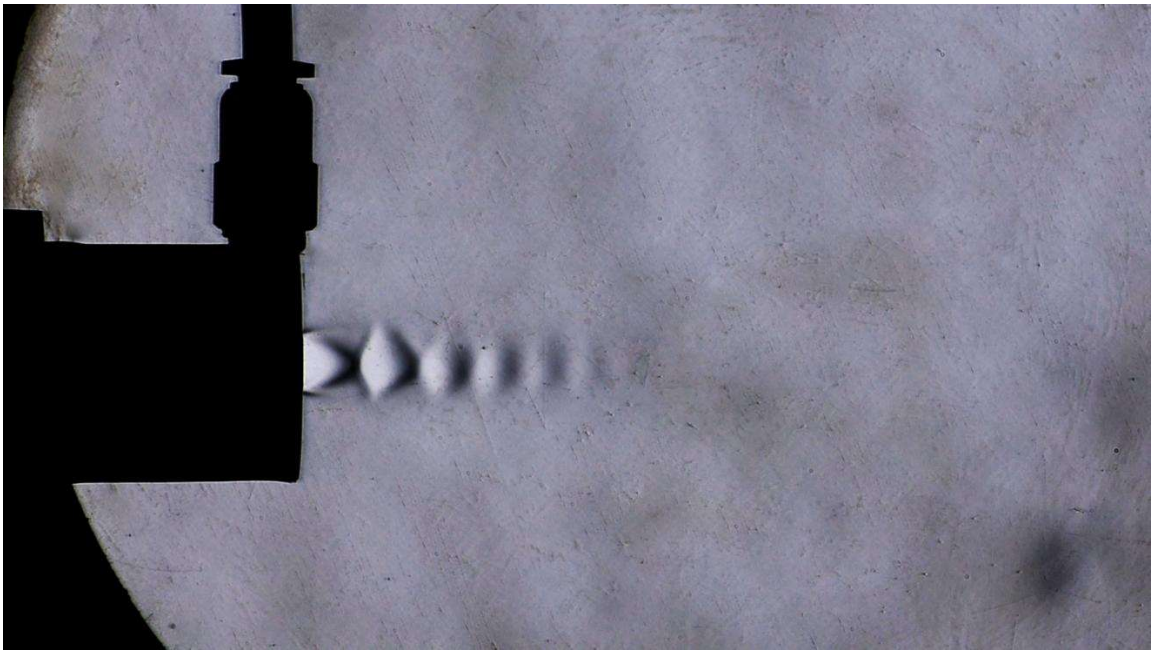

(c)

Figure B1: Schlieren images for jet deflection corresponding to NPR = 11, SPR = 0.7 and when the secondary inlet located at (a) 25 %, (b) 50 % and (c) 75 % of the divergent section length

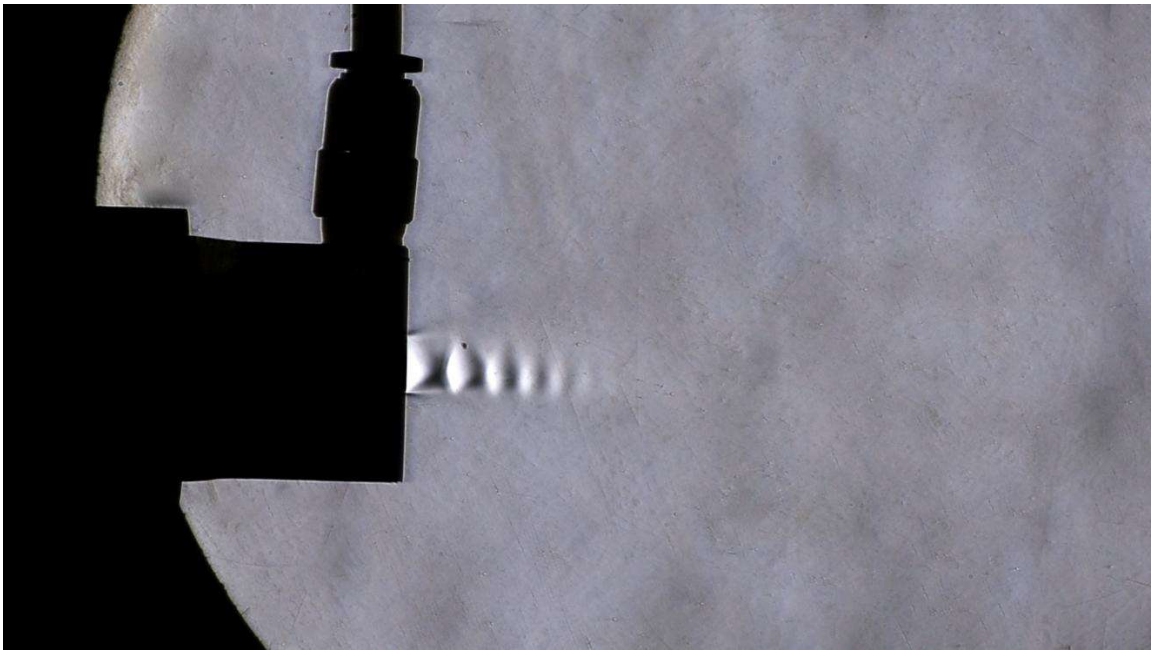

(a)

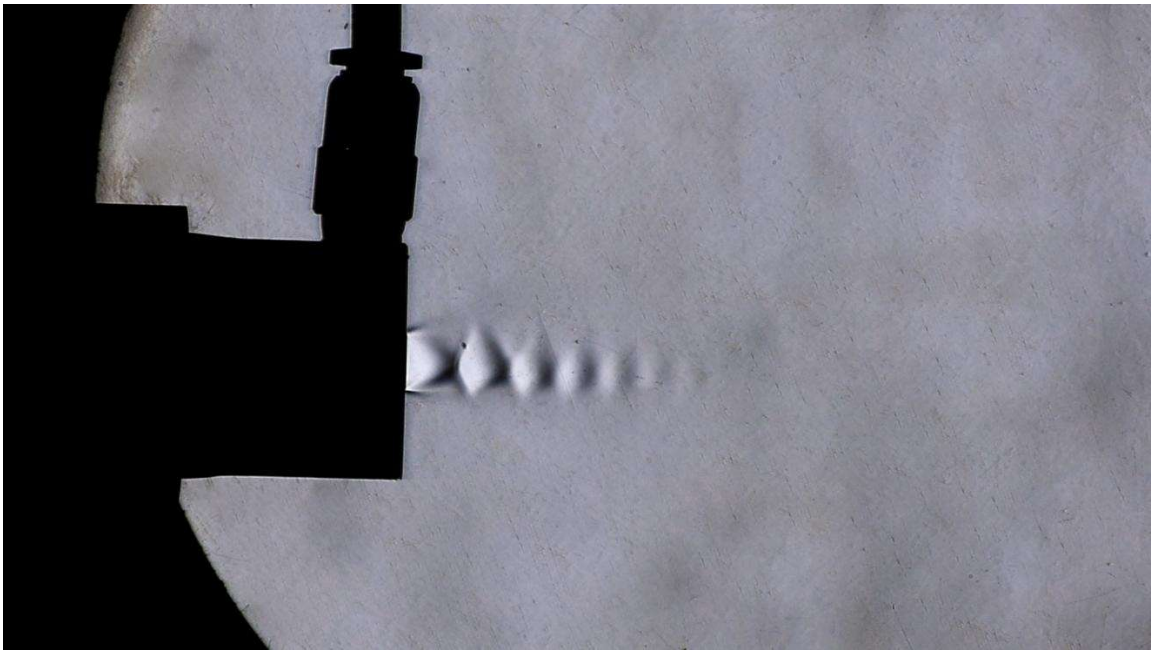

(b)

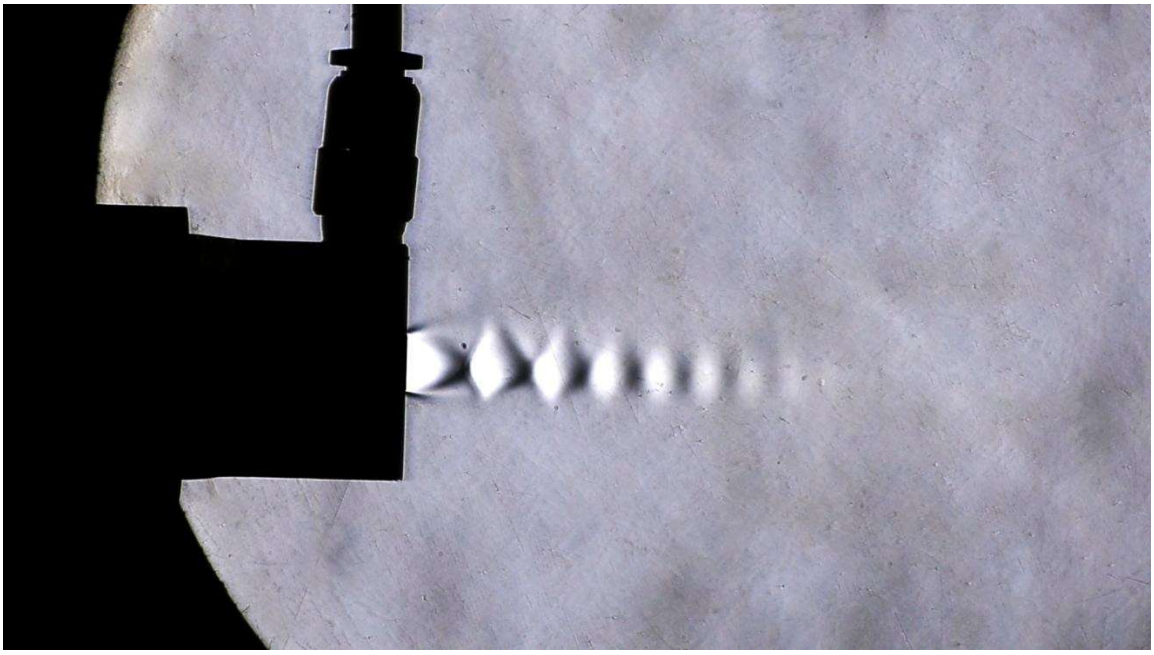

(c)

Figure B2: Jet deflections for secondary inlet located half way of divergent section, SPR = 0.7 and (a) NPR = 7, (b) NPR = 9, and (c) NPR = 11

# Appendix C: Letter of Paper Acceptance at IOEGC



Pulchowk Campus
Institute of Engineering
Tribhuvan University

KESHAV ACHARYA <079msmde011.keshav@pcampus.edu.np>

## [IOEGC16] Editor Decision

1 message

**Kobid** <conference-noreply@ioe.edu.np> Fri, Mar 28, 2025 at 8:10 AM
To: Keshav Kumar Acharya <079msmde011.keshav@pcampus.edu.np>, Kamal Darlami <darlami.kd@pcampus.edu.np>

Keshav Kumar Acharya, Kamal Darlami:

We are pleased to inform you that your manuscript titled "Numerical Simulation of Shock Vector Control in Two Dimensional Convergent Divergent Nozzle" submitted to 16th IOE Graduate Conference is **Accepted** for presentation in the Conference as well as inclusion in the Peer-Reviewed Proceedings.
Please note that inclusion in hard copy proceedings is contingent upon your timely response to further edits, if any, during the publication process.

With Warm Regards,
IOEGC-16 Editorial Team

# Appendix D: Similarity Report



## Keshav Acharya

### Report for plag check.pdf

Tribhuvan University

---

**Document Details**

Submission ID
trn:oid:::3117:448580358

Submission Date
Apr 13, 2025, 11:19 AM GMT+5:45

Download Date
Apr 13, 2025, 12:02 PM GMT+5:45

File Name
Report for plag check.pdf

File Size
6.0 MB

86 Pages

13,656 Words

68,892 Characters

iThenticate Page 1 of 90 - Cover Page Submission ID trn:oid:::3117:448580358



2082/01/03

# 12% Overall Similarity

The combined total of all matches, including overlapping sources, for each database.

## Filtered from the Report

- Bibliography
- Quoted Text
- Cited Text
- Small Matches (less than 8 words)

## Match Groups

- 51 Not Cited or Quoted 12%
  Matches with neither in-text citation nor quotation marks
- 0 Missing Quotations 0%
  Matches that are still very similar to source material
- 0 Missing Citation 0%
  Matches that have quotation marks, but no in-text citation
- 0 Cited and Quoted 0%
  Matches with in-text citation present, but no quotation marks

## Top Sources

8% Internet sources
8% Publications
0% Submitted works (Student Papers)

## Integrity Flags

0 Integrity Flags for Review

No suspicious text manipulations found.

Our system's algorithms look deeply at a document for any inconsistencies that would set it apart from a normal submission. If we notice something strange, we flag it for you to review.

A Flag is not necessarily an indicator of a problem. However, we'd recommend you focus your attention there for further review.

✓ iThenticate Page 2 of 90 - Integrity Overview

Submission ID trn:oid:::3117:448580358



2082/01/03

## Match Groups

- 51 Not Cited or Quoted 12%
  Matches with neither in-text citation nor quotation marks
- 0 Missing Quotations 0%
  Matches that are still very similar to source material
- 0 Missing Citation 0%
  Matches that have quotation marks, but no in-text citation
- 0 Cited and Quoted 0%
  Matches with in-text citation present, but no quotation marks

## Top Sources

- 8% Internet sources
- 8% Publications
- 0% Submitted works (Student Papers)

## Top Sources

The sources with the highest number of matches within the submission. Overlapping sources will not be displayed.

| | | |
|---|---|---|
| 1 | Internet | |
| issuu.com | | 3% |
| 2 | Publication | |
| Saadia Afridi, Tariq Amin Khan, Syed Irtiza Ali Shah, Taimur Ali Shams, Khawar Mo... | | 3% |
| 3 | Internet | |
| elibrary.tucl.edu.np | | 1% |
| 4 | Internet | |
| mice.cs.columbia.edu | | 1% |
| 5 | Internet | |
| www.science.gov | | <1% |
| 6 | Publication | |
| Hoffman, Trent Lee. "Nozzle Design for Vacuum Aerosol Deposition of Nanostruct... | | <1% |
| 7 | Publication | |
| Raj P. Chhabra. "CRC Handbook of Thermal Engineering Second Edition", CRC Pre... | | <1% |
| 8 | Publication | |
| Jun-Lin Chen, Ying-Hao Liao. "Parametric Study on Thrust Vectoring with a Secon... | | <1% |
| 9 | Internet | |
| repository.nwu.ac.za | | <1% |
| 10 | Publication | |
| Karen Deere. "Summary of Fluidic Thrust Vectoring Research at NASA Langley Re... | | <1% |



2082/01/03